School of Chemistry

Investigating High Pressure Microplasmas in Diamond Substrates

Chris Turner

March 2013

Abstract

High pressure microplasmas produce large amounts of radiation and have high electron densities making them useful as radiation sources and plasmachemical reactors. However, they are often susceptible to sputtering and tend to exhibit high gas temperatures which can lead to damage and instabilities. Consequently, most microplasma devices, commonly fabricated out of silicon or metal, are unable to operate above atmospheric pressure. Using a more suitable material should enable operation at higher pressures and ensure longer device lifetimes.

Diamond has many superlative properties which make it a promising material for high pressure microplasmas. These include unparalleled thermal conductivity, a high melting point and the ability to be doped to alter conductivity. The objective of this project was to fabricate a diamond microplasma device, operate it at pressures above one atmosphere and characterise it at these high pressures.

Several micro hollow cathode discharge (MHCD) type devices were fabricated using a combination of boron-doped and un-doped diamond with an electrode separation of 50 μm. The devices operated consistently in helium between 0.5 and 9.5 atm, higher than any previous device in the literature.

V-I characteristics over the pressure range were consistent, showing three modes observed at lower pressures in similar devices: the predischarge, self-pulsing and normal modes. The observation of recognisable modes indicates the devices were operating in a similar manner to lower pressure microplasmas.

Optical emission spectroscopy measurements of the second positive system of nitrogen were used to determine gas temperatures for a device operating between 0.5 and 4.0 atm. The temperature remained constant at around 400 K, the low temperature a reflection of the excellent thermal conductivity of diamond and the non-thermal property of the microplasmas.

Paschen curves recorded for several of the devices were very similar in shape to a theoretical curve following Paschen's law, suggesting the devices operate by the traditional Townsend breakdown mechanism.

The size of aperture was found to have a subtle effect on stability, with smaller apertures showing more stable operation at higher pressures. This might indicate a new scaling law similar to the White-Allis similarity law which acts at high pressures.

Finally, to prove the feasibility of arrays, a 2×2 array of microplasmas was fabricated. When operated under high-frequency pulsed DC the device showed good power distribution between 0.5 and 3 atm.

Following these results it is evident that the project was successful. High pressure microplasmas were produced and characterised, showing that fabrication using diamond is a viable strategy for accessing high pressure operation. Further characterisation, such as determining electron densities and radiative emission, in addition to the production of larger arrays, are clear aims for further investigation.

Contents

1 Introduction

Compared to lower pressure conventional plasmas, microplasmas produce large amounts of radiation and have high electron densities. These properties, in addition to their small size, give them useful applications, for example as UV radiation sources for water purification or ozone generating plasmachemical reactors.[1]

The higher the pressure of the microplasma, the more pronounced these properties become. As such, producing higher pressure microplasmas could lead to more efficient products or new applications. However, in addition to these useful properties, gas temperature and instabilities also increase with pressure, causing difficulties.[2]

The devices in which microplasmas are operated, usually consisting of electrodes separated by a dielectric, are often exposed to these high temperatures. As a result they heat up, leading to damage by localised melting and increased thermionic emission which produces instabilities.[3]

Most conventional devices tend to be made out of metal or silicon. Using a material with more beneficial properties should enable operation at higher pressures. Due to its superlative properties, diamond appears to be the perfect material for high pressure microplasmas.

The main objective of this project was therefore to design a diamond microplasma device capable of operating above one atmosphere. A further, more adventurous goal was successful operation at ten atmospheres, a magnitude greater than the limit of most conventional devices.

If successful, such diamond based devices would provide an exciting opportunity to explore how microplasmas function at high pressures, a topic so far unexplored in the literature. As such, another challenging aim was to characterise the microplasmas and explain the observations.

Before delving into more detailed objectives, it is important to understand what microplasmas are, why they are useful and how they can be characterised. To achieve this, this section describes plasmas, gas discharge plasmas and microplasmas. It then considers microplasma devices, the applications of high pressure microplasmas and the possibility of arrays. Following this, the difficulties of high pressure operation are explored and how these can be circumvented by carefully selecting materials and gases. The current research in high pressure microplasmas is then summarised. Finally, the objectives of the project are covered in detail.

1.1   Introduction to Plasmas

Microplasmas are defined as glow discharges confined in at least one dimension to less than 1 mm.[2, 4] In order to understand the fundamentals of microplasmas, the basic principles of plasmas, and more specifically those classified as glow discharges, need to be covered.

1.1.1   What is a Plasma?

Plasma, often referred to as the fourth state of matter, is characterised by a gaseous mix of cationic, anionic and neutral molecules and atoms as well as negatively charged electrons. Despite the charges of the individual particles, the overall charges balance leading to a quasi-neutral medium.

The vast majority of matter in the universe (excluding dark matter) is in the plasma state; stars, including our sun, interstellar gas clouds and the Earth's magnetosphere all consist of plasmas.[5]

Owing to their low temperatures and pressures, natural terrestrial plasmas are rare, with the two most arresting examples being the aurora and lightning.[6] The most common terrestrial plasmas are artificially created gas discharges; plasmas have a huge range of applications, ranging from common fluorescent light bulbs to ion engines designed for spacecraft propulsion.[6]

1.1.2 Fundamental Parameters

Ordinary matter is usually characterised by three parameters: temperature, density and pressure. Plasmas, on the other hand, are more complex systems and thus almost always involve more parameters.[6] The fundamental parameters of plasmas are as follows:[7]

1. the temperature T_s of each species
2. the number density n_s of each species
3. the steady-state magnetic field B.

A huge variety of secondary parameters can be derived from these initial parameters; in some cases these secondary parameters are conceptually more accessible and easier to measure.

Plasma parameters span enormous ranges of many magnitudes. This is illustrated in Figure 1.1.[5]
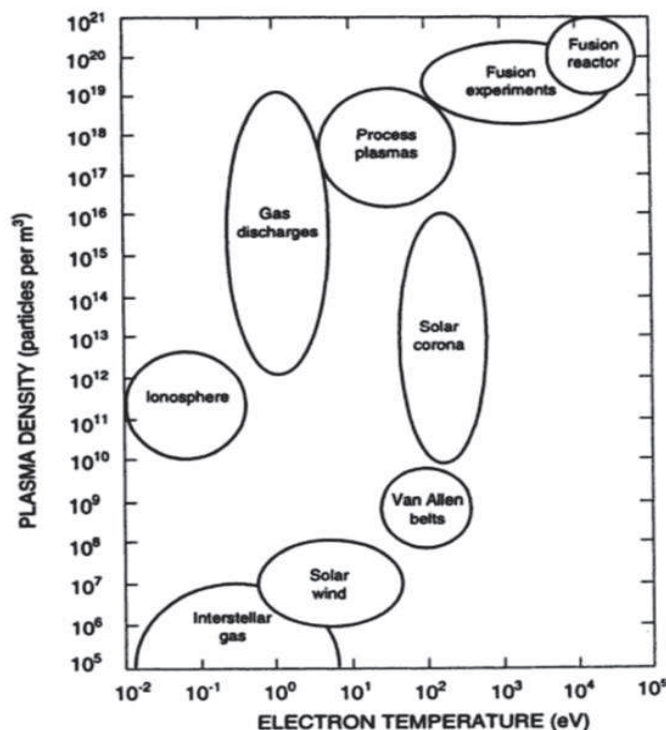
Figure 1.1. A logarithmic plot of electron density against electron temperature showing parameter ranges for a variety of both of both artificial and natural plasmas.[5]

1.1.3 Temperature

Although in terms of fundamental parameters the temperature of each of the plasma species should be considered separately, it is more appropriate to divide the species into two categories: electrons and heavier species. The efficient energy transfer between particles with similar masses means that, although neutral species do not interact with applied electric and magnetic fields, they are in thermal equilibrium with the heavier charged species.[8] As such, only one temperature for the heavier particles needs to be defined, this is called the gas temperature, T_g.

Conversely, the mass difference between electrons and heavier species is great enough to lead to inefficient energy transfer.[6, 9] This, coupled with the fact that energy deposition often favours the much lighter electrons, means that the electron temperature, T_e, and T_g can take very different values.[10]

The difference between these two values is dependent on how effective the energy transfer within the plasma is. This in turn is dependent on the rate and energy of collisions; a high frequency of collisions with a largely elastic nature will result in efficient energy transfer and similar values of T_e and T_g. As the gas density determines the frequency of collisions, increasing the pressure of a plasma can reduce the difference between T_e and T_g. This is shown in Figure 1.2.[11]
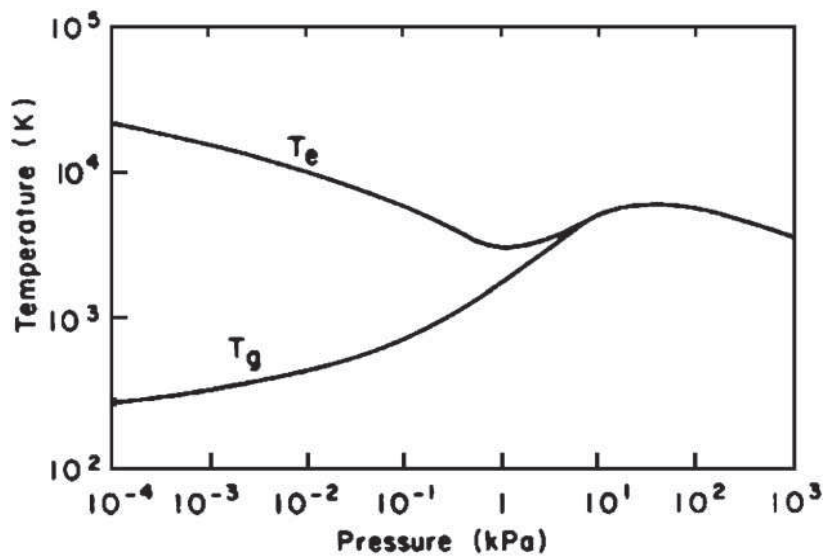
Figure 1.2. A plot of electron and gas temperature against pressure for a mercury plasma formed between two planar electrodes.[11]

Two different types of plasmas can be distinguished based on these temperatures. Where a thermal equilibrium is established between all species and $T_e = T_g$ the plasma is considered to be a thermal plasma.[12] In a thermal plasma the distribution functions of all species can be considered Maxwellian.[13] Arc plasmas are an example of thermal plasmas.[14]

Plasmas with $T_e \gg T_g$ are categorised as non-thermal plasmas. Glow discharges are a good example of non-thermal plasmas; these generally have much lower gas temperatures than thermal plasmas.[12] The distinction between whether a plasma is thermal or not is relevant when determining parameters and therefore important to consider when characterising a plasma.[15] Rather than following a Maxwell-Boltzmann distribution, electron energy

distributions of non-thermal plasmas are better modelled using a generalised Lorentzian distribution, which features a high energy tail.[16, 17]

Defined as glow discharges, microplasmas are non-thermal plasmas, with relatively low gas temperatures and non-Maxwellian electron energy distributions.[18] Examining Figure 1.2, it might appear that high pressure, non-thermal plasmas are implausible. This is not the case for microplasmas, as will be explored in later sections.

1.1.4   Density

Rather than consider the density of the combined species, it is more useful to consider solely the charged species, as these give the plasma its properties. On average the electron density (n_e) and ion density within a plasma are equal; this number is also known as the plasma density.[8]

1.2   Gas Discharge Plasmas

The most common method of creating an artificial plasma is simply to apply an electric field to a volume of gas. Plasmas generated in this method are referred to as gas discharges.[19] When the potential difference across the volume of gas is large enough, the resistance of the gas drops and the gas becomes conductive; a plasma is formed. The Townsend theory of plasma formation can explain how this occurs.

1.2.1   Townsend Theory of Plasma Formation

On their own, the electric fields applied are not strong enough to separate the gas into electrons and ions. Instead seed electrons are formed through the ionisation of atoms via cosmic rays.[20, 21] Further, if the energy present is greater than the work function, a property unique to the device material, electrons are emitted from the cathode.[22]
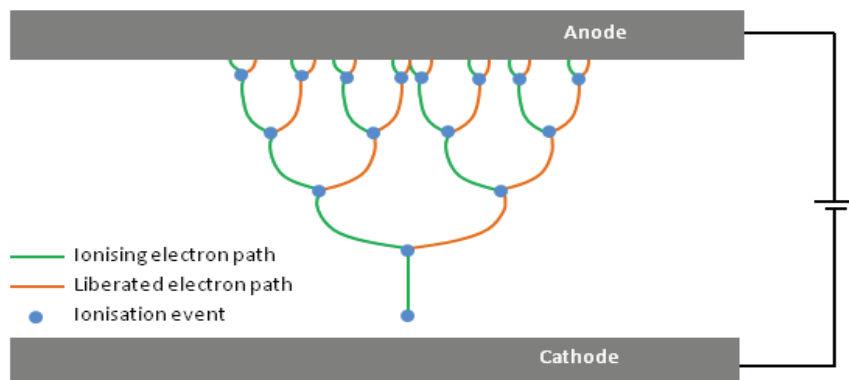
Figure 1.3. A depiction of an electron avalanche in which a seed electron near the cathode stimulates a series of ionisation events and the release of more electrons.

Seed electrons in the vicinity of the cathode are accelerated by the electric field. Collisions of these electrons with gaseous atoms can result in ionisation and the release of more electrons. These electrons are also accelerated, with further collisions producing even more electrons. This process of rapidly producing a large number of electrons is known as an electron avalanche and is illustrated in Figure 1.3.

Ionisation does not occur on every collision; elastic energy losses mean some electrons have less than the required energy. In these cases the atoms are excited temporarily to higher energy levels, returning to the ground state upon radiative emission.[20]

Positive ions formed in the primary avalanche may strike the cathode, liberating at least the number of electrons required for their own neutralisation. Any extra electrons released are called secondary electrons; these are accelerated in the electric field and form a further avalanche.[23] A positive layer of ions can build up on any insulating surfaces and stimulate further electron emission.[24]

Free electrons are constantly taken out of the system by recombination with heavier species or collisions with the anode. As such, for a plasma to be maintained, ionisation must occur continuously with constant electron avalanches. To maintain a stream of avalanches, the energy given to the electrons must be high enough and therefore the electric field strong enough. Consequently, there must be a minimum potential difference between the electrodes to strike a plasma. This potential difference is known as the breakdown voltage, V_b.[25]

Although a useful tool for understanding plasmas, recent calculations have shown that Townsend theory is not accurate.[26] More recent theories propose a combination of Townsend and streamer mechanisms in combination with initial excitation of metastables.[27]

1.2.2   Modes of Operation

Different modes of operation are observed in gas discharges. The mode is dependent on several factors, including electrode distance, gas pressure and the current flowing through the plasma. Modes can be used to describe the plasma. In a conventional gas discharge, three modes are usually observed: the Townsend discharge, the glow discharge and the arc discharge. By increasing the current of the discharge all three modes are displayed. Voltage-current (V-I) characteristics can be used to differentiate the modes as shown in Figure 1.4.[20]
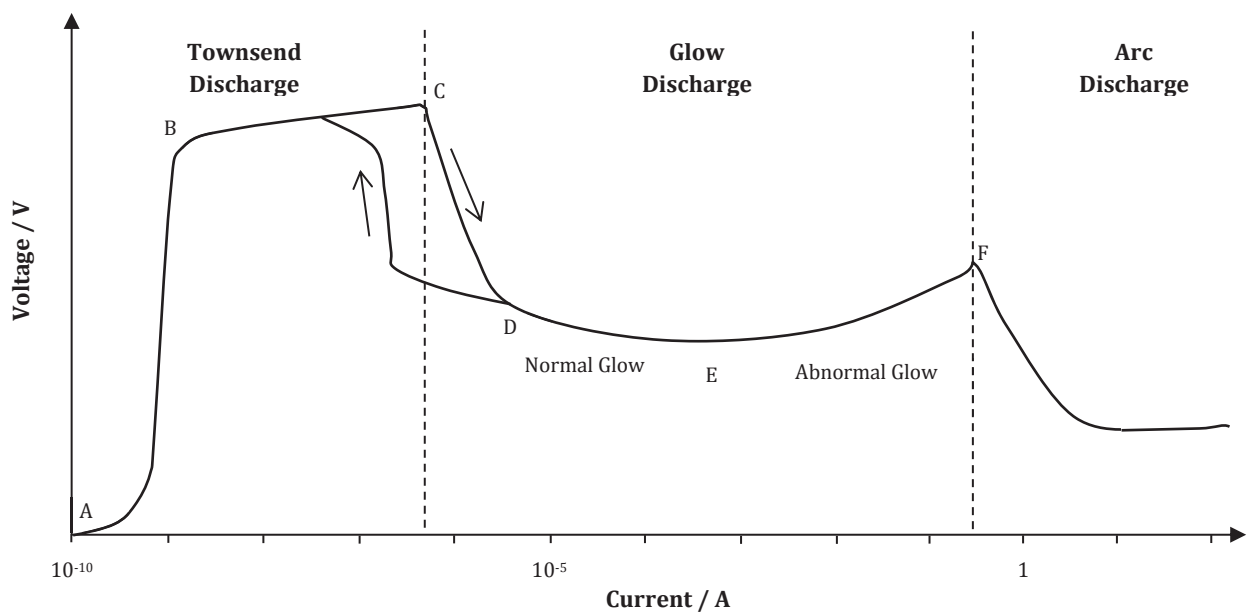
Figure 1.4. The V-I characteristic for a conventional discharge between two metal plates. The characteristic is divided into three clear modes. Adapted from Penning.[20]

5

The Townsend discharge, or predischarge, is the region spanning from A to C on the V-I characteristic. Very little light is given off during this regime, hence it is also known as a dark discharge.[28] Between A and B, the voltage is not high enough to cause avalanches and as such the only electrons in the field are those present in any environment, such as those from cosmic rays or radioactive sources. At B the breakdown voltage is reached followed by a sharp exponential increase in current between B and C as avalanches occur and the gas is ionised.

A rapid decrease in voltage with an increase in current between C and D marks the transition to a glow discharge. Hysteresis is seen on return of the discharge from the glow mode to the Townsend mode.[29]

The glow regime consists of two regions. The normal glow mode between D and E is characterised by a slight decrease in voltage with an increase in current. The normal mode shows a negative dynamic resistance, which is explained by the contraction of the plasma to give a higher current density and lower electric field strength.[30] The second region is the abnormal glow regime between E and F, characterised by a slight increase in voltage with current. A gas discharge in the glow mode is non-thermal and referred to as a glow discharge.

At F the cathode has become hot enough to emit electrons thermionically and an abrupt glow-to-arc transition occurs.[31] Arc plasmas are thermal plasmas, consisting of a direct channel of ionisation, characterised by high emission in the UV and visible light region.[20]

Microplasmas are glow discharges which tend to operate in both the normal and abnormal glow modes, although their V-I characteristics can differ greatly from Figure 1.4.

1.2.3 Regions within the Glow Mode

Although a glow discharge might be thought of as a diffuse, uniform plasma stretching between cathode and anode, this is not the case. In reality, several regions form between the electrodes. These regions are shown in Figure 1.5.[32] The luminosity across these regions varies depending on the processes carried out and the energies of the electrons carrying out these processes.
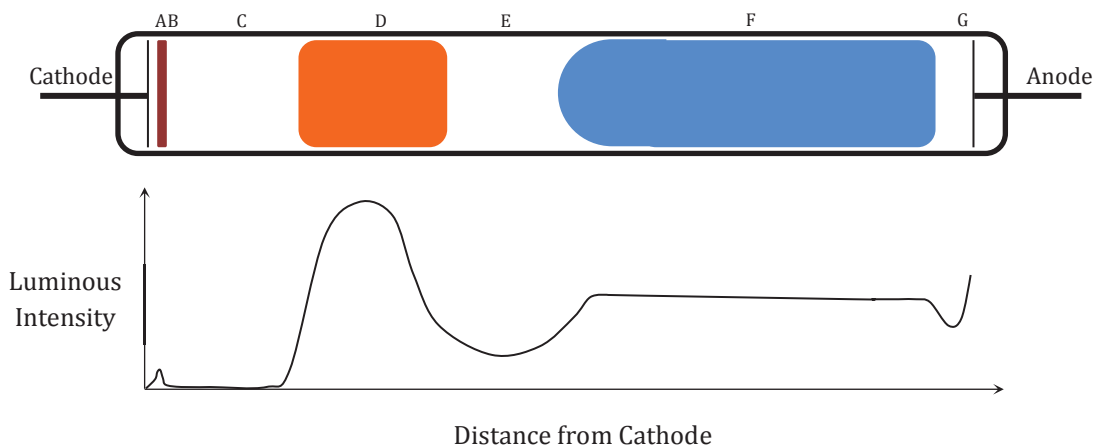
Figure 1.5. A diagram of a conventional DC gas discharge showing the regions between the electrodes: the Aston Dark Space (A), the Cathodic Glow (B), the Cathode Fall (C), the negative glow region (D), the Faraday Dark Space (E), the positive column (F) and the Anode Fall (G). A sketch of luminous intensity is shown directly below the diagram to illustrate differences in the light intensities given out in each region. Adapted from Boenig.[32]

Immediately next to the cathode is the very thin and non-luminous region (A): the Aston Dark Space. Electrons ejected from the cathode are accelerated away by the strong electric field. Overall, it has a negative space charge, meaning there are more electrons than ions; the electrons do not have enough energy to ionise atoms.[33]

The Cathodic Glow (B) is a thin luminous layer adjacent to the Aston Dark Space. Here electrons from the Aston Dark Space are accelerated to sufficient energies to excite neutral atoms on collision. Photons emitted upon relaxation of these atoms are the cause of the glow.

The Cathode Fall (C) is next in the sequence. It has a positive space charge, high ion intensity and low luminescence. The electric field is high in this region, consequently the electrons continue to accelerate towards the anode and positive ions towards the cathode, stimulating the release of secondary electrons. Throughout this region the electric field decreases to almost nothing, shielding the bulk of the plasma.

The most luminous region of the gas discharge is the negative glow region (D). The potential difference has dropped off by this region and the electrons are travelling at their maximum speeds with enough energy to ionise gas molecules and produce new, slower electrons. These slower electrons collide inelastically with gas molecules, exciting them and causing them to emit photons upon relaxation. Collisions within this region slow the electrons down until they are no longer travelling fast enough to excite atoms. At this point the region becomes the Faraday Dark Space (E), a region with excessive negative space charge as few ions are generated.[32]

Throughout the Faraday Dark Space the plasma density decreases and the electric field increases. In the positive column (F) the field has become strong enough to provide electrons with enough energy to excite atoms and once again cause luminescence.[25] This region is generally the largest, consisting of weakly ionised plasma. The Anode Fall (G) follows the positive column and features a drop in voltage. Electrons exiting the positive column gain energy in this region and collide with atoms to cause luminescence and generate ions which subsequently enter the positive column. No particles are emitted from the anode itself, it simply absorbs electrons.[32]

When the glow mode is compacted to sub-millimetre dimensions the regions are less well defined. However, they are still visible, particularly between planar electrodes.[34] When examining non-planar geometries, such as those with a hollow cathode, regions are more poorly defined.

In these devices the electric field is non-uniform and the structure is difficult to view. As such, a more simplistic description of the discharge is required; Lazzaroni & Chabert concluded that the discharge could be separated into two main regions: the positive column and cathode sheath.[35] The cathode sheath is the volume next to the cathode through which the electric field drops to zero, equivalent to the Cathode Fall region. The majority of the plasma bulk is referred to as the positive column.

1.2.4   Sputtering

Collisions between ions and the surface of the cathode not only produce secondary electrons, but also cause the ejection of atoms from the cathode. The initial collision of the ion with the

surface causes a series of internal collisions, leading to structural changes and possibly the ejection of an atom. This process is known as sputtering. [8]

Sputtering has several useful applications. The two most common are sputter etching, where sputtering is used to etch a pattern or thin a target, and sputter deposition where a thin layer of atoms is deposited from the cathode onto a substrate.[36, 37]

However, sputtering is less useful when operating microplasmas. The microscale of the devices makes them vulnerable to physical erosion, especially over long periods of use.[38] Furthermore, operation at very high pressures results in a higher plasma density and a greater number of sputtering collisions.

1.2.5 Collisions and the Mean Free Path

It should be clear from previous sections that the state and existence of plasmas, and especially gas discharges, are intrinsically linked to collisions within the plasma. For a more in-depth understanding it is useful to consider the mean free path. Defined as the average distance travelled by a particle between collisions, the mean free path is inversely proportional to the collision frequency.[39]

For a steady glow discharge the electron mean free path must be long enough to allow electrons to gain the energy required to ionize gas atoms. When reducing the dimensions of plasmas the mean free path becomes even more important as enough collisions must occur within the electrode separation to generate an electron avalanche.

In normal gases the mean free path is heavily dependent on the temperature and pressure of the gas, with increases in the velocity, density and cross section leading to increased collision frequency and a shorter mean free path. However, in plasmas, the presence of charged particles makes it slightly more complex. Pressure and velocity are still important, but a further feature is the effect charged particles have on each other and how large and penetrating this reach is. The Debye length is a useful parameter for explaining this effect.

1.2.6 Debye Shielding

A lone ion with a positive charge e will exhibit an electric field which attracts electrons and repels positive ions. In a vacuum this field will extend to infinity with the magnitude of the force exerted on the particle proportional to $1/r^2$, where r is the distance between the centre of each ion.[39]

When the ion is surrounded by a multitude of positive and negative charges its potential falls off far more rapidly. The distance over which the potential is reduced to $1/e$ of its initial value is named the Debye length, λ_D and for a plasma is defined by Equation 1.1.[8]

$$\lambda_D = \left(\frac{kT_e\varepsilon_0}{ne^2}\right)^{\frac{1}{2}} \tag{1.1}$$

where k is the Boltzmann constant, ε_0 the permittivity of free space, e the charge of an electron, T_e the electron temperature and n the plasma density. It is evident from Equation 1 that the denser the plasma the shorter the Debye length; for a highly ionised gas with $n \simeq 10^{16}$, $\lambda_D \simeq 10^{-4}$ mm, whereas for a poorly ionised glow discharge with $n \simeq 10^8$, λ_D can be up to 3 mm.[23]

A larger Debye length increases the number of electron collisions, and thereby reduces the electron mean free path. A strange effect in plasmas is that, unlike with normal gases, increasing particle speed can decrease collisions; faster electrons are more likely to have enough energy to travel unimpeded through an ion's coulombic field, and as such the collisional cross section is reduced.

Debye shielding is also the reason why the electric field decreases from the cathode to the Negative Glow region in a gas discharge. The Debye length for a stable plasma must be smaller than the dimensions of the plasma system itself and therefore becomes more important when considering microplasmas.[40]

1.2.7   Paschen's Law

Through his gas discharge investigations in the late 19th century Friedrich Paschen discovered an important relationship between the breakdown voltage, V_b and the product of pressure and gap length, $p \cdot d$.[41] The relationship is described by Equation 1.2 and can be visualised by the Paschen curve in Figure 1.6. [42]

$$V_b = \frac{a \cdot pd}{\ln(pd) + b}$$

(1.2)

where a and b are constants dependent on the gas composition. [43]
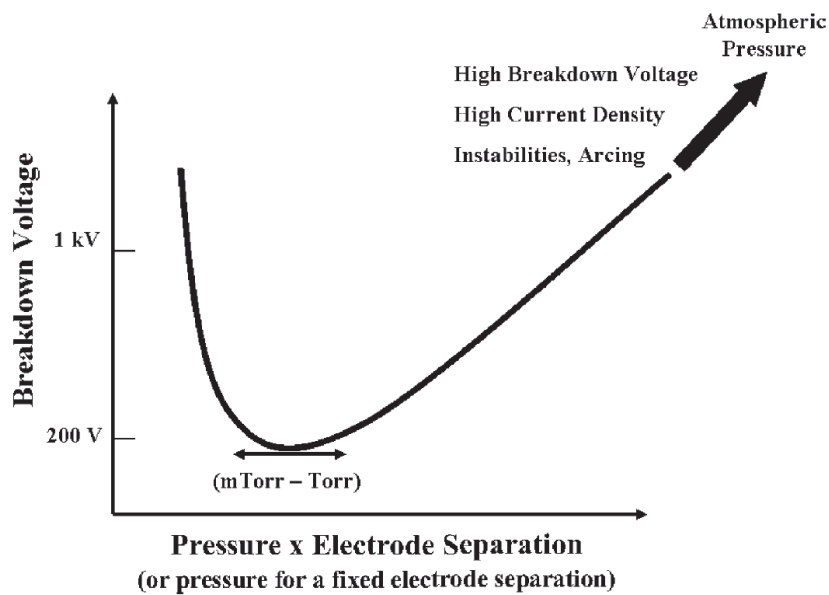
Figure 1.6. The Paschen curve showing the relationship between the Breakdown voltage (V_b) of a plasma and $p \cdot d$.[4]

At higher pressures and larger electrode separations, more collisions occur between the electrodes and the electrons have a shorter mean free path. At large values of $p \cdot d$, the high frequency of collisions means it is more difficult to accelerate electrons to the energies required to ionise the gas molecules, and a higher breakdown voltage is required.

At low $p \cdot d$ values the electrons have enough energy to ionise the gas molecules, but due to a long mean free path, may not collide with enough molecules to stimulate an electron avalanche.

Paschen's law indicates that the product $p \cdot d$ can be kept constant by reducing the gap between electrodes while increasing pressure. Microplasmas, by definition, have $d < 1$ mm. As such, the breakdown minima and general stability resides at higher pressures for microplasmas when compared with conventional glow discharges.

However, investigations have shown that at much smaller dimensions, with $d < 10$ μm, Paschen's law breaks down.[44, 45] At these micro-dimensions electron field emission plays a more important role in electron generation than in the traditional Townsend discharge. At higher pressures high numbers of positive ions near the cathode lower the potential barrier of emission and significantly increase the number of electrons emitted from the cathode.[46]

Consequently, modified Paschen curves, featuring a linear decrease in V_b with d at small electrode separations, can be applied in these circumstances.[47] Figure 1.7 shows the modified Paschen curve.[44]

Devices explored in this project had $d > 10$ μm and would therefore be expected to follow Townsend formation and exhibit a traditionally shaped Paschen curve.
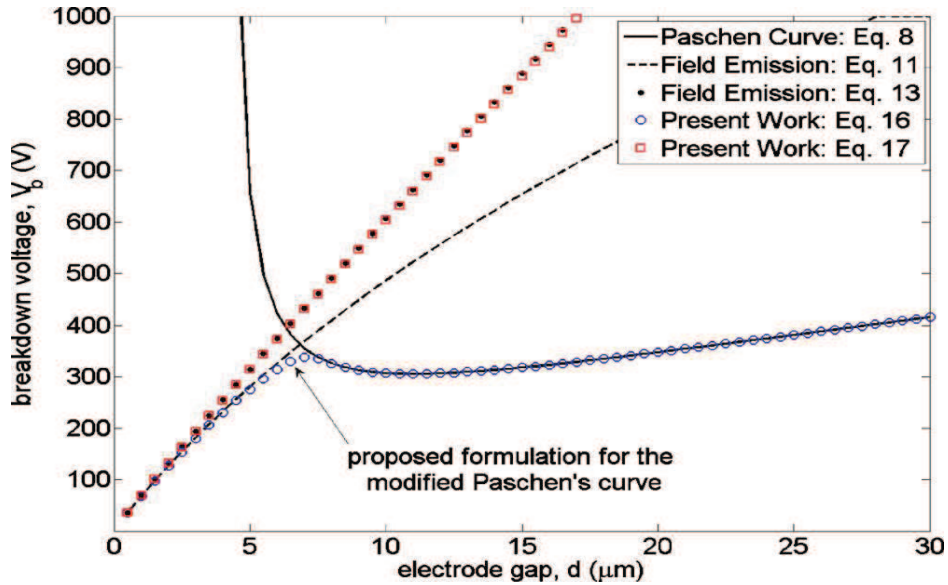
Figure 1.7. A comparison of the original Paschen curve and a number of modified curves taking field emission into account.[44]

1.3   Introduction to Microplasmas

Through the previous sections several key characteristics of microplasmas have become apparent. Firstly, they are non-thermal glow discharges in which $T_e \gg T_g$. Secondly, they can be characterised by V-I characteristics, and tend to show behaviour similar to the normal and abnormal glow regimes in conventional gas discharges. Thirdly, it is difficult to define regions within microplasmas and consequently only two main regions are frequently identified, the cathode sheath and plasma bulk.

Lastly, due to Paschen's law and $p \cdot d$ scaling, microplasmas are able to function at much higher pressures than conventional glow discharges. High pressure microplasmas tend to have much higher electron densities and a higher rate of excimer formation than conventional plasmas.[1] These properties are key features driving the development of microplasmas and their applications.

1.4 Microplasma Devices

Many different device types have been investigated in the literature. These are generally defined by the structure and geometries of their electrodes in addition to their frequency of operation.[48] Although efforts are being made to design more effective devices, there are five established device types: Micro Hollow Cathode Discharges (MHCDs), Cathode Boundary Layer Discharges (CBLDs), Dielectric Barrier Discharges (DBDs), radio frequency (RF) Capacitively Coupled Plasmas (RF CCPs) and RF Inductively Coupled Plasmas (RF ICPs).[49]

Of these device types, MHCDs are the best studied and most viable for high pressure operation. At high pressures the other devices form filaments, are highly vulnerable to sputtering or require large amounts of power to operate.[48, 50-52] The devices fabricated in this project followed a MHCD type geometry. Therefore, only MHCDs and their low pressure, more conventional counterpart, Hollow Cathode Discharges (HCDs) will be explored in detail in this section. Further information regarding the other devices can be found in Appendix I.

1.4.1 Hollow Cathode Discharges

In contrast to devices with planar electrodes, HCDs feature a cathode which contains a cavity. HCDs are operated using direct current (DC) and follow the geometry shown in Figure 1.8. They are defined as gas discharges between a cathode containing a hollow structure and an arbitrarily shaped anode.[2]
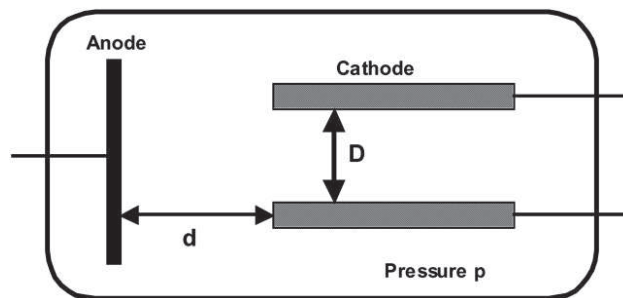
Figure 1.8. The general geometry of a conventional HCD.[2]

Stable HCDs have V-I characteristics similar to that shown in Figure 1.4. They are divided into three modes. Firstly, the predischarge is a Townsend discharge outside the cathode structure with an axial electric field between the two electrodes. In the predischarge mode, voltage increases with current.

Upon increasing the current, breakdown occurs and the discharge enters the cavity. A positive column forms along the cavity axis, acting as a virtual anode. The electric field changes from purely axial to radial throughout this transition; electrons travel in an oscillatory motion and

11

consequently have a longer effective path length and ionise a greater number of gas molecules.[53, 54] In this state the discharge is said to exhibit the Hollow Cathode Effect and be in the Hollow Cathode mode. A large increase in the emitted light intensity is observed in this mode, along with a negative differential resistance in which voltage decreases with increasing current, much like the normal glow region in a conventional gas discharge.[55]

After the cathode sheath has spread over the entire interior of the cavity it begins to cover to the surface of the cathode and, consequently, the V-I characteristic levels out. When the sheath has saturated the cathode surface, current increases with voltage. The discharge is now in the abnormal glow mode.[55]

In addition to Paschen's law, HCDs follow a second scaling law involving the product $p \cdot D$: The White-Allis similarity law, where $V = f(p \cdot D)$.[56] This law implies that depending on the electrodes, device geometry and gas, a stable HCD exhibiting the Hollow Cathode mode must have a $p \cdot D$ product between approximately 0.1 and 10 torr cm.[57]

1.4.2   Micro Hollow Cathode Discharges

MHCDs are miniaturised HCDs, typically with both d and $D < 1$ mm. At low pressures they obey the White-Allis similarity law and exhibit similar V-I characteristics to conventional HCDs, including the three previously established modes, shown in Figure 1.9.[58]
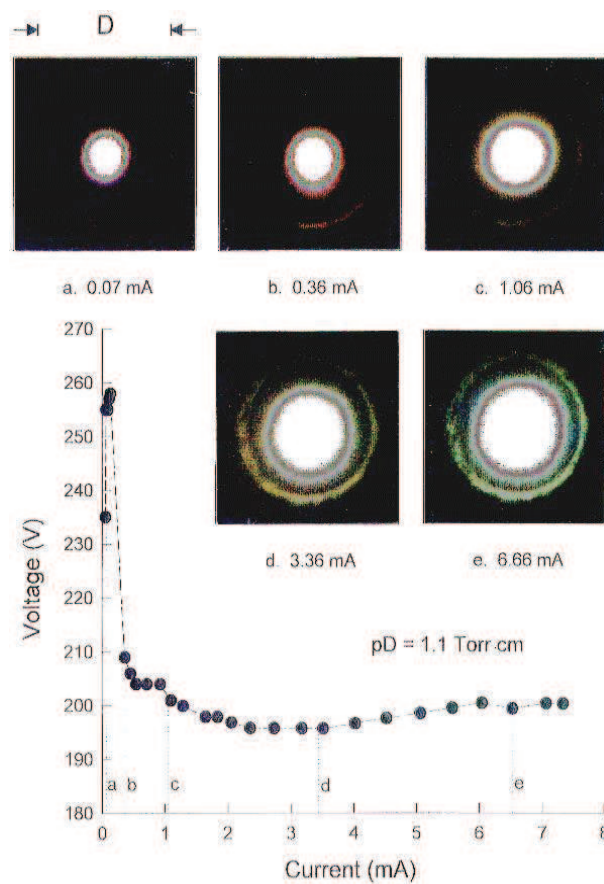
Figure 1.9. The V-I characteristic of a sandwich type MHCD operating in argon (56 Torr). The three modes characteristic of a conventional HCD can be resolved: the predischarge (a-b), hollow cathode mode (b-d) and the abnormal glow mode (d-e).[58]

However, for high pressure MHCDs, the upper limit of the White-Allis similarity law is reduced to 1.1 torr cm, meaning that for atmospheric pressure $D \lesssim 14$ μm. In circumstances where $p \cdot D$ is greater than 1.1 torr cm, the mean free path of the oscillating electrons is very short and they are unable to gain enough energy to ionise the gas molecules.[58, 59]

To date, the requirement for such a small cavity has restricted atmospheric pressure experiments to investigating MHCDs with $p \cdot D > 1$ Torr cm, a value too low for the discharge to display the classical Hollow Cathode Effect. V-I characteristics of these discharges tend to differ from those of conventional HCDs, and depending on operating parameters, from each other.

In many investigations, V-I characteristics display only flat or positive gradients following the predischarge mode. In the majority of these cases the discharges are said to exhibit only the normal or abnormal glow modes.[60-62] However, other authors conclude a mode unique to high pressure operation is exhibited; Greenan *et al.* identified the regime as High Pressure Hollow Cathode (HPHC) operation due to the uniform plasma distribution across the hollow.[63]

Negative differential resistances have also been observed. These regions have been attributed to a confined abnormal to normal mode transition or, more recently, the self-pulsing mode.[59, 64-71]

Initially found by Hsu *et al.* and investigated more fully by Aubert *et al.*, the self-pulsing mode features consistent oscillations in both current and voltage, shown in Figure 1.10.[64-66] The oscillations feature an initial increase in sustaining voltage with time. During this period the current is very low and the plasma completely confined to the hole, as shown in Figure 1.11a. Once a certain voltage is reached a sharp current pulse is observed, accompanied by a steep drop in sustaining voltage. During this pulse the plasma emerges from the cavity and swells onto the cathode surface (Figure 1.11b-e). The current then drops to the previous low value, accompanied by contraction of the plasma (Figure 1.11d-f).
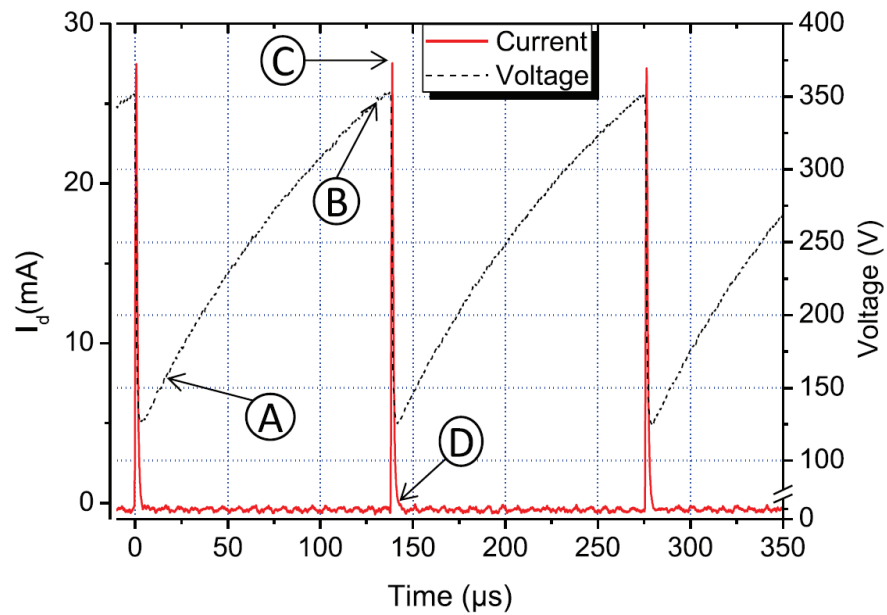
Figure 1.10. Current and voltage plots against time for the self-pulsing mode observed for a MHCD operating under helium (200 Torr).[65]
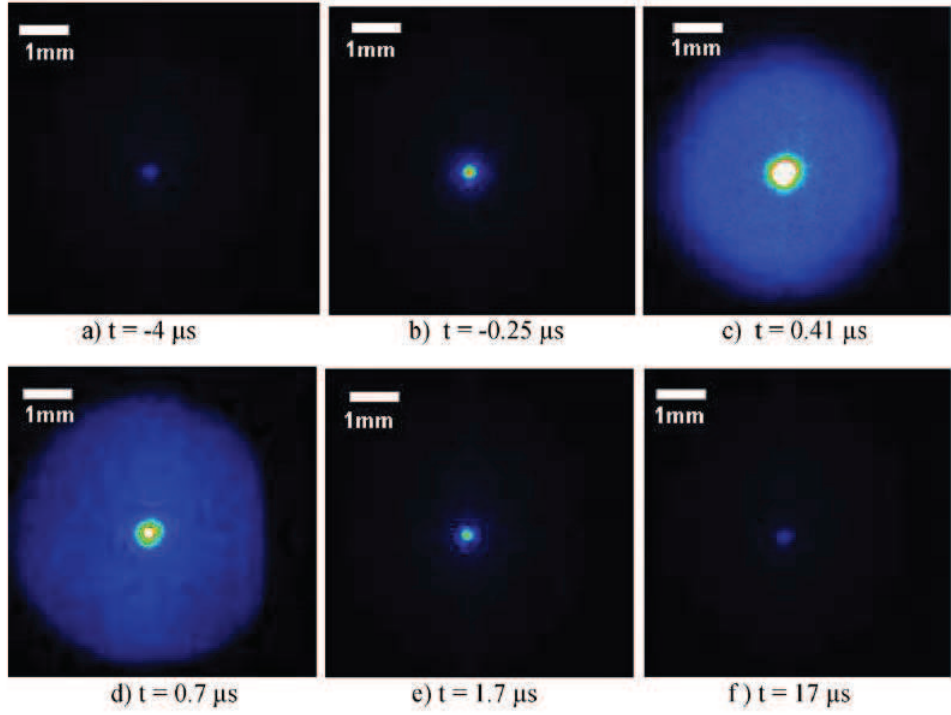
Figure 1.11. CCD images of the cathode of a MHCD operating in the self-pulsing mode under argon (40 Torr). a) and f) show the discharge at low current and increasing voltage, whereas b) to e) show the current pulse.[66]

Similar to the Hollow Cathode mode, the self-pulse regime is exhibited following predischarge. It is important to note that the current measured and recorded on the V-I characteristics is not constant DC, but the average current. A further characteristic of this regime is the dependency of the oscillation frequency on average current and pressure; Aubert *et al.* found the frequency to increase with average current.[66]
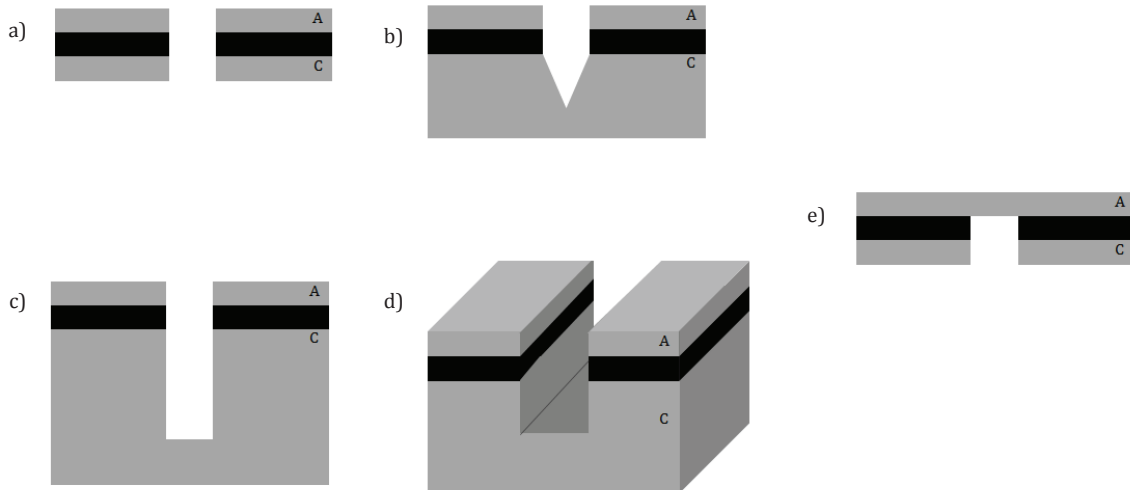
Figure 1.12. Common MHCD designs: sandwich (a), inverted pyramidal (b), vertical cavity (c), trench (d) and planar anode (e).

A variety of geometries have been explored for MHCDs, shown in Figure 1.12. One of the most common is a sandwich type device consisting of a cylindrical cavity with a conductor/insulator/conductor structure (a).[2, 61, 72] Other variations include the inverted pyramidal MHCD (b)[73, 74], vertical cavity MHCD (c)[74-76], trench type MHCD (d)[74, 75] and planar anode MHCD (e).[77, 78] The geometry explored in this project is most similar to the planar anode structure, but features a longer cathode.

1.5   Applications of High Pressure Microplasmas

The previous sections have explored in detail what microplasmas are and why they can function at high pressure. But why are they useful? The potential applications of high pressure ($\geq$ 1 atm) microplasmas (HPMs) stem from four sought after properties:

1. Efficient production of high energy radiation
2. A high electron density for use in plasmachemical processing
3. The ability to operate in atmospheric air
4. Compact size for use in miniaturised devices

The first two of these properties especially might benefit from the investigation of higher than atmospheric pressure microplasmas. The following section will examine each of these properties and the potential applications associated with them in turn.

1.5.1   Radiation Sources

The high concentrations of energetic electrons coupled with dense gas molecules leads to a fast rate of excimer formation in HPMs. As such, they can produce large amounts of excimer radiation, with the majority in the UV region. The radiation produced can be used directly as UV for applications such as water purification[79] and photocatalytic processes or converted into visible light by phosphors for use in display panels.[80, 81]

Recently arrays have been adapted to commercial lighting and flat arrays of up to 12" × 12" are being manufactured. These arrays are marketed as 'light tiles' and provide a long lived, efficient and uniform source of light. In addition to opening up design possibilities unavailable for conventional lighting (Figure 1.13), these light panels are used in videography and product inspection.[1]

Figure 1.13. An unconventional chandelier featuring eight 6"×6" 'light tiles'.[1]

Microplasmas operated in series result in increased excimer emittance. Von Allmen *et al.* produced a device with seven microdischarges arranged optically in series which amplified one of the Xe^+ transitions.[82] The ability of a microplasma array to produce gain indicates that a high

pressure array with well-designed cavities and reflectors could function as a miniature excimer laser.[83]

1.5.2 Plasmachemical Processing

The electron density within microplasmas increases with pressure.[84] Consequently the electron densities found within HPMs are extremely high, regularly in excess of 10^{14} cm^{-1}.[1] These high electron densities can be utilised in low power plasmachemical processing.

Figure 1.14. Photograph of a 12-channel microplasma ozone generator operating in 1 atmosphere of O_2.[88]

Several studies have examined the reforming of simple molecules within high pressure MHCDs. These have included the reforming of CO_2, methanol and ammonia.[85-87] Although moderately successful, inconsistencies in plasma stability and short device lifetime were common issues with these devices.

A more promising use of microplasma reactors is for the generation of ozone for water purification; Kim *et al*. fabricated arrays of microplasmas in Al/Al_2O_3 (Figure 1.14) which were used to generate ozone at rates and efficiencies competitive with current large scale DBD reactors.[88]

1.5.3 Operation in Ambient Air

Certain applications require operation in ambient air. One such application where this is required, in combination with high electron densities, is in the destruction of organic and biological compounds. For use in air regeneration systems, several atmospheric pressure microplasma arrays have been used to destroy volatile organic compounds (VOCs) efficiently and with high destruction rates.[89-91] Furthermore, preliminary investigations into the destruction of highly resistant biomolecules, such as prions, have also been successful and could establish atmospheric pressure microplasmas as a primary sterilisation tool.[92-94]

1.5.4 Compact Size

The recent expansion of 'lab-on-a-chip' research, particularly within analytical chemistry, has driven investigations into the use of atmospheric pressure microplasmas as analytical detectors, both for trace contaminants and other micro-chemical analysis.[95] Several contaminants have

been detected by microplasmas, including halogenated hydrocarbons, pesticides and toxic metals.[96-98]

1.6   Arrays

Many of the aforementioned applications require microplasmas arranged in arrays. Operation in both series and parallel is possible. If the microplasmas are operating in a mode with flat or positive differential resistance (*e.g.* predischarge) no individual ballasts are required for parallel operation.[60, 99]

However, when functioning in the abnormal glow mode the cathode surface must be covered with a dielectric layer to constrict the plasma to the cathode.[2] Arrays of this kind operated with DC tend to have poor power distribution between microplasmas. Conversely, alternating current (AC) provides more consistent operation and has been used in arrays with as many as 40000 discharges, shown in figure 1.15.[100]

Arrays operating in modes with a negative differential resistance require individual ballasts.[101] Series operation of plasmas in both positive and negative differential modes also requires individual ballasts and provides increased excimer emittance.[102]

Fabrication of individually ballasted devices is difficult and currently restricts the size of arrays and materials used. However, the use of semiconductor processing techniques could allow the economically feasible production of these arrays in silicon.[99, 103]
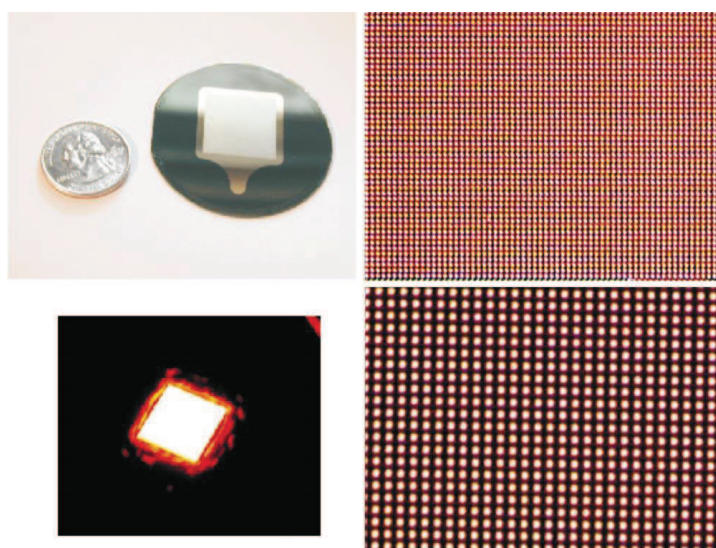
Figure 1.15. A 200 × 200 array of microplasmas fabricated in silicon and operated under AC in Ne (700 Torr). Images on the left are photographs of the device before and during operation. On the right are optical micrographs of sections of the array.[100]

1.7   Difficulties of High Pressure Operation

Two major difficulties are encountered when operating microplasmas at high pressure: firstly, HPMs are vulnerable to arcing and, secondly, a large amount of damage is incurred through high thermal energies and sputtering.

1.7.1 Instabilities and arcing

At higher pressures arcing occurs more readily via the glow-to-arc transition, identified in Figure 1.4. During this transition the plasma turns from a non-thermal, poorly ionised glow discharge to a thermal arc with a high ionisation fraction.

The transition is primarily a cathode effect. Increased electron emission from the cathode results in a greater number of electron avalanches. Ions produced during these discharges increase the positive space charge and electric field near the cathode. If a high enough current density is already established, the increase in field strength can stimulate the release of another electron. A positive feedback loop is established where the number of emitted electrons increases and becomes far greater than the amount required for glow operation and a direct channel of ionisation (an arc) forms.[104, 105]

Thermionic emission of electrons from the cathode is one of the foremost reasons for increased field emissions. As such, increases in cathode temperature can cause a discharge to lose stability. Microplasmas acting at higher pressures are vulnerable to cathode heating due to increased collisions and energy transfer between both electrons and heavier species and heavier species and the cathode.[4] To reduce this effect, thermally conductive materials can be used to transfer heat away from the cathode surface.

1.7.2 Device Damage

Higher pressures lead to a larger number of ion-electrode collisions and the high surface-to-volume ratio means that electrode damage has a more substantial effect on discharge stability and device lifetime.[106, 107]

Furthermore, HPMs, although still non-thermal, tend to have much higher gas temperatures than their conventional counterparts. At high pressures more elastic neutral-electron collisions lead to Joule heating and efficient energy transfer between electrons and heavier species.[108, 109] A much higher proportion of electron-neutral collisions occur in the cathode sheath. Consequently, gas temperatures and power densities in this region are higher than in the positive column and can be in excess of 1200 K at atmospheric pressure (Figure 1.16).[109-111]
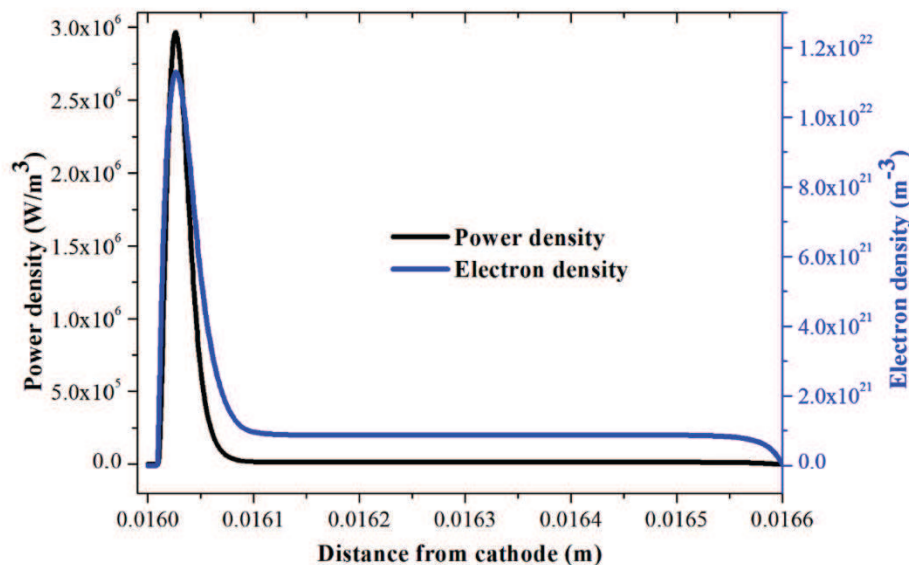
Figure 1.16. How power and electron density vary depending on distance from cathode simulated for an argon microplasma operating at atmospheric pressure.[109]

It is likely these harsh conditions have been the limiting factor for investigations probing microplasma operation at pressures higher than atmospheric pressure. One method to reduce device damage is to use a material which can withstand high temperatures and sputtering.

1.8 Materials

It should be evident from the previous section that material choice is key for successful HPMs. To minimise damage, materials should be resistant to sputtering, capable of withstanding very high temperatures and have good thermal conductivity to dissipate heat away from the aperture. Although still relevant at the dielectric and anode, these properties are most important when considering the cathode. It is here that sputtering occurs and the highest gas temperatures are observed. A recent model by Mobli *et al.* showed electrode material can greatly influence gas temperature.[112]

Microplasmas rely on secondary electron emission from the cathode. The amount of electrons released relates to the secondary electron coefficient, γ.[113] In turn γ is dependent on the material work function, *i.e.* the energy required to remove an electron from the material surface. A higher work function generally means a lower secondary emission coefficient and a less stable discharge.[114] Consequently, materials with lower work functions are more likely to form stable discharges.

Further properties to take into account are the conductivity of both the electrodes and insulators, the machinability and how inert the material is.

1.8.1 Metals

In the majority of cases, microplasma electrodes are fabricated from metals. Metals have good electrical conductivity and machinability but tend to sputter easily.[48] Molybdenum is the most commonly chosen metal, due to its high thermal conductivity and melting point (Table 1.1). However, it is still vulnerable to sputtering.[115]

Table 1.1. Common electrode metals and their properties.[115]

Element	Work function (eV)	Melting point (°C)	Thermal conductivity ($W\ cm^{-1}\ K^{-1}$) at 27 °C	Thermal expansion coefficient ($K^{-1} \times 10^{6}$) at 25 °C
Al	4.3	660	2.37	23.1
Au	5.1	1064	3.17	14.2
Fe	4.5	1538	0.80	11.8
Mo	4.6	2617	1.38	4.8
Ni	5.1	1453	0.91	13.4
Re	5.0	3180	0.48	6.2
Ta	4.2	2996	0.57	6.3
W	4.5	3422	1.74	4.5

1.8.2 Silicon

Another popular material is silicon, first chosen due to its good thermal conductivity and resistance to sputtering.[76] Easy machinability combined with established integrated circuit fabrication techniques make silicon a promising candidate.[116] Furthermore it can be doped and converted into a (semi)conductive material.[117, 118]

Despite these promising properties, investigations have found that even with its high melting point of 1410 °C the cathode surface is damaged by localised melting at pressures as low as 400 Torr.[3, 119] Consequently, a more resilient material is required.

1.8.3 Diamond

One row up from silicon lies carbon. Diamond, the carbon allotrope most similar in structure to elemental silicon, has a variety of superlative properties which make it a superb candidate for HPMs, shown in table 1.2.[120-122] Many of these properties are similar to those valued in silicon, but far exceed them in terms of magnitude.

Table 1.2. The superlative properties of diamond useful to HPMs.[120-122]

Property	Use in HPMs
High melting point (4400°C)	Able to withstand high temperatures and reduce events of localised melting.
Highest known thermal conductivity (20 W cm^{-1} K^{-1} at 298 K)	Dissipates heat away from the plasma to reduce gas temperature.
High radiation hardness	Reduces sputtering damage.
Low thermal expansion coefficient (0.8 ×10^{-3} K^{-1} at 298 K)	Reduces deformation and structural damage at high temperatures.
Excellent insulator (10^{16} Ω cm)	A large band gap ensures high resistance for use as a strong electrical barrier between the electrodes.
Resistant to chemical corrosion	Undamaged upon exposed to acid for oxidative cleaning.
Ability to be doped	Can be doped to alter resistivity and enable use as both electrode and insulating layer.
Relatively low work function and negative electron affinity	Gives a high secondary electron yield, γ, providing discharges with extra stability.

For the basis of this project, the most important properties are the high melting point, thermal conductivity and sputter resistance which should enable devices to function at high pressures without being destroyed.

A further key property is the ability to control the electrical conductivity by doping. In this project, metallically conductive, boron-doped diamond was used in the electrodes. Upon doping, carbon atoms in the lattice are substituted for boron and consequently impurity states are introduced between the valence and conduction bands. The impurity states reduce the band gap and form a p-type semiconductor. At heavy doping concentrations the impurity states merge to form a continuous impurity band, which widens with increasing concentration. At a

certain concentration ($\sim 10^{21}$ cm^{-3}) the impurity band reaches the valence band, abolishing the band gap and forming metallically conductive diamond.[123, 124]

Both doped and un-doped diamond can be grown consistently using Chemical Vapour Deposition (CVD), a well-established technique used to synthesise diamond.[121] Use of CVD makes it possible to create a fully diamond microplasma device with the conductive components made of boron-doped diamond (B-diamond) and the insulating components made of un-doped diamond (Figure 1.17).[125] One disadvantage of diamond is its poor mechanical machinability, however, this can be bypassed using laser machining.[126]

Figure 1.17. A diagram of the MHCD type device fabricated solely from diamond by Mitea *et al.*[125]

Despite the many advantages of diamond, few examples of diamond devices exist in the literature. Mitea *et al.* fabricated a MHCD type device with a sandwich B-diamond/un-doped diamond/B-diamond structure out of microcrystalline diamond, shown in Figure 1.17, and found the discharge produced to have characteristics similar to typical MHCDs.[125]

Instead of using doped diamond as a conducting material, Chang *et al.* used ultra-nanocrystalline diamond for the cathode of a microplasma device and found it gave improved plasma illumination compared with silicon devices.[127] Lastly, Hatta *et al.* investigated a conventional gas discharge with a B-doped diamond cathode and found hydrogen-terminated surfaces to provide lower sustaining voltages.[128]

This project is the first investigation into the use of diamond in microplasmas operated well above atmospheric pressure and consequently will determine how feasible diamond is as a HPM material.

1.9 Gases

The majority of microplasmas are operated in noble gases, such as He, Ne, Ar and Xe. Not only do these gases provide a simple chemical environment, they also produce low temperature plasmas.

Operation in ambient air, although a key target for developing applications, is difficult. Large numbers of reactive molecules cause greater device damage and ensure little of the electron energy goes into ionising collisions.[38] Consequently, although several designs have been operated successfully, the stability of the plasmas formed is questionable.[38, 69, 129, 130]

The most promising gas candidate for operation far above atmospheric pressure is helium. A low atomic mass ensures good thermal conductivity in addition to a low sputter rate.

Additionally, helium has an ionisation energy of 24.6 eV, much higher than those of other noble gases.[131] Consequently a lower ion density is observed within the plasma and the likelihood of arcing is reduced. For these reasons, helium was chosen as the gas used in this project.

1.10 Characterisation

Two common microplasma diagnostic tools were used in this experiment and will be explored in this section: Optical Emission Spectroscopy (OES) and current-voltage measurements. OES is frequently used to quantify gas, electron and excitation temperatures in addition to electron density. Current-voltage measurements are used to obtain V-I characteristics for evaluating operating modes as well as Paschen curves.

Other techniques often used to measure species' temperatures and densities include laser Thompson scattering and diode laser absorption spectroscopy. [132, 133] However, these will not be explored in this project.

1.10.1 Gas Temperature

The most common method for quantifying gas temperature in microplasmas uses the fine structure of the N_2 (C $^3\Pi_u \longrightarrow$ B $^3\Pi_g$) transition, a well-studied transition with known constants in a non-congested region of the spectrum. If a vibrationally resolved spectrum can be obtained using OES, a synthetic spectrum with the rotational temperature, T_R, as the free parameter can be fitted to the spectrum. The best fitting spectrum should have an accurate T_R.

If N_2 is in equilibrium with the bulk gas, T_R is approximately equal to the kinetic gas temperature of the plasma; this is often the case as rotational relaxation is much faster than vibrational and electronic transitions. Noble gas plasmas diagnosed using this technique often have trace amounts of N_2 already present as a result of imperfect vacuum systems, or have small amounts added.[134]

Gas temperatures tend to range between 350 and 2000 K, with higher pressure microplasmas often exhibiting higher temperatures.[2] It is important to note that any OES measurements correspond to the brightest part of the plasma, which may not necessarily be the hottest part.

1.10.2 Electron Density and Temperature

A phenomenon known as Stark broadening can be used to measure both the electron temperature and density. Often the H_β and H_γ lines in either the Balmer or Lyman series are measured by OES and analysed.[135-138] Due to limitations in spectroscopy resolution as well as time restraints this diagnostic was not utilised in this project and will therefore not be covered further in this section. A more in-depth review can be found in Appendix I.

In microplasmas electron densities tend to be around $10^{14} - 10^{16}$ cm^{-3} and average electron temperatures roughly 1 eV (11 600 K).[1, 2]

1.10.3 Excitation Temperature

The electronic excitation temperature, T_{exc} is a parameter more easily determined than T_e and n_e. T_{exc} is the temperature associated with the distribution of excited electrons within gaseous

atoms. It is therefore possible to measure T_{exc} by comparing the intensity of spectral lines attributed to transitions featuring different upper energy levels.

If the excitation processes controlling the excited state distribution are primarily the result of electron collisions, it follows that T_{exc} must be closely linked to T_e.[139] Indeed, in thermal plasmas T_e is equal to T_{exc}. However, when plasmas deviate from thermal equilibrium the relationship is less clear, with T_e varying between two and six times greater than T_{exc} depending on pressure, power and device type.[140] Despite this, the dependency of T_{exc} on parameters such as pressure could be used to infer the dependency of T_e on the same parameters.

The Boltzmann plot method is the most common technique for determining T_{exc} and the method used in this project. Assuming the energy levels of the measured species follow a Boltzmann distribution, the intensity of a spectral line associated with a transition from an upper level q to a lower level p can be determined by Equation 1.3:

$$I_{qp} = \frac{d}{4\pi} A_{qp} \frac{hc}{\lambda_{qp}} n \frac{g_q \exp\left(-\frac{\varepsilon_q}{kT_{exc}}\right)}{Z} \qquad (1.3)$$

Where I_{qp} is the line intensity, d is the source depth, A_{qp} the Einstein coefficient reflecting the transition probability, h is Planck's constant, c is the speed of light, λ_{qp} the transition wavelength, n is the particle number density, g_q and ε_q are the statistical weight and energy level, respectively, of the upper energy level, k is the Boltzmann constant, T_{exc} the absolute excitation temperature and Z the partition function.[141]

Introducing logarithms and rearranging equation 1.3 gives Equation 1.4:

$$ln\frac{I_{qp}\lambda_{qp}}{g_q A_{qp}} = ln\frac{dhcn}{4\pi Z} - \frac{\varepsilon_q}{kT_{exc}} \qquad (1.4)$$

Following Equation 4, a plot of $ln(I_{qp} \cdot \lambda_{qp}/g_q \cdot A_{qp})$ against ε_q gives a straight line with slope of $-1/kT_{exc}$. Hence T_{exc} can be determined.

1.10.4 V-I characteristics

As described in detail in Sections 1.2.2 and 1.4.2, V-I characteristics are often used to determine the mode of operation. Due to power supply limitations they are often measured by altering the voltage and measuring the current. Despite this characteristics are often interpreted as how sustaining voltage alters with current.

In this investigation the power supply was capable of operating in current-driven mode. Consequently, V-I characteristics were obtained by altering the discharge current and measuring the voltage. Using this method it was possible to display real-time V-I characteristics on the oscilloscope by constantly varying current using a triangular waveform.

1.11 Current Research into High Pressure Microplasmas

Although many atmospheric-pressure microplasmas have been investigated, there are few examples of microplasmas operating above 1 atm. The reason for this is most likely due to the inability for conventional devices to withstand the high temperatures and pressures.

However, examples do exist. Park & Eden investigated a range of MHCDs under pressures reaching 1200 Torr. [142] Kosarev *et al.* studied nanosecond microdischarges in synthetic air at pressures between 1 and 5 atm for the application of combustion initiation. However, due to the short discharge lifetime it is unclear if these were stable or even operating in the glow discharge regime.[143]

The lack of investigation into plasmas operating above 2 atm gives the most enticing reason for studying HPMs: they represent an unexplored frontier.

1.12 Project Objectives

As mentioned earlier, the overarching aims were the fabrication of diamond microplasma devices capable of operating above atmospheric pressure and the characterisation of these high pressure plasmas. In order to accomplish these aims, it was necessary to break the project down into more manageable objectives.

These were as follows:

1. Design and fabricate microplasma devices adhering to the following criteria:
    - A MHCD type geometry
    - Components exposed to high temperatures (cathode and dielectric) made out of diamond
    - Good electrical contact between device and circuitry
    - Capable of consistent breakdown
    - A range of aperture sizes

2. Develop and fabricate a device of similar design consisting of an array of microplasmas.

3. Operate the devices at pressures of up to ten atmospheres.

4. Characterise the microplasmas using the following techniques:
    - Voltage and current measurements to obtain Paschen curves and V-I characteristics
    - OES measurements to determine species' temperatures and densities

5. Explain the microplasma characteristics in terms of their fundamental physics and by comparing them to well-characterised microplasmas operated at lower pressures.

6. Assess the feasibility of diamond as a material used to fabricate microplasma devices by observing damage after high pressure operation.

2 Experimental

2.1 Device Conceptualisation and Design

Initially diamond devices were fabricated following the design and methods of Mitea *et al.*[125] Although the devices often struck successfully, the life-time was poor. After operating for only a couple of hours the devices would short, most likely due to graphitisation. Instabilities were common, with regular arcs forming between the electrodes and around the device. A new device, explained below, was designed to solve these short comings.

A miniaturised version of a conventional HCD device was chosen as the basis of the design, shown in Figure 2.1. Unlike most MHCD devices seen in the literature it was made up of two separate components. The cathode/dielectric part consisted of a thick cathode (~ 600 μm) with an insulating layer (40 – 60 μm) on one side and an aperture in the centre. The separate anode was a planar piece of conducting material onto which the dielectric layer was held. For the most part the cathode/dielectric component will be referred to here as the 'device' or 'sample'. The molybdenum anode was unmodified throughout measurements.

The highest plasma temperatures are observed near the cathode. As such it was only necessary for the cathode/dielectric to be fabricated out of diamond. Molybdenum was chosen as the anode material due to its good conductivity and heat resistance.[115] The hollow cavity is deeper than previously studied MHCDs. It was thought that the increased surface area within the cavity might increase the stability of the discharge and ensure efficient energy transfer from the plasma to the diamond.
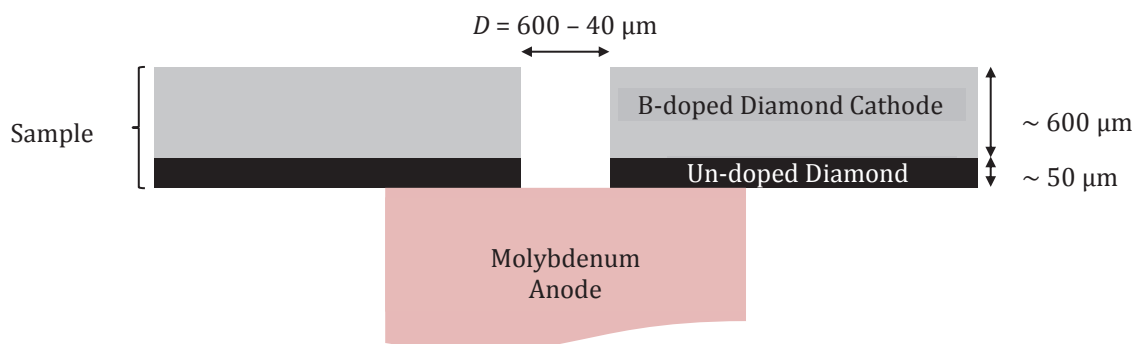
Figure 2.1. The final design consisting of two parts. The cathode/dielectric sample contains a thick, 600 μm B-diamond cathode with a 50 μm insulating un-doped diamond layer. The planar anode is separate and made of molybdenum.

2.2 Device Fabrication

Scheme 2.1. The overall fabrication process of the diamond samples. B-diamond is represented by grey and un-doped diamond by black.

Samples were fabricated following Scheme 2.1. Electrochemical grade, microcrystalline boron doped diamond samples (10 × 10 × 0.6 mm) were acquired from Element Six. Prior to CVD they were acid washed in a solution of HCl (3 M) and HNO$_3$ (4 M) at 50 °C for ca. 20 minutes to remove any metal particles that had become attached to the surface during the production process.

2.2.1   Diamond deposition

The un-doped diamond layer was grown using microwave enhanced CVD. Flow rates of 40, 25 and 500 sccm min^{-1} for argon, methane and hydrogen, respectively, a pressure of ~125 Torr and temperature of ~800 °C were chosen to ensure a consistent, microcrystalline diamond layer was deposited at a fast rate (~ 5 μm hour^{-1}). Between one and four samples were coated at the same time, with the samples placed in the centre of the reactor to ensure an even film. Deposition lasted for at least ten hours to deposit a film of roughly 50 μm. An ohmmeter was used to test the resistance of the samples and showed that the un-doped diamond layer was thick enough to insulate the cathode well. Scanning Electron Microscopy (SEM) images of the insulating layer (Figure 2.2) showed it was well-defined. The similar texture of the diamond suggests similar crystal sizes.
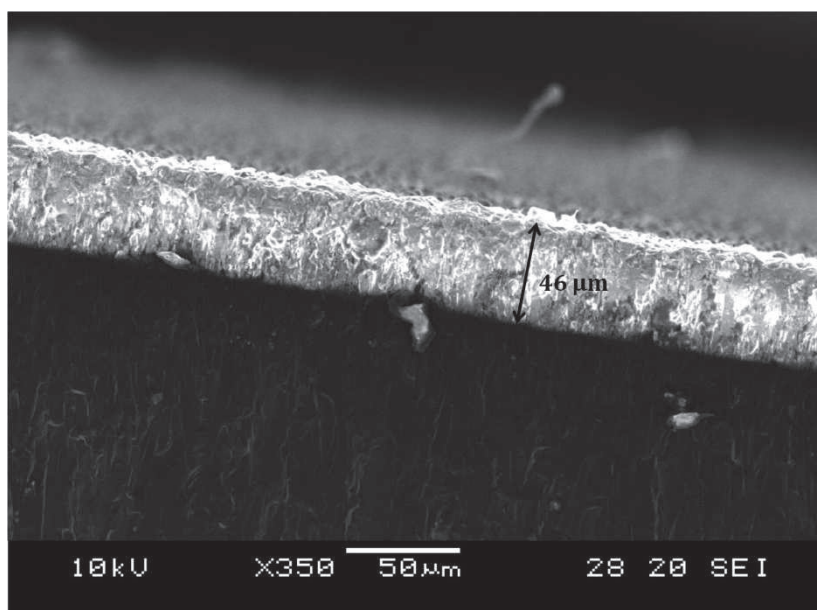
Figure 2.2. An SEM image of the un-doped diamond layer. The contrast of the two layers is representative of their conductance. The insulating layer initially traps electrons creating a negative space charge that reflects new electrons and causes the layer to appear white.

2.2.2   Laser Machining

A Nd:YAG laser (532 nm) micro-machining system (Alpha, Oxford Lasers) was used for several processes. Firstly, the square un-doped diamond coated samples were cut into four smaller samples (5 × 5 × 0.6 mm). Due to the thickness of the samples it was necessary to cut roughly a third of the way through before snapping the sample.

Secondly, cavities were drilled through the samples. Herein, any mentioned hole sizes refer specifically to the diameter, D. Holes were drilled through the insulating side of the device. Plasma formation occurs within the gap between anode and cathode. It was therefore important that the insulating side had a well-defined hole to ensure consistent plasma breakdown.

Larger cavities ($D > 200$ µm) were easily drilled giving well-formed holes on both the anode and cathode faces. However, smaller cavities proved more difficult. The laser exit hole consistently formed in a cross shape (Figure 2.3). The formation of deformed holes could be a consequence of beam divergence amplified by the thick sample.[144] Alternatively, if the beam were slightly misaligned to give a non-circular laser spot, Fresnel diffraction might lead to a non-circular laser spot as it passes through the aperture.[145] One method for correcting this is to drill from both sides of the sample. This has its own difficulty; once a sample has been moved on the machine's stage it is unlikely that the precisely drilled hole can be found and the laser centred exactly.
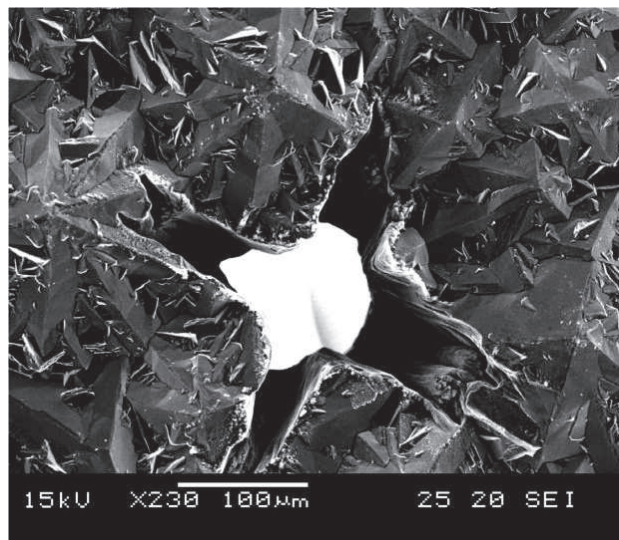

Figure 2.3. The cross shaped laser exit of a 150 µm diameter hole imaged by SEM. At smaller diameters the cross shape is more defined and transmits light poorly.

A new sample stage was designed to help centre the laser beam on the hole. A sprung mechanism in the stage ensured the sample edge was held precisely parallel to the laser x axis. The reference corner of the sample could then be found and the distances in the x and y axis retraced to find the hole location, as shown in Figure 2.4. Figure 2.5 shows a sample subjected to this method. Initially the deformed hole is unable to let light through, but, after a second pass with the laser, a cylindrical hole is visible and capable of transmitting light.
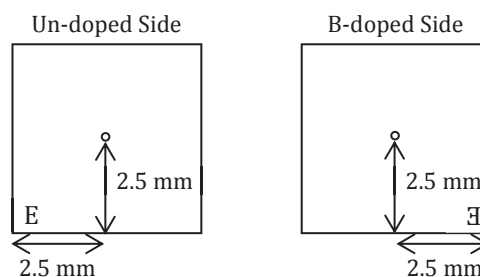
Figure 2.4. After the initial hole was drilled in the un-doped diamond face, the samples were turned over, as shown, to drill at the exact same spot on the B-doped face. The sample stage ensured samples were held parallel to the laser x axis.
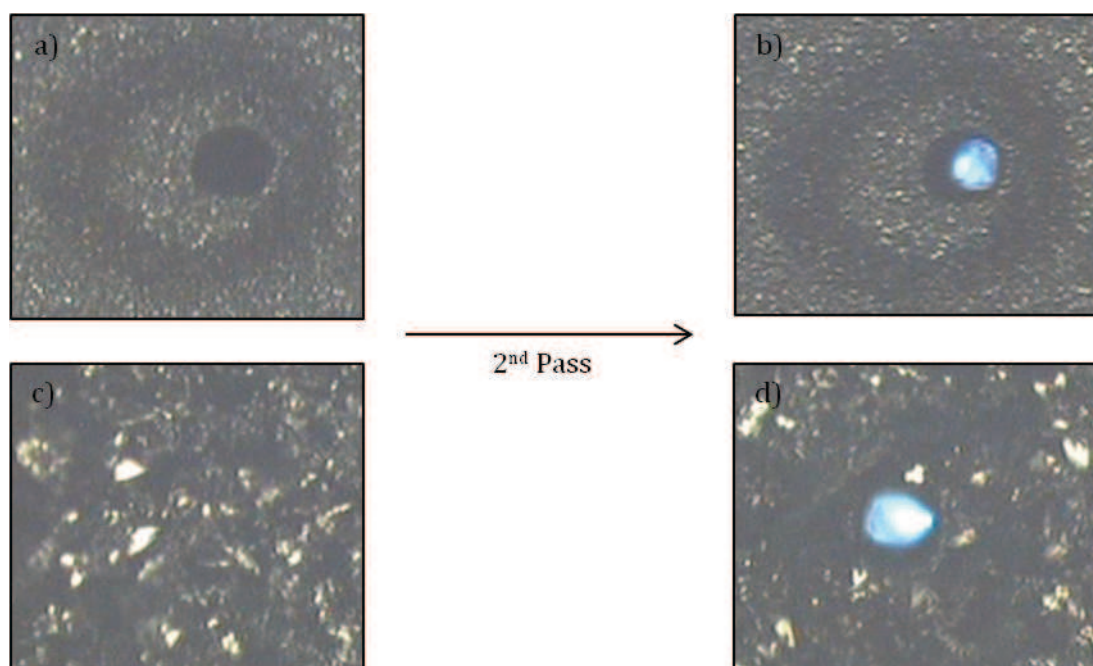
Figure 2.5. A 50 μm hole viewed at ×10 magnification both before (a, b) and after (b, d) the second laser pass. Both un-doped (a,b) and B-doped (c, d) faces are shown.

A further use was to label the samples. Short burst pulses were used to drill holes on the conducting side in a specific pattern. For simplicity, labels followed a braille numbering system where only spots were required (e.g. for E3 ∴ ⋯).

2.2.3   Acid Washing

As a result of intense thermal exposure causing a phase transition, a thin layer of conductive graphite forms on diamond surfaces exposed to laser machining.[146] This layer can be removed by oxidative acid cleaning or oxidative etching.[147] Acid washing was the method of choice in this investigation; samples were washed in concentrated HNO_3 (16 M) at ~ 100 °C for *ca.* 2 hours. Resistance measurements indicated this was enough to remove the graphite layer.

Samples showing degradation or sputtering after operation were again acid washed in a solution of concentrated HNO_3 (16 M) at ~ 100 °C for *ca.* 2 hours. Inspection of washed samples under magnification showed that most of the sputtered material had been removed.

2.2.4   Device Types

All fabricated devices followed the geometry described in Section 2.1. However, the size, number and geometry of holes were varied. Hole diameters ranged from 40 – 600 μm, arrays of up to 9 holes were produced and two devices with a slit rather than a hole were tested. A catalogue of working devices is shown in Appendix II.

2.3 Sample Holder Design

The initial sandwich-type device relied on gold plated pins gently placed against the electrodes to form a circuit. Positioning of the pins was irregular and prior to measuring it was uncertain whether there was enough contact between the pin tip and the diamond. Arcs were regular and the procedure of changing samples was difficult and variable.

To overcome this, a new sample holder which ensured consistent contact between the circuit and sample was designed. Macor, a machinable and well insulating ceramic, was used to construct the insulating parts of the holder. Copper was used for most of the electrically conductive components. One exception was the molybdenum anode, which was chosen to be an intrinsic part of the device holder. The final design is shown in Figure 2.6. The holder consisted of two parts: the base which included a molybdenum cylinder insulated with macor and fitted into a thick copper disk to ensure good connectivity to the circuit, and the copper lid which fixed the sample in place and connected the cathode to the circuit.
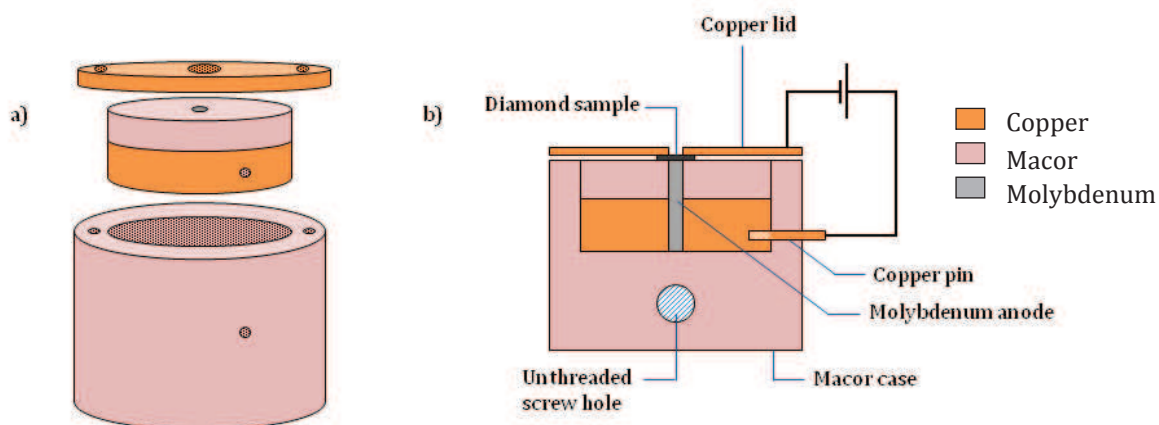
Figure 2.6. The sample holder design, shown using an isometric projection (a) and cross section (b).

The holder operated well. Initially it was difficult to align the samples and ensure the hole was positioned in the centre of the molybdenum anode so a thin PTFE template was produced to aid sample positioning. Photographs showing operation of the sample holder are shown in Figure 2.7.
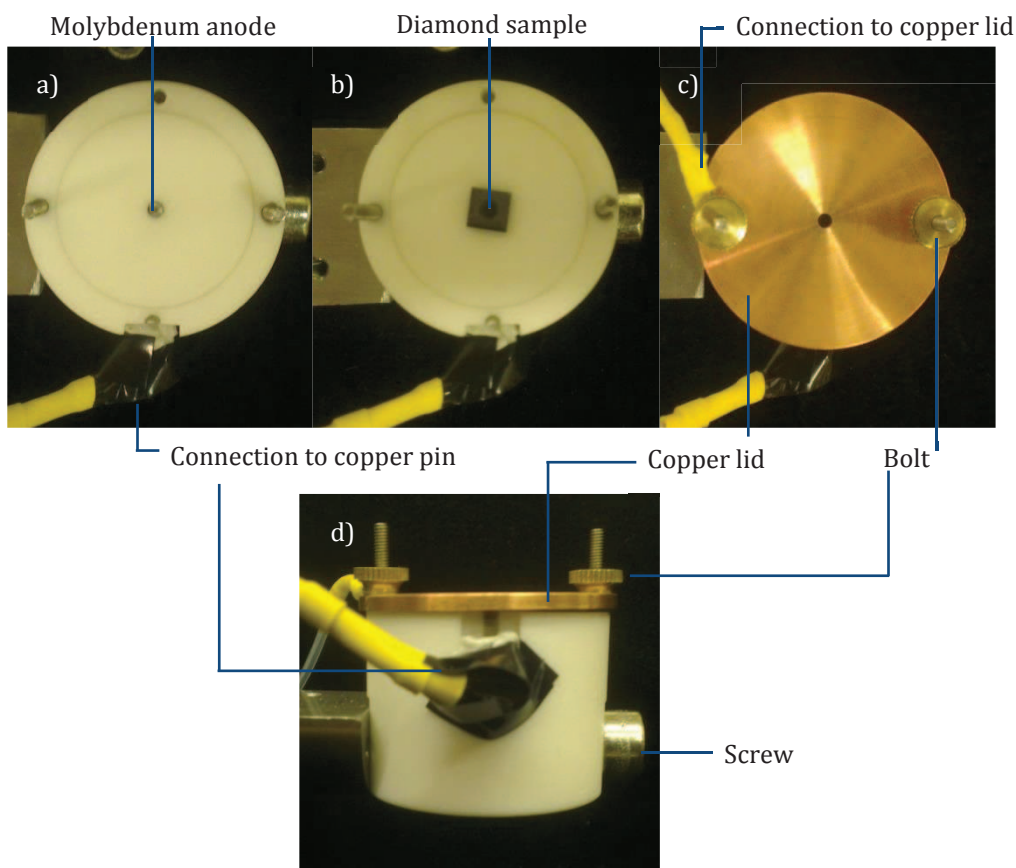
Figure 2.7. The sample holder shown from above: (a) with the anode exposed (b) with the sample in position and (c) with the copper lid in place and cathode connected. A side view of the holder with lid attached is also shown (d).
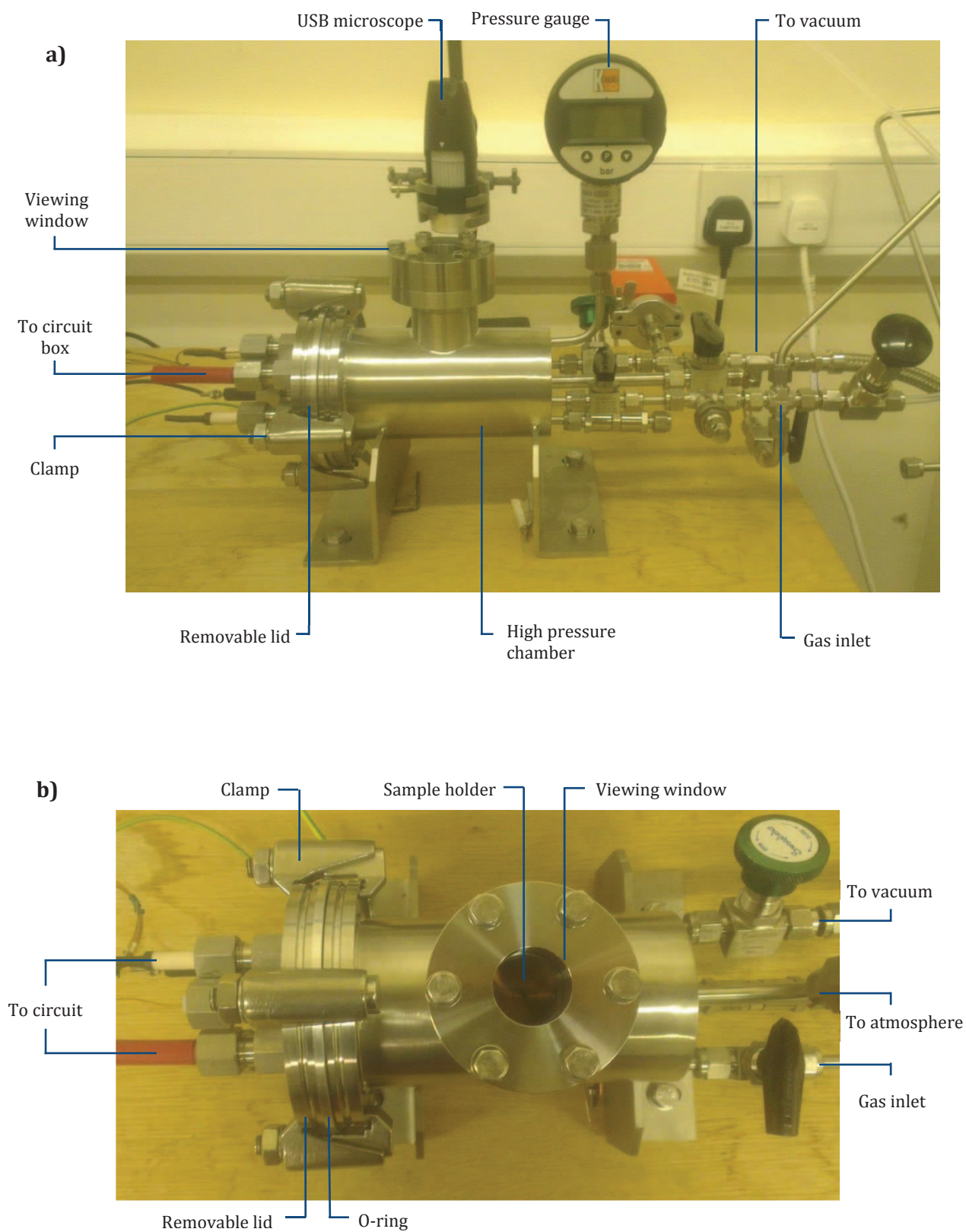
2.4 High Pressure Chamber

Samples were tested in a stainless steel chamber (Figures 2.8 and 2.9), capable of withstanding pressures of 9.5 atm. Connected to this chamber was an inlet for the required gases and an outlet leading to a vacuum pump. A quartz viewing window was situated over the sample holder. One side of the chamber was removable and attached to the sample holder with a steel bar.
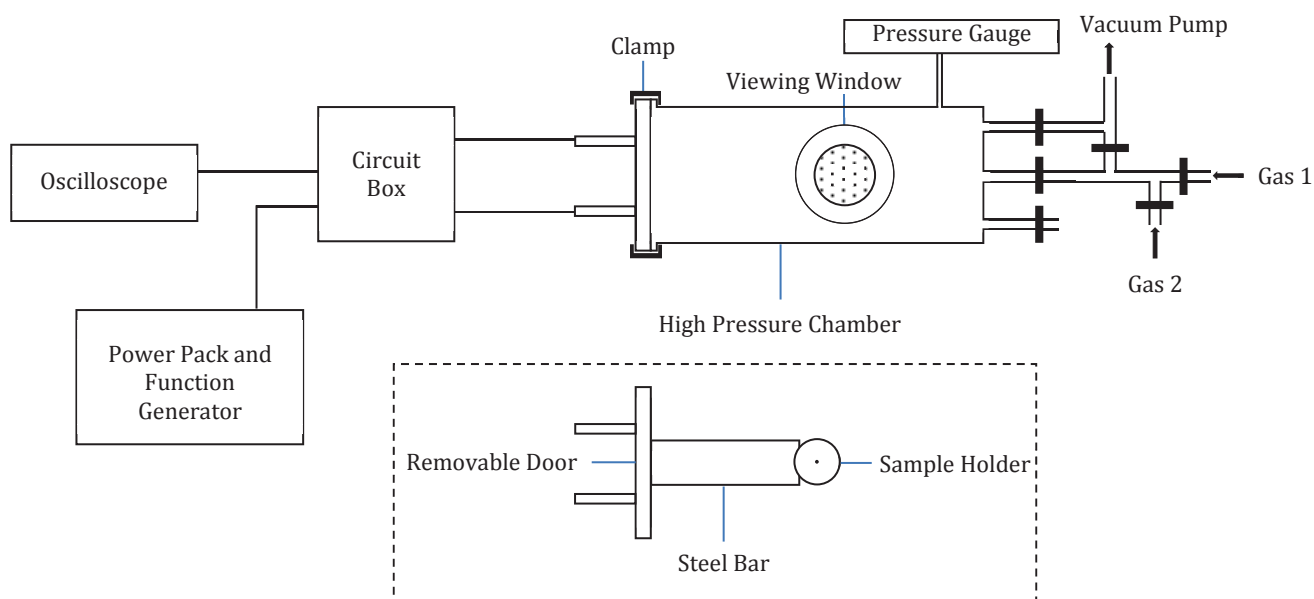
Figure 2.8. High pressure chamber and gas inlet set up.

Figure 2.9. Photographs of the high pressure chamber from the side view (a) and plan view (b).

Connected to the chamber was a piezo-resistive gauge pressure sensor (Man-SD3S, Kobold), capable of determining the chamber pressure to ± 0.5 %.

To reach the required conditions for sample operation the following steps were followed:

1. The sample holder, still attached to the chamber door, was removed.
2. A sample was carefully positioned in the centre of the holder, the lid tightened and then placed within the chamber.
3. The door was clamped and the chamber purged three times with the required gas before once again being reduced to vacuum.
4. The required amount and combination of gases were then released into the chamber.
5. The power supply was switched on.

2.5   Gases

For reasons explained in Section 1.9, helium was chosen as the operating gas. Samples operated for ~ 1 hr occasionally stopped operating at lower currents or shorted completely, evidence that graphitisation was occurring on the insulating layer. To erode the graphite formed, a small amount of H_2 in N_2 (~ 2 %) was added to the helium with the knowledge that hydrogen plasma is an effective destroyer of graphite.[148] Possibly due to the small amount of hydrogen added, graphitisation still occurred. To overcome this, regular acid washing in HNO_3 at *ca.* 100°C for 2 hrs was used to remove the built up graphite.

2.6   Circuitry

The final circuitry design is shown in Figure 2.10. Two source probes were used to measure both current and voltage directly, enabling accurate, high resolution, current measurements to be made. The power supply (BOP 1000M, Kepco) was capable of operating in both voltage and current driven mode. The function generator (TG20, Aim and Thurlby Thandar Instruments) was capable of generating sine, triangular and square waveforms with a frequency range of 0 – 1000 Hz.
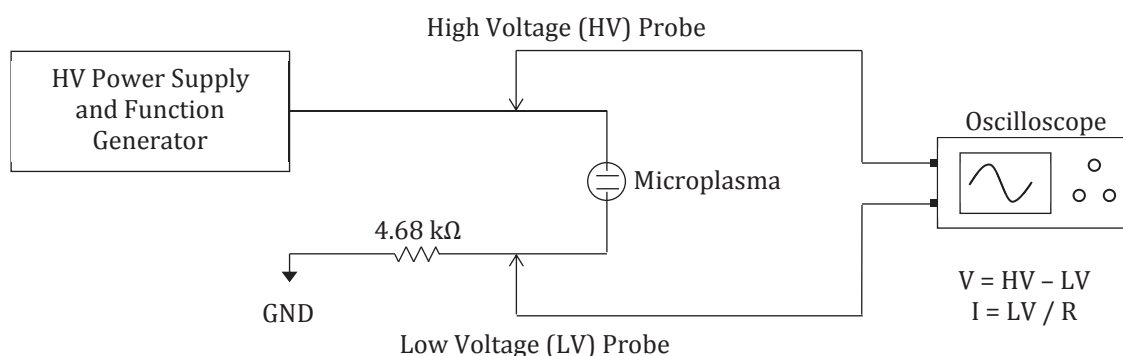
Figure 2.10. Final circuit used for microplasma operation.

The voltage was calculated using the difference between the high voltage probe and the low voltage probe. The resistor connected in series is required primarily for calculating the current using Ohm's law, V = I × R, but also acts as a ballast resistor due to its high resistance of 4.68 kΩ.

This resistor limits the current flowing through the circuit, preventing damage to the sample and ensuring the power pack's current limit is not exceeded.

2.7 Current/Voltage measurements

The oscilloscope (WaveRunner 64Xi, LeCroy) displayed real-time current and voltage data in the form of voltage/current against time plots in addition to a V-I characteristic. The time period shown was adjustable. Displayed data could be saved and replotted using conventional graphing programmes to give V-I characteristics and Paschen curves.

2.7.1 V-I Characteristics

To record V-I characteristics the power supply was operated in current driven mode. A triangle waveform was generated to continuously vary the current from 0 to ~ 15 mA at a frequency of 1 Hz. Between 60 and 150 accumulations were collected to average out random events such as filament formation. Each saved dataset contained 1 million data points.

Such a large number of data points meant manipulation was processor intensive in basic graphing programmes. To solve this, a Savitzky-Golay filter using a decimation factor of 100 was applied via a Python program to smooth and reduce the number of data points to 10,000.[149] This smoothing process had little effect on characteristic shape, as shown in Figure 2.11.
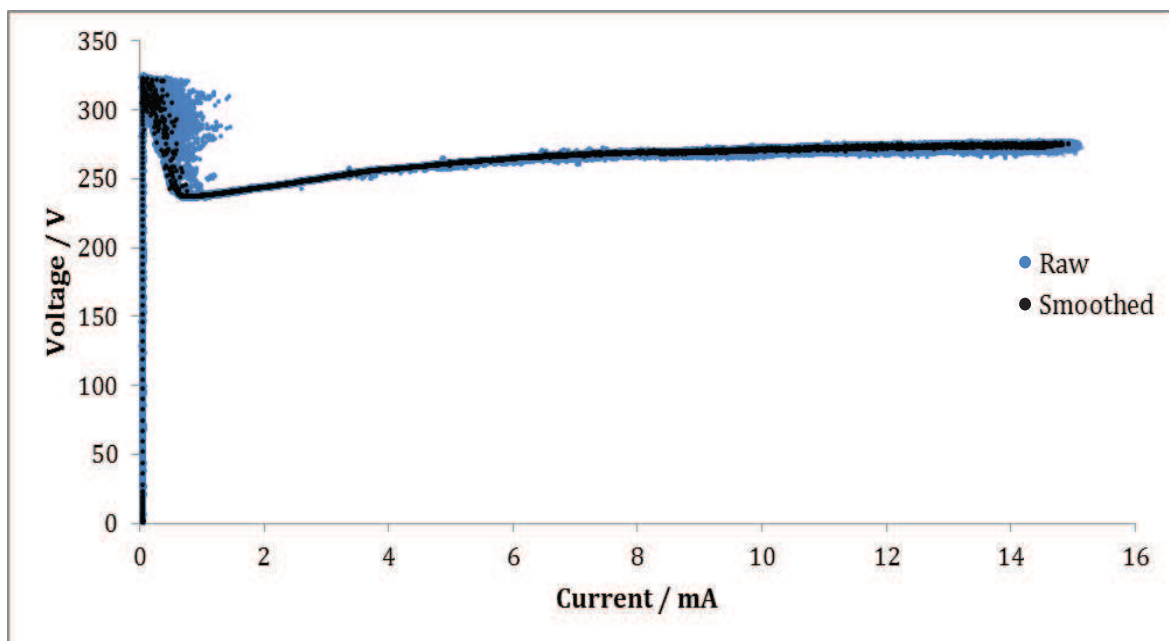

Figure 2.11. A V-I characteristic for a 200 μm device operating at 1 atm. Shown is data before (raw) and after (smoothed) application of the Savitzky-Golay filter. There is very little reduction in detail despite the hundredfold reduction in data points.

2.7.2 Paschen Curves

Breakdown voltages were measured by operating the power pack in voltage driven mode. A triangle waveform was chosen to vary the voltage from 0 to ~ 600 V at a frequency of 1 Hz. Upon reaching the breakdown voltage the current immediately increased dramatically and the voltage decreased to the sustaining voltage. The voltage against time graphs (Figure 2.12) were

analysed to find the breakdown voltages which were then plotted against $p \cdot d$. The distance between the electrodes (d), although not explicitly measured, was viewed under SEM and found to be between 40 and 60 μm. As such, $d = 50$ μm was used for the Paschen plot.
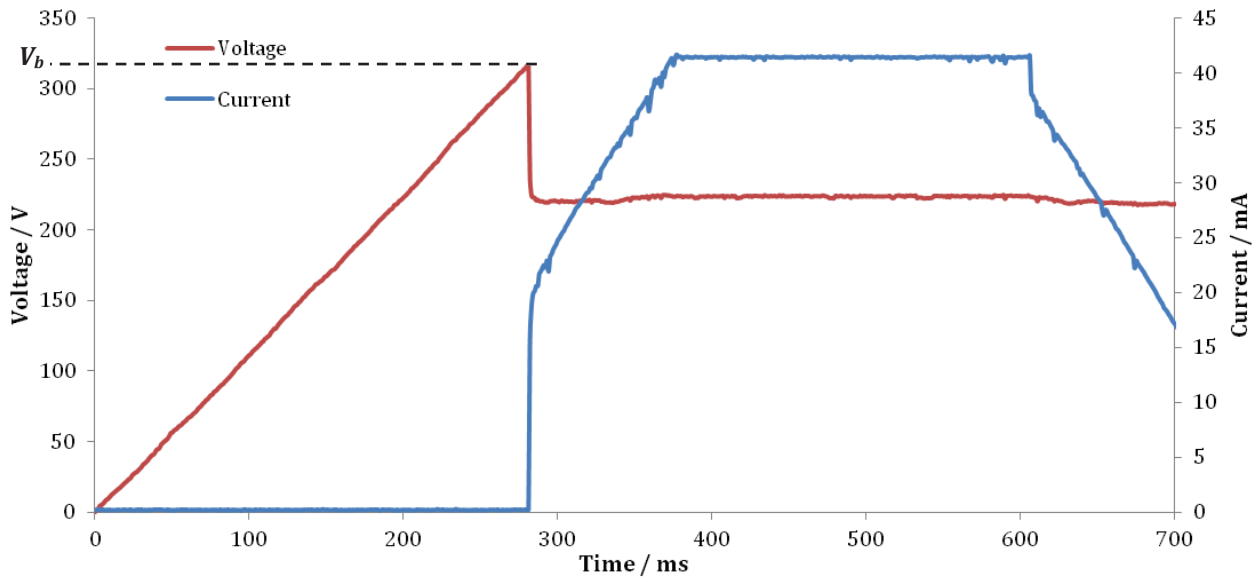
Figure 2.12. How voltage and current vary with time during a breakdown voltage measurement. V_b was determined as the voltage reached prior to the current increase.

2.8 Optical Emission Spectroscopy

OES was used to measure the excitation temperature and the gas temperature of the plasma. A Czerny Turner type optical design with a 127 mm focal length and diffraction grating of 1800 lines per mm was used. The detector (EMCCD, Andor Newton) was cooled to -50 °C. Spectra were calibrated to absolute values using a mercury pen lamp. Prior to measurement the chamber was purged ten times to ensure gas purity.

2.8.1 Excitation Temperature

Excitation temperatures were determined using the Boltzmann plot method (see Section 1.10.3) for both helium and neon lines. In the case of neon, the gas mixture consisted of a 50:50 mix of neon and helium. In both cases 512 accumulations and exposures of 0.03252 s were used. Five lines, shown in Table 2.1, were used for the helium plot.[150]

Table 2.1. The spectral lines used for the helium Boltzmann plot.[150]

Wavelength λ / nm	Configuration	Upper state energy ε_q / eV	Statistical weight g_q	Transition probability A / 10^7 s^{-1}
388.9	2s(^{3}S) - 3p(^{3}P)	23.01	9	0.95
447.2	2p(^{3}P) - 4d(^{3}D)	23.74	15	1.63
501.6	2s(^{1}S) - 3p(^{1}P)	23.09	3	1.34
587.6	2p(^{3}P) - 3d(^{3}D)	23.07	15	7.07
667.8	1p(^{1}P) - 3d(^{1}D)	23.07	5	6.37

For the neon plot, 21 lines, shown in Table 2.1, were used. All the lines originate from the $2p^53p$ → $2p^53s$ configuration as many levels in the $2p^53p$ configuration are well populated. The lines are split into four multiplets depending on the term of the lower energy level.[151]

Table 2.2. The spectral lines used for the neon Boltzmann plot. The multiplets are labelled using the respective lower energy level term.[151]

Multiplet	Wavelength λ / nm	Configuration	Upper state energy ε_q / eV	Statistical weight g_q	Transition probability A / 10^7 s^{-1}
$2p^53s$ [3/2]$_2$	640.2	$2p^5(^2P_{3/2})3s$ - $2p^5(^2P_{3/2})3p$	18.56	7	4.33
	633.4		18.58	5	1.36
	621.7		18.62	3	0.77
	614.3		18.64	5	2.16
	597.6	$2p^5(^2P_{3/2})3s$ - $2p^5(^2P_{1/2})3p$	18.70	3	0.43
	594.5		18.71	5	1.05
	588.2		18.73	3	1.28
$2p^53s$ [3/2]$_1$	650.7	$2p^5(^2P_{3/2})3s$ - $2p^5(^2P_{3/2})3p$	18.58	5	2.32
	638.3		18.62	3	2.79
	630.5		18.64	5	0.51
	607.4		18.71	1	6.17
	612.8	$2p^5(^2P_{3/2})3s$ - $2p^5(^2P_{1/2})3p$	18.70	3	0.33
	609.6		18.71	5	1.69
	603.0		18.73	3	0.63
$2p^53s$ [1/2]$_0$	653.3	$2p^5(^2P_{1/2})3s$ - $2p^5(^2P_{3/2})3p$	18.62	3	1.28
	626.6	$2p^5(^2P_{1/2})3s$ - $2p^5(^2P_{1/2})3p$	18.70	3	2.23
	616.4		18.73	3	1.60
$2p^53s$ [1/2]$_1$	692.9	$2p^5(^2P_{1/2})3s$ - $2p^5(^2P_{3/2})3p$	18.64	5	1.90
	671.7	$2p^5(^2P_{1/2})3s$ - $2p^5(^2P_{1/2})3p$	18.70	3	2.34
	667.8		18.71	5	2.38
	659.9		18.73	3	2.51

2.8.2   Gas Temperature

Prior to microplasma operation a small amount of nitrogen was bled into the system (< 1%). Spectra were collected between 0.5 and 4.0 atm. The product of accumulations, exposure and gain were kept constant at 2048 s for each measurement.

Two bands from Nitrogen's second positive system, C $^3\Pi_u$ (v=0)→ B $^3\Pi_g$ (v=2) and C $^3\Pi_u$ (v=1)→ B $^3\Pi_g$ (v=3) between 372 and 382 nm, were well resolved at a vibrational level, even at high pressures. Pgopher was used to fit a simulated spectrum against these two peaks while floating both rotational and vibrational temperatures, T_R and T_V, respectively.[152] Assuming N_2 is in thermal equilibrium with the helium atoms, T_R is equal to gas temperature. An example of the simulated and experimental spectra are shown in Figure 2.13.
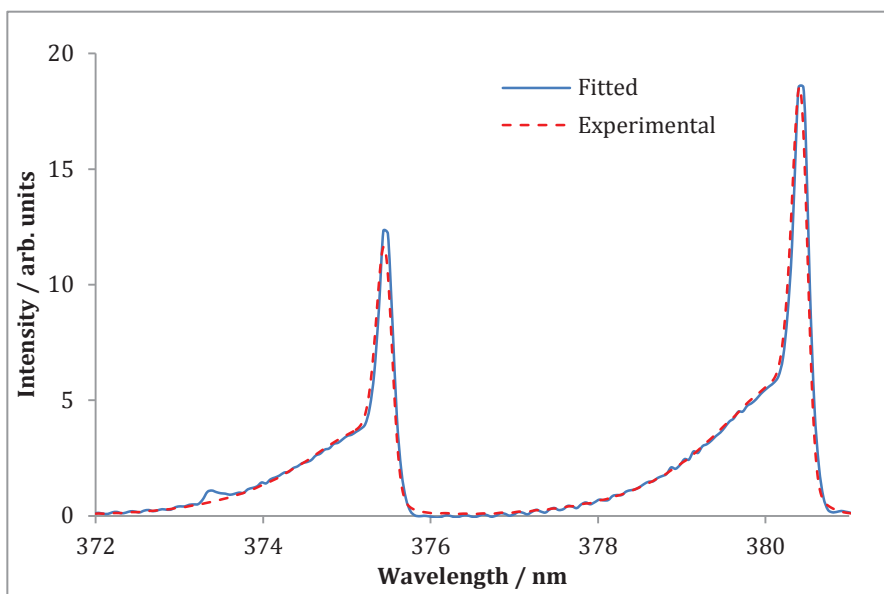
Figure 2.13. The fitted and experimental bands used to measure the gas temperature at 1 atm. The C $^3\Pi_u$ (v=0)$\rightarrow$ B $^3\Pi_g$ (v=2) and C $^3\Pi_u$ (v=1)$\rightarrow$ B $^3\Pi_g$ (v=3) peaks lie at 380.4 and 375.5 nm respectively.

2.9   Images

A USB digital microscope (Nikkai computers) was used to take pictures of the plasma during operation. Samples were also viewed using an optical microscope (Axiolab, Carl Zeiss Microscopy) and by scanning electron microscopy (SEM, JSM-5600 LV, JEOL).

3 Results and Discussion

Samples were consistently operated at pressures between 0.5 and 9.5 atmospheres. Characterisation of microplasmas at pressures greater than two atmospheres is thus far unprecedented in the literature. As such, the following section will aim to understand the physical nature behind device operation and compare it to well characterised devices operated at lower pressures. A number of underlying queries will be addressed in this section, including:

1. Is plasma formation characteristic of traditional Townsend breakdown?
2. How does the plasma change with an increase in pressure?
3. Is the plasma operating in the glow discharge mode?
4. Does the hole diameter have an effect on plasma operation?
5. Is diamond an effective material for preventing damage and prolonging device lifetime?
6. Can arrays be operated successfully under high pressures?

3.1 Plasma Breakdown

Plasma formation occurred almost exclusively within the cavity, even at high pressures. Good insulation of circuitry, combined with reliable electrical contact to the sample, ensured the breakdown voltage within the cavity was lower than elsewhere in the chamber.

Figure 3.1 shows Paschen curves obtained for three devices of varying diameters and geometries. Errors in V_b were calculated using the standard deviation with an added correction factor for the low sample size of three (the best unbiased estimator of the population standard deviation).[153]
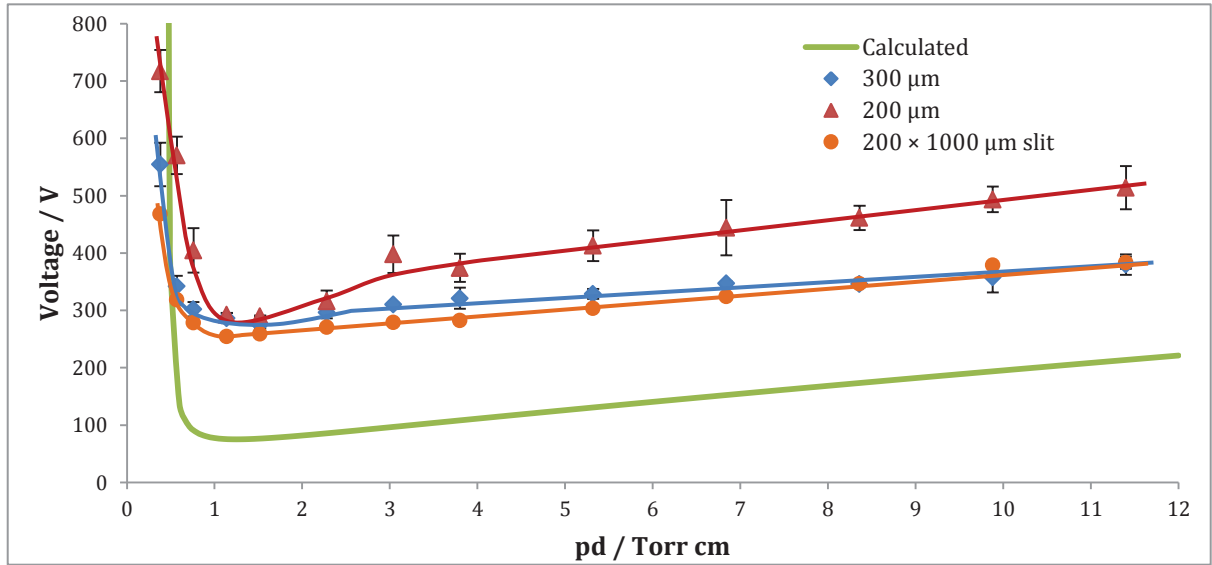
Figure 3.1. Paschen curves for several devices, two with circular apertures with diameters of 300 μm (blue diamond) and 200 μm (red triangle) and one with a 200 × 1000 μm slit (orange circle). A theoretical curve is also shown (green line), calculated using the equation and helium constants given by Burm.[156]

### 3.1.1 Validity of Breakdown Measurements

Prior to examining the curves, the validity of the measurements should be considered. Although a popular method of determining V_b in the literature, the technique of increasing voltage until breakdown occurs has been questioned. Maric *et al.* suggested that, due to the statistical nature of seed electron formation, the measured breakdown voltage may be considerably higher than the true value.[154]

Although it is true that seed electron formation is of a statistical nature, the accuracy of the measurement is dependent on the seed electron density, n_{seed}.[155] If n_{seed} is maintained above the minimum value required for breakdown during voltage increase, an accurate V_b can be determined. Generally, prior to breakdown, low currents between 10^{-10} and 10^{-5} A are observed. The currents are attributed to the presence of seed electrons, suggesting there is a constant non-zero n_{seed} between the electrodes.[69] The low error values associated with the measured breakdown voltages suggest n_{seed} in the predischarge gas volume is high enough for accurate V_b evaluation.

3.1.2 Similarity to a Townsend Discharge

The most obvious feature of all three paschen curves is their similarity in shape to the theoretical curve calculated for a Townsend discharge. At roughly 0.3 atm ($p{\cdot}d$ = 1.1 Torr cm) all three devices exhibit a minimum V_b, with a steep increase at lower $p{\cdot}d$ and more gentle increase at greater $p{\cdot}d$. The physical interpretation of this shape can be explained using the Townsend theory of plasma formation (see Section 1.2.7). The similarity in shape therefore indicates that plasma formation is as expected for a gas discharge and likely follows Townsend theory. Additionally, the minimum is consistent between the calculated and experimental curves suggesting the value of d = 50 μm is an accurate representation of electrode separation, despite the hollow cathode.

In contrast to the MHCDs, the theoretical curve is associated with a planar electrode geometry with a uniform electric field.[156] This difference will affect the breakdown voltage. One consequence is a shift to higher breakdown voltages. It is possible the curved electric field might lead to the quenching of electrons through collisions with the insulating layer or a wider distribution of electron energies, shown in Figure 3.2. In either case, a higher breakdown voltage might be required.
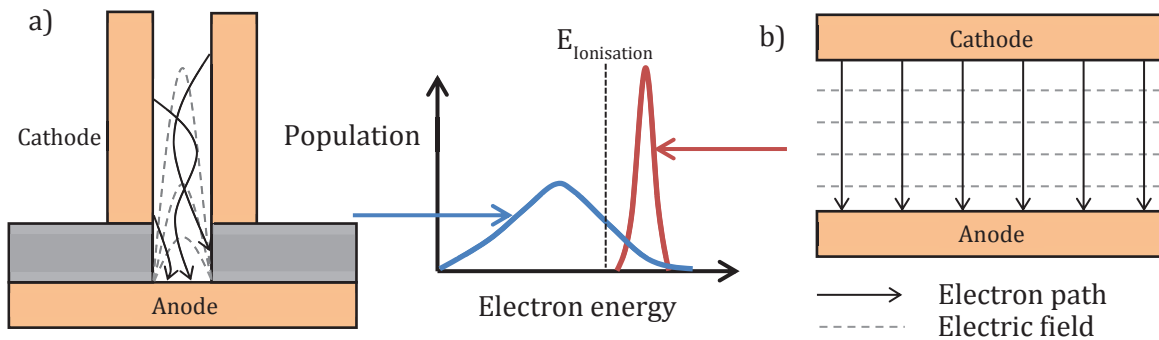
Figure 3.2. A non-uniform field and long cathode (a) would lead to a wider distribution of electron energies. This might mean for a specific voltage too few electrons have enough energy to ionise the gas compared to a planar electrode geometry (b), meaning a higher breakdown voltage is required.

A further consequence is the less sharp increase in V_b at low $p \cdot d$. Long path breakdown, where electrons are accelerated from within the cathode cavity can explain this. At low pressures, where the mean free path is too long for substantial collisions to occur, the discharge operates at longer paths from a point within the cavity.[154] Essentially, the electrode separation, d can be thought of as a more flexible value, especially at low $p \cdot d$.

The curves compare well with those for other MHCDs. Both Gomes *et al.* and Sismanoglu & Amorim characterised sandwich type devices under argon and observed similar curves with higher breakdown voltages and shallower slopes at low $p \cdot d$ when comparison with theoretical curves.[69, 71]

3.1.3 Effect of Cavity Shape

All three devices exhibited similar curves. However, differences are noticeable and are most likely a consequence of differing cavity size. Generally, the larger the cavity, the lower and more shallow the Paschen curve. This is most obvious when comparing the devices with 300 and 200 µm diameter holes. One interpretation might follow the idea of electron quenching used to explain the higher V_b of non-planar electrodes. Electrons confined to smaller cavities have less access to the anode surface, resulting in a greater proportion being quenched through collisions with cavity walls.

Smaller apertures were more difficult to drill (see Section 2.2.2) and often formed imperfect cavities. Moreover, protrusions formed on the cavity surfaces throughout operation. It is possible these protrusions might enhance the local electric field during breakdown and affect the breakdown voltage. The surface area within the cavity determines how prevalent surface effects are. As such, one would predict protrusions and imperfections would have a greater effect on plasma operation for devices with smaller apertures and a smaller internal surface area. This is reflected in the error magnitude. The 200 µm device had far larger errors and breakdown voltages were more inconsistent, possibly a consequence of breakdown at different protrusions each time.

Contrary to preceding discussion, Sismanoglu & Amorim and Schwaederlé *et al.* both compared the Paschen curves of devices with circular apertures of different sizes and found diameter to have no influence on breakdown.[69, 118] It is possible this is also the case in these devices, with dissimilarities in the Paschen curves arising purely from different cavity morphologies unrelated to aperture size. A greater number of devices would need to be studied for a more definite conclusion.

3.2 Modes of Operation

Regardless of operating pressure, a general V-I characteristic was observed for all device types, shown in Figure 3.3. This characteristic can be separated into three different modes. At very low currents a steep increase in voltage is observed. This is the predischarge mode in which plasma breakdown has not yet occurred.
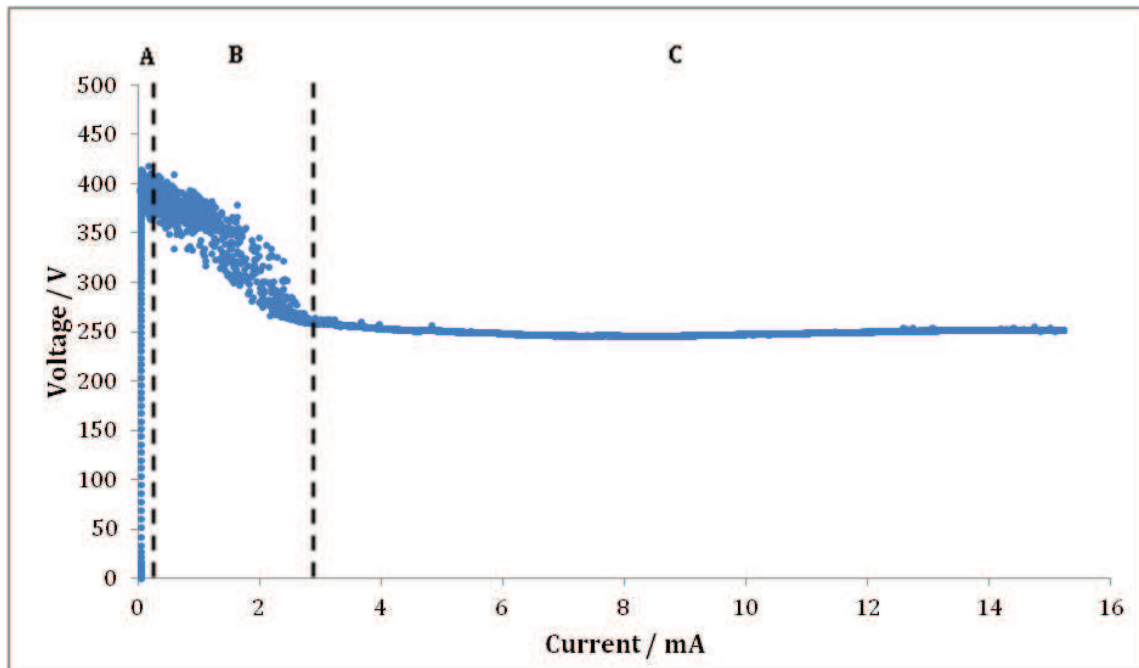
Figure 3.3. The V-I characteristic for a 200 µm diameter device operating at 5 atm. Three distinct regimes are visible: predischarge mode (A), self-pulsing mode (B) and normal mode (C). This general shape was observed in all devices between 0.5 and 9.5 atm.

3.2.1   The Self-Pulsing Mode

Following breakdown, the plasma enters a new regime spanning between 1 and 3 mA. Although a negative differential is observed, with voltage decreasing with current, the voltage-current relationship within this regime is poorly defined, despite averaging over 60 accumulated plots. Similar negative differential regimes following the predischarge mode have been exhibited by comparable MHCDs. Generally this mode is interpreted in two ways: either as the Hollow Cathode mode or as the self-pulsing mode.[60, 66]

Described in Section 1.4.1, the Hollow Cathode mode features pendulum electrons ionising a large number of gas molecules and producing increased light emittance. However, in order for this mode to occur, the plasma must conform to the White-Allis similarity law, in which $pD < 1.1$ Torr cm.[58] All devices investigated in this project were operated with $pD \gg 1.1$ Torr cm and therefore the mean free path of oscillating electrons is too short for the Hollow Cathode mode to occur.

The self-pulsing mode, explored in Section 1.4.2, has been used to describe V-I characteristics of microplasmas operated at pressures with pD > 1.1 Torr cm. This regime features oscillations of both current and voltage.[66]

In addition to flat waveforms where both current and voltage were maintained, oscillating waveforms, shown in Figure 3.4, were observed when the current was set to a value representative of the negative differential regime (0.1 – 2 mA). The waveforms are almost identical to those observed by Aubert *et al.*, Hsu & Graves and Lazzaroni & Chabert (Figure 1.10), suggesting the regime is the self-pulsing mode.[64, 66, 68] They feature a steady increase in sustaining voltage from roughly 270 to 440 V. Upon reaching 440 V the voltage drops sharply to 270 V, associated with a strong current pulse reaching 16 mA then decreasing to roughly 50 µA.

40
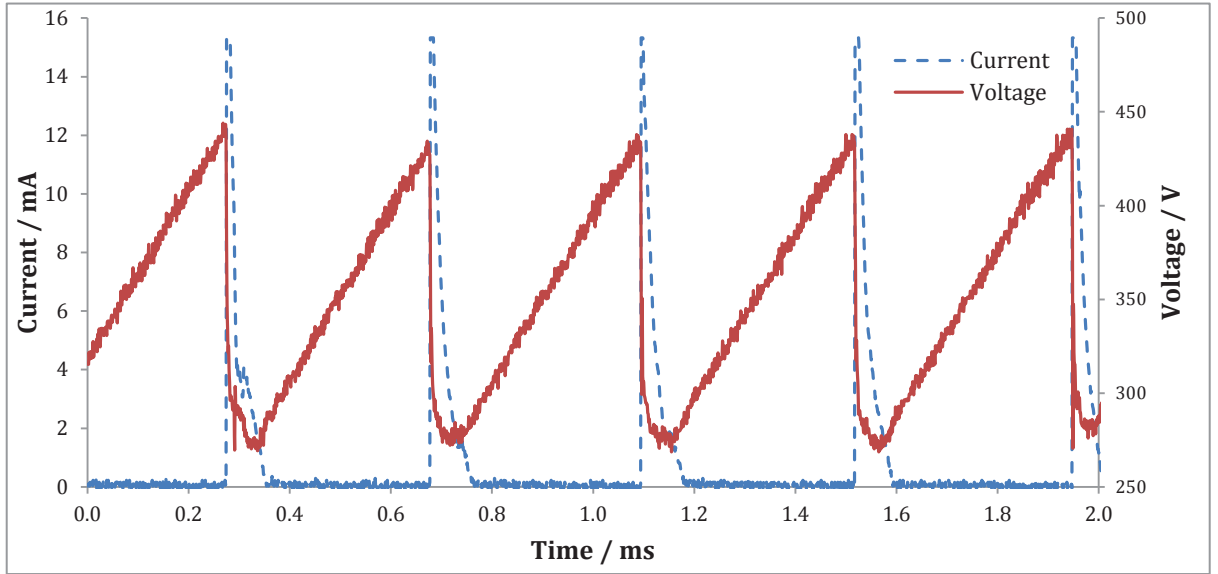
Figure 3.4. Time evolutions of both current and voltage observed at an average current of 1.0 mA for a 200 μm device operating at 5.0 atm.

Furthermore, the oscillation frequency increased along with the driven current specified. Figure 3.5 shows three voltage waveforms observed at different driven currents. Frequencies in the literature tended to range from tens of kHz to MHz.[64] The frequencies observed in this work are between 2 and 10 kHz. The discrepancy is most likely due to the much higher operating pressure. Further investigation would be necessary to determine this.

Aubert *et al.* found frequency increased with average current.[66] In contrast, the average current for the oscillations presented here tended to remain constant at roughly 1 mA. Instead the defining current was the current maintained during short periods of stable operation between oscillations. The reliance of frequency on specified driven current may be an indication that the oscillations are not indicative of the self-pulsing mode and are instead a consequence of power supply operation in current driven mode.
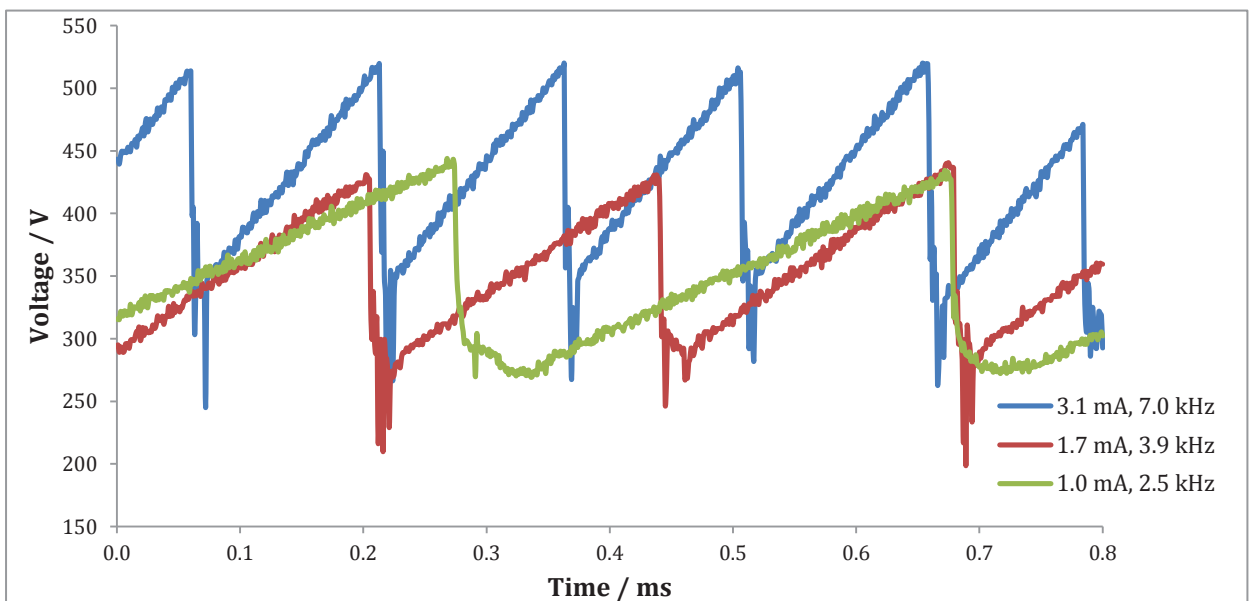
Figure 3.5. Time evolutions of voltage observed at different specified driven currents for a 200 μm device operating at 5.0 atm.

More conclusive evidence that the observed mode is indeed the self-pulsing regime would require high resolution, short exposure images or sensitive photodiode measurements of the discharge intensity during oscillations. Through these techniques the swelling and contraction cycles of the plasma, characteristic of the self-pulsing mode, could be determined. Regardless, herein the mode will be referred to as self-pulsing.

3.2.2   The Normal Mode

Following the self-pulsing mode the discharge enters a stable regime featuring very little variation in sustaining voltage with current increase. Many MHCDs in the literature exhibit this flat regime immediately following a mode of negative differential resistance, including those operated at pressures exceeding 1 atm.[58, 69]

The constant sustaining voltage can be explained physically by the expansion of the plasma over the surface of the cathode with increasing current. The increasing volume of the plasma ensures the current density remains constant and thereby the voltage required to sustain the discharge is also maintained. In agreement with this theory, the microplasmas were observed to spread over the cathode surface with current, as shown in Figure 3.6.
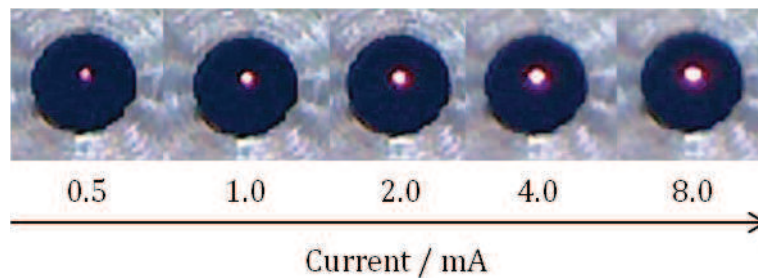
Figure 3.6. Images of a 100 μm device operating under 1.0 atm over a range of currents. The plasma clearly increases in size, spreading over the cathode surface.

Existence of the normal mode is a clear indication that even at 9.5 atm the devices are operating as glow discharges. If, instead, the discharges were arcs, a much lower sustaining voltage would be observed as well as a steep drop in voltage with current characteristic of the glow-to-arc transition.[157, 158]

3.3   Changes in Plasma Properties with Pressure

A prominent characteristic of the plasmas is the decrease in discharge size with pressure, shown in Figure 3.7. At higher pressures the plasma becomes more confined to the cavity. This is in agreement with spectroscopic measurements conducted by Lazzaroni *et al.* and fluid simulations performed by Feng *et al.* Both observed a contraction of the plasma sheath and an increase in electron density with pressure for MHCDs.[159, 160]

Fundamentally, the plasma contraction is a result of the reduction of the electron mean free path at higher pressures. The shorter mean free path means the electrons are unable to travel as far from the cathode before being quenched by collisions with helium atoms.
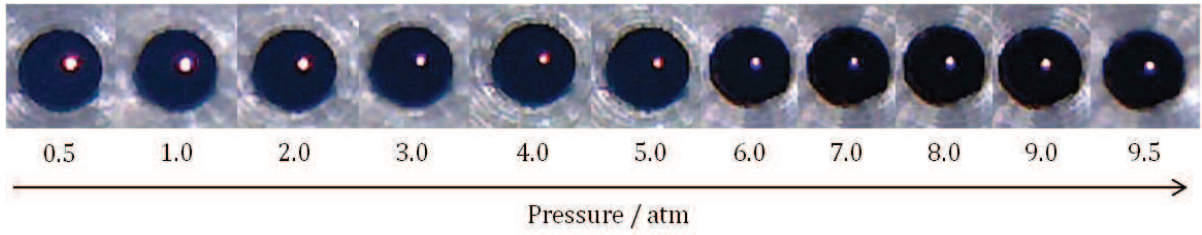
Figure 3.7. Images of a 100 μm device operating under a range of pressures with a current of 7 mA, within the normal mode of operation. The plasma contracts as pressure increases.

In addition to visual changes in the plasma upon pressure increase, closer inspection of the normal regime shows slight variance in the V-I characteristics. Figure 3.8 shows a summary of these differences for a 200 μm device, displayed as both real data and simplified illustrations. Four different characteristics were identified: low pressure (<1 atm), atmospheric pressure (1 atm), high pressure (2 – 4 atm) and very high pressure (>5 atm).
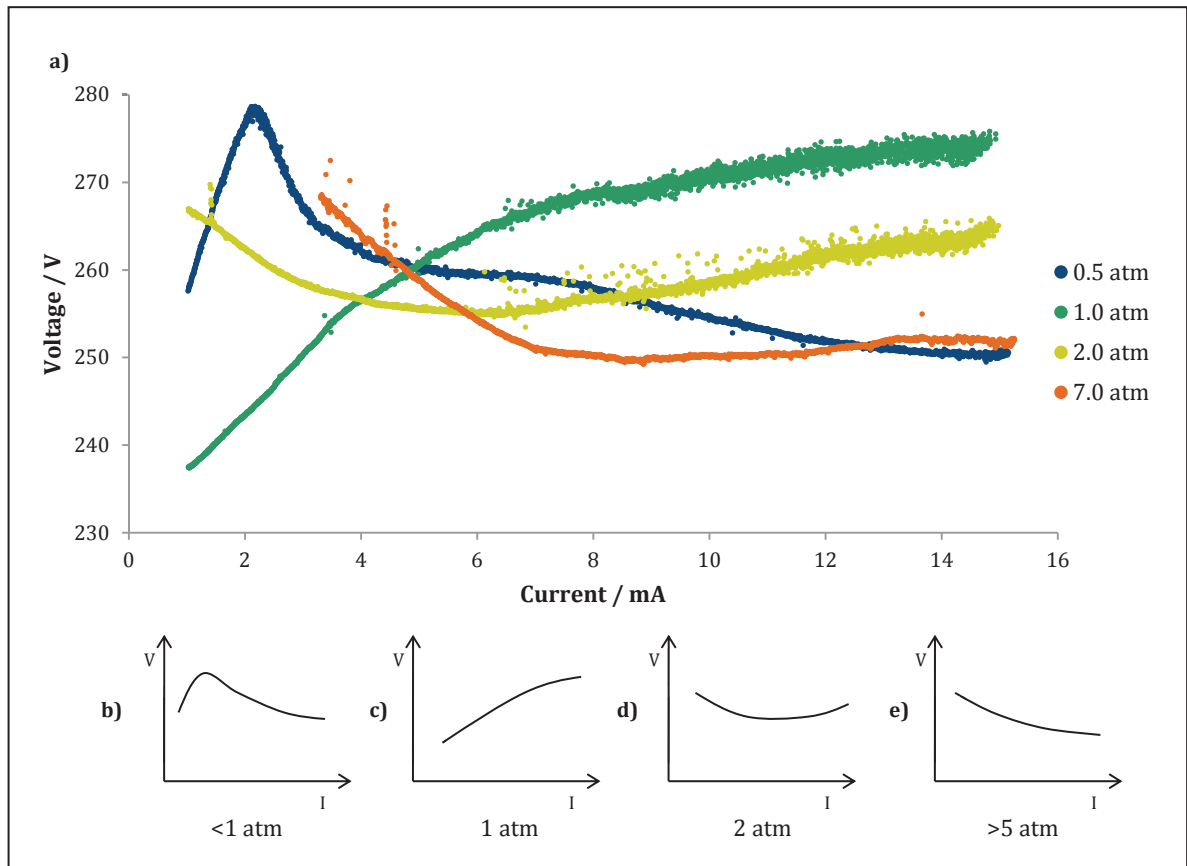
Figure 3.8. V-I characteristics of the stable normal mode for a 200 μm device operated at four pressures (a). Each pressure is representative of a different type of characteristic: 0.5 atm, low pressure (b); 1.0 atm, atmospheric pressure (c); 2.0 atm, high pressure (d); 7.0 atm, very high pressure (e).

3.3.1   Low Pressure Operation

When operated under low pressures the normal mode was less flat, featuring an initial rise of voltage with current between 1 and 2 mA (Figure 3.8b). At lower pressures the discharge is less compact and spreads over the cathode, see Figure 3.9. In comparison to higher pressure operation, the cathode surface area is more saturated. Consequently, the current density is not

held constant and a small rise in sustaining voltage is observed with current. Regions in V-I characteristics where this occurs are usually known as abnormal glow regimes.[58, 118] However, as the plasma is still observed to spread across the cathode surface, the regime might be better described as a transition between the normal and abnormal modes. As such, the regime will be referred to as pseudo-abnormal.
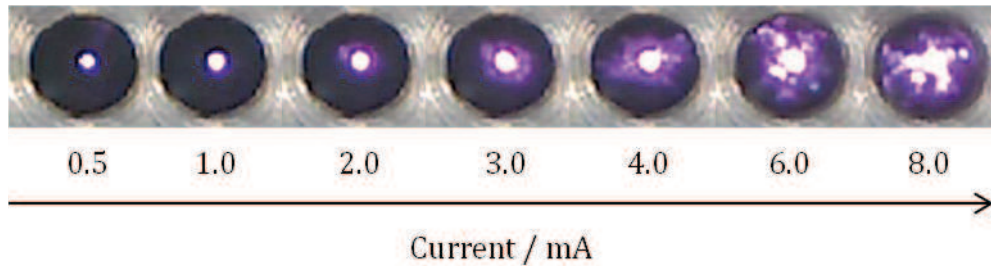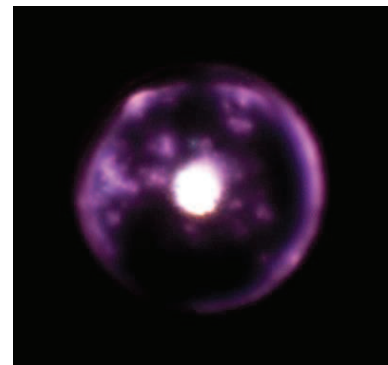

Figure 3.9. Images of a 200 μm device operating under 0.5 atm over a range of currents. Streamers appear above 2 mA.

At 2 mA a negative differential resistance is observed. This coincides with the appearance of streamers stretching from the plasma aperture to the copper lid of the sample holder, shown in Figures 3.9 and 3.10. Once the plasma interacts with or even spreads onto the copper it is difficult to justify whether the characteristic is truly representative of the device or a consequence of the copper lid. The negative differential resistance might be a consequence of the streamers bypassing the plasma sheath and producing channels of lower resistance.

Figure 3.10. Image of a 300 μm device operated at 5 mA under 0.3 atm. Streamers reach from the discharge centre to the copper lid.

Similar V-I characteristics were observed by Pekarek when studying the filamentary streamer regime for a corona discharge surrounded by a brass ring.[161]

The direction in which these streamers flow and exactly where they form is unclear. It is possible that photoinisation of the copper occurs, stimulated by UV radiation from the plasma bulk, and electrons are released from the copper lid. These electrons propagate towards the virtual anode within the centre of the cavity, causing erratic streamers. Exposing the copper to a high energy UV lamp and observing the extent of streamer activity would determine whether this is a viable explanation.

Although their formation is most likely a consequence of the copper, streamers or filaments within discharges are not unknown in similar devices. Schoenbach *et al.* observed the formation of 'streamer-like discharges' that coincided with a change in the slope of the V-I characteristic.[58]

### 3.3.2 Atmospheric Pressure and Beyond

Under atmospheric pressure the V-I characteristic is fairly simple, with a positive gradient maintained between 1 and 15 mA (Figure 3.8c). Once again this can be attributed to pseudo-abnormal operation where the more diffuse plasma occupies a large area of the cathode. Consequently, the plasma is unable to spread across the cathode as easily and current density increases. The positive differential has a lower gradient than at low pressures; the more compact plasma requires a higher current to saturate the surface.

At high pressures the positive differential, pseudo-abnormal mode is maintained above 6 mA. At low currents a stable, negative differential is observed (Figure 3.8d). Fundamentally, the appearance of this region might be explained by analysing the electron mean free path, explained in Figure 3.11.
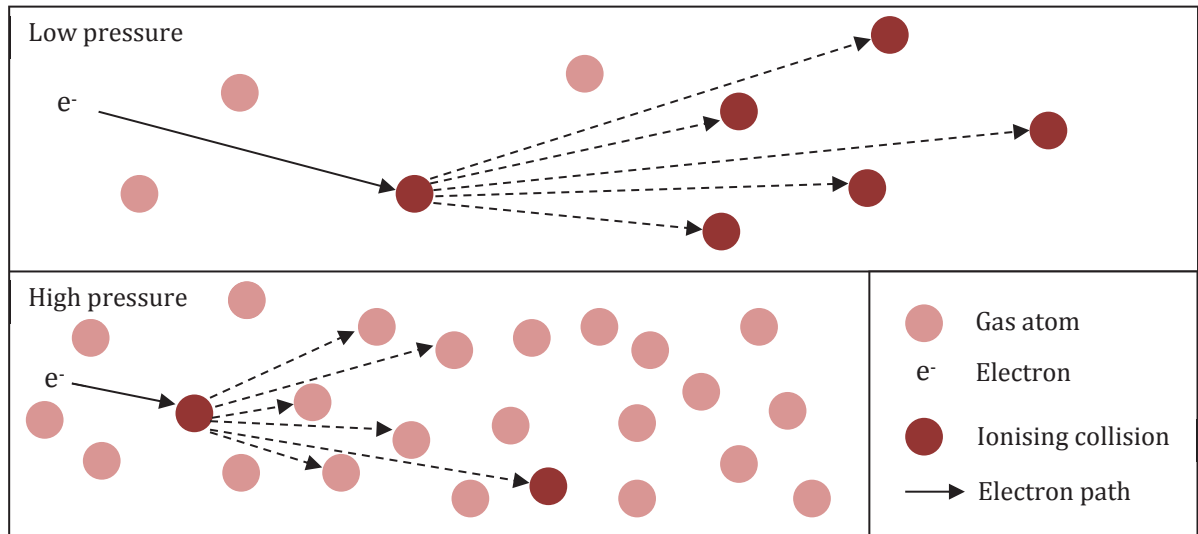
Figure 3.11. At low pressures fewer collisions ensure a longer mean free path and a higher number of ionising collisions. At high pressure fewer ionising collisions occur and to compensate the electric field needs to be stronger to maintain the same number of ionising collisions.

At low pressures, the mean free path is large and electrons regularly gain enough energy from the electric field to sustain the plasma. At higher pressures, more collisions occur and the mean free path decreases; fewer electrons gain enough energy in their mean free path to cause ionising collisions. As current is decreased, fewer electrons are expelled from the cathode. A threshold current is reached where below this value there are too few ionising collisions to sustain the plasma. Upon reaching this value, any further reductions in current will need to be accompanied by an increase in voltage to ensure the electrons have a greater amount of energy to counteract the lower density and therefore maintain the same number of ionising collisions.
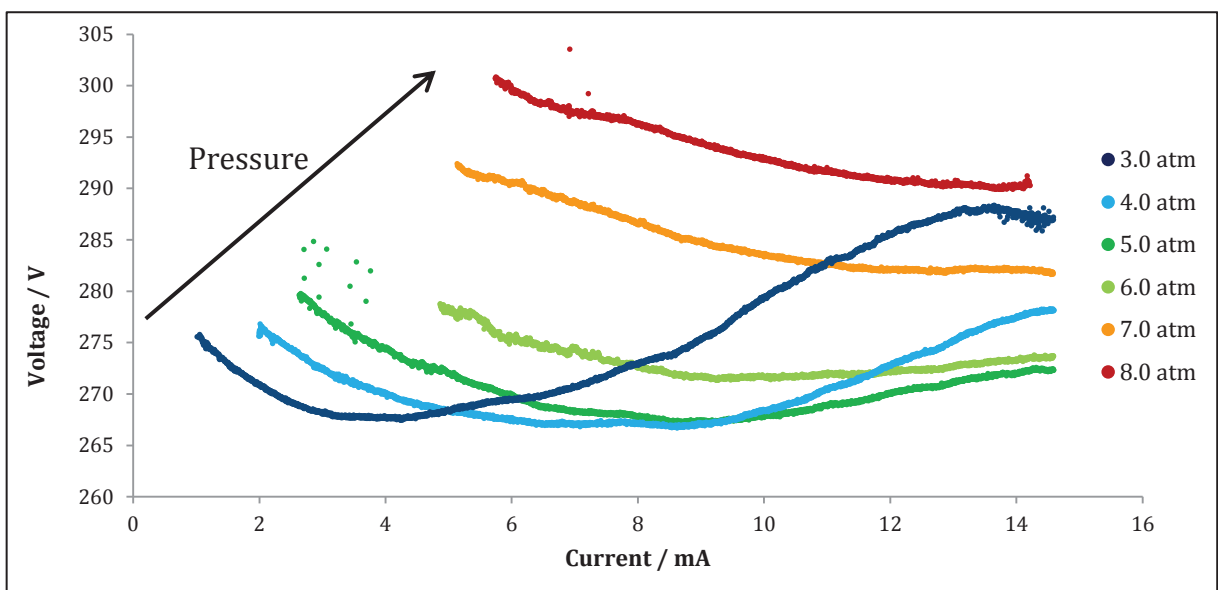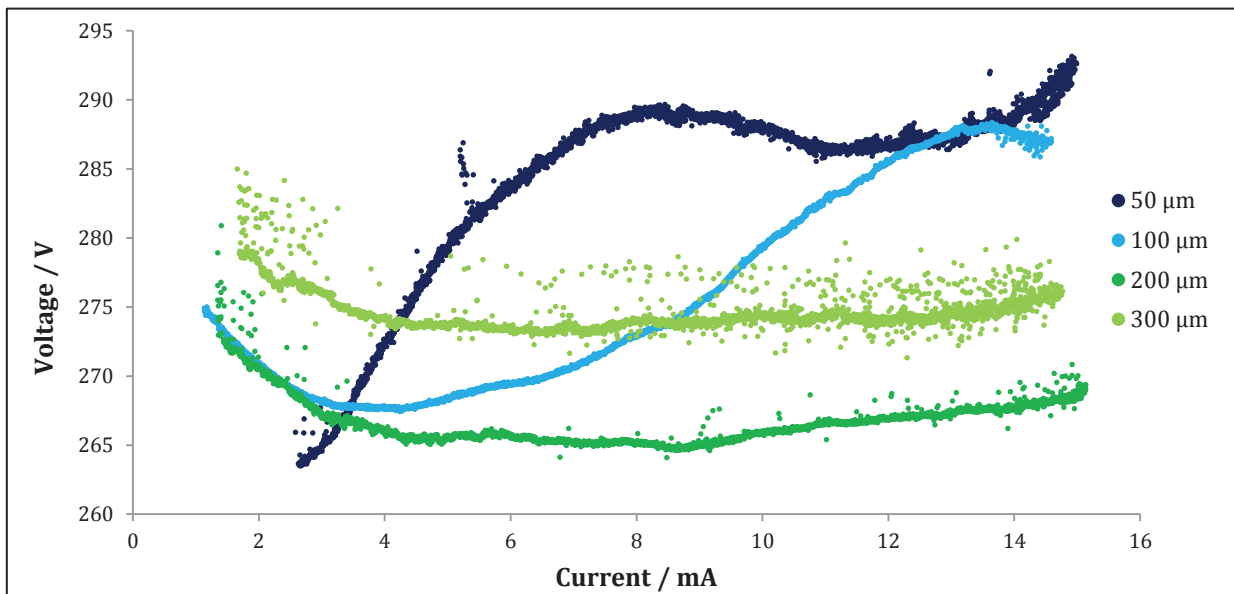

Figure 3.12. The V-I characteristics of the normal mode for a 100 μm device operated between 3 – 8 atm. A steady increase in sustaining voltage with pressure is observed in addition to a gradual reduction in the pseudo-abnormal regime.

As would be expected, with an increase in pressure, the negative slope lengthens and extends to higher current. Above roughly 5 atm the pseudo-abnormal regime is no longer exhibited within the measured current range (Figure 3.8e). A further consequence is the rise in sustaining voltage with pressure, as shown in Figure 3.12. This is in contrast to MHCDs operated at lower pressures, between 20 and 800 Torr (0.03-1.05 atm), which showed a decrease in sustaining voltage with pressure.[69, 71]

3.4 Effect of Hole Size on Mode of Operation

In Section 3.13 it was suggested that smaller apertures showed an increase in breakdown voltage on both sides of the Paschen curve (Figure 3.1). This appeared to hold true at low pressures; devices with small apertures showed poor operation. Devices with $D < 50$ μm failed to operate below 0.7 atm, instead arcs formed elsewhere in the chamber.

However, at higher pressures smaller apertures operated more consistently than larger ones. Furthermore, the distinct characteristics shown in Figure 3.8 and discussed in Section 3.3 tended to shift to higher pressures when operating devices with smaller apertures. This is shown in Figure 3.13; the 50, 100, 200 and 300 μm holes show characteristics similar to Figure 3.8b, c, d and d, respectively.

Figure 3.13. The V-I characteristics of the normal mode for four different devices at 3.0 atm. The smaller the hole size, the more similar the characteristic to those exhibited at lower pressures in Figure 3.8 (200 μm device).

The dependency of high pressure stability on D indicates that a new scaling law, akin to the White-Allis similarity law for Hollow Cathode mode operation, might be acting in this high pressure region.[56]

3.5 Device Durability

The most prominent reason for using diamond as a microplasma material relates to its ability to mitigate damage from sputtering and withstand high gas temperatures. Consequently an

important aspect of this project is to review the damage incurred during high pressure operation.

3.5.1 Lifetime

Under harsh measuring conditions, at pressures greater than 1 atm (including 9.5 atm) and currents in excess of 10 mA, samples were operated for 30 – 60 minutes before they failed to operate as microplasmas and exhibited ohmic behaviour. This ohmic behaviour suggested the surface of the insulating layer was graphitised, forming a conductive layer between the electrodes and shorting the device. After washing in hot concentrated HNO_3 the devices operated well.

Detailed lifetime studies would be required to investigate device lifetime under optimum conditions. Initial experiments were promising - when operated under constant, low current (4 mA) and high pressures (3 atm) devices were able to function much longer (> 2 hours).

3.5.2 Damage

Visualisation of devices post-operation using SEM showed evidence of graphitisation and sputtering. Figure 3.14a shows a clear pale halo surrounding the aperture. The darker outer region is the area of the cathode surface shielded from the plasma by the copper lid. In SEM, a change in brightness is indicative of a change in electronic properties.[162] As such, the halo's paleness suggests graphitisation of the surface. The surface morphology is continuous, indicating only a shallow layer formed.
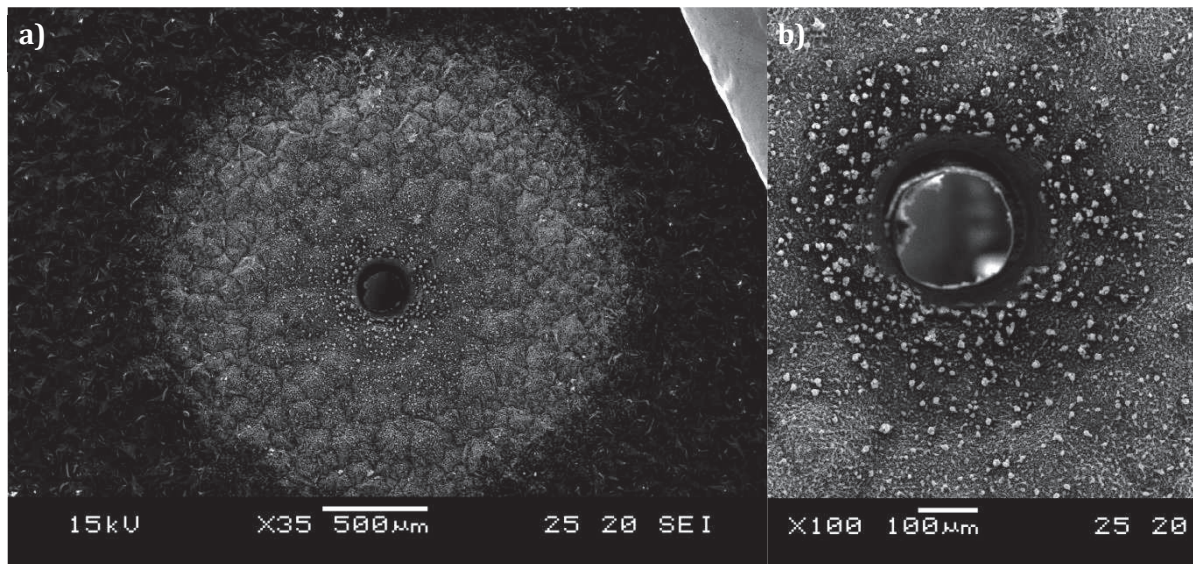
Figure 3.14. SEM images of the cathode face of a 200 μm device. Graphitisation is observed in a) whereas b) shows particulates formed by sputtering.

Upon further magnification (Figure 3.14b) small particles surrounding the hole were clearly visible. It is possible these particles are copper, sputtered onto the surface from the copper lid. Although it is understandable that the negatively charged copper would attract ions, it is less clear why the particles end up so far from their source. A further query is how the particles end up so large. Although sputtering generally proceeds via a nucleation and migration mechanism,

the particles formed are of the order of 1 μm, far smaller than observed in Figure 3.14b.[163] Further analysis is required to gain a clearer understanding, for example, the use of energy dispersive x-ray spectroscopy (EDX) in combination with SEM to identify the particle composition.[164]

Figure 3.15 shows damage within the cavity. A well-defined hollow is situated next to the insulating layer. The aperture within the un-doped diamond layer remained undamaged and 200 μm in diameter. The contrast in damage between the cathode and insulating layer indicates damage is almost entirely caused by sputtering where positive helium ions are drawn to the charged cathode surface. A further inference is the situation of the plasma during operation. In agreement with high pressure simulations the plasma is located primarily within the cathode hollow.[160] Additionally, it is possible the light debris observed on the inside of the insulating layer and cavity (Figure 3.15b) could be graphite and the cause of device shorting.

Even when operated in helium and at low pressures other DC devices show large amounts of cathode erosion from sputtering after several hours of operation.[106] In contrast, devices presented here showed little damage after hours of high pressure, high current operation, a testament to diamond's good sputter resistance and high thermal conductivity.

However, initial investigations using other gases, such as argon and neon indicated a larger amount of device damage. A possible approach to reduce damage is to operate the device at radio frequencies; if the power supply frequency is high enough the ions are immobilised and sputtering no longer occurs.[38]
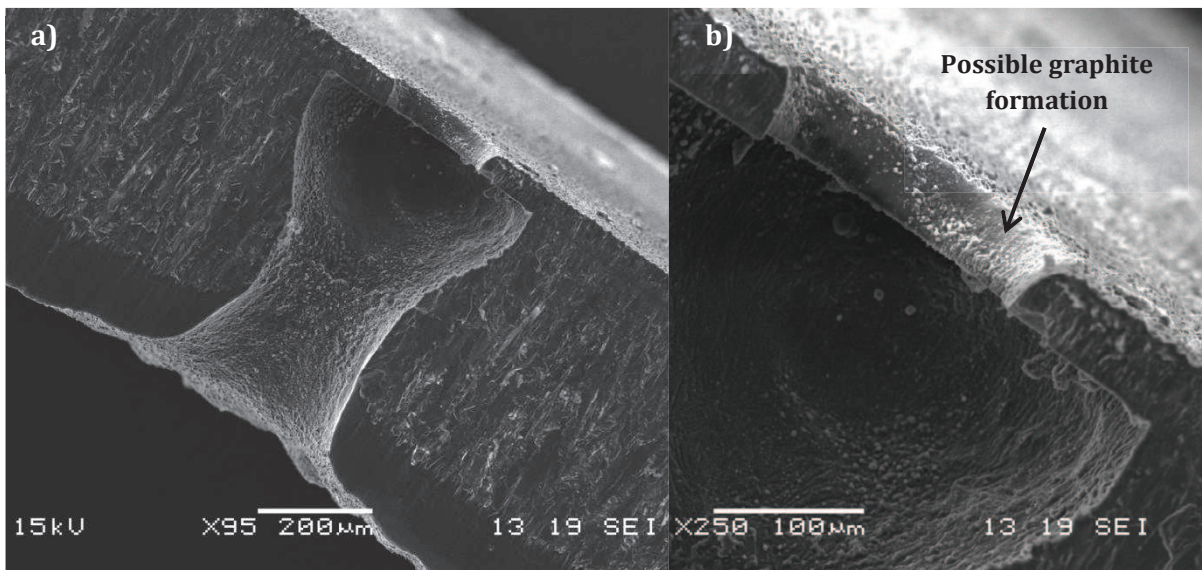

Figure 3.15. SEM images of the aperture of a bisected 200 μm device after high pressure operation for ~5 hours. b) shows a possible area of graphite formation on the insulating layer surface,

3.6 Arrays

To produce useful quantities of radiation, large numbers of microplasmas are required, hence functioning arrays are a key goal in microplasma research. Two arrayed devices in this project were investigated, featuring a 2×2 and 3×3 array. The microplasmas were operated in parallel, with neither device featuring individual ballasts.

Independent of the pressure, when operated under DC, only one microplasma struck. However, when operated under high frequency (1 kHz) pulsed DC, a more even power distribution was observed with multiple holes lighting up simultaneously. Park *et al.* recorded similar observations; excitation frequencies of 10 kHz were required to produce an even power distribution.[100]

When operated above 2 mA, the devices were functioning in the normal mode, with a flat or slightly positive V-I characteristic. As such it should be possible for simultaneous operation.[60, 99] However, the use of such high frequencies means it is difficult to assess whether several microplasmas are operating simultaneously or only one discharge is struck at any one moment. The use of a high speed camera or larger arrays might be able to determine this.
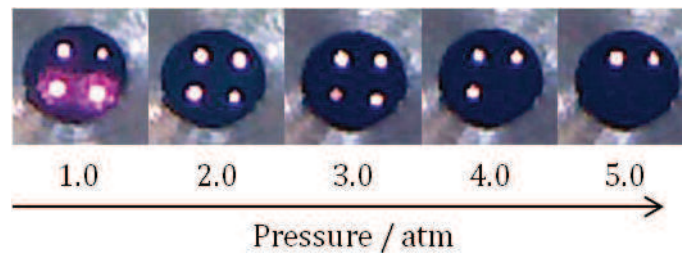
Figure 3.16. The 2×2 array operating at different pressures under 1 kHz pulsed DC (max current = 8 mA). The most consistent power distribution was observed at 2.0 atm.

Power distribution also depended on pressure, with most consistent operation at 2 atm, as shown in Figure 3.16. At lower pressures streamers formed within the holes closest to the copper lid. These holes were illuminated preferentially, suggesting the streamers stabilised the individual discharges. At higher pressures the increased breakdown voltage might ensure a greater dependency on hole morphology. If this were the case, the holes with the slightly lower breakdown voltage would illuminate more strongly.

The 3×3 (150 μm) device performed poorly. However, rather than this being a consequence of a greater number of holes, it is more likely to be due to more inconsistent holes. It was noted that, perhaps because of their small size, the holes were poorly formed and uneven. Nonetheless, despite this, the device still operated (Figure 3.17).
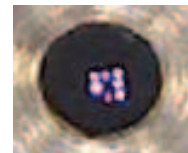

Figure 3.17. The 3×3 array operating at 2 atm under 1 kHz pulsed DC (max current = 8 mA).

Initial results are promising; arrays were simple to fabricate and worked well when operated under high frequency pulsed DC. To investigate this issue further, larger, more consistently formed arrays would need to be examined.

3.7 Slit Geometry

An alternative to using large arrays is to fabricate long slits. Devices with slit geometries exhibited V-I characteristics similar in shape to those described in Section 3.2. When operated at 8 mA and up to three atmospheres the plasma spread along the entire slit. At higher pressures the plasma contracted and developed in only part of the slit, see Figure 3.18. Above 3 atm higher currents were required for the plasma to saturate the slit.
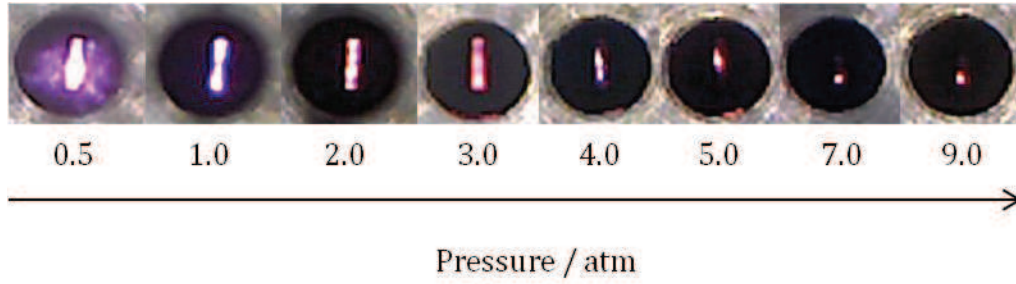
Figure 3.18. A 1000 µm × 200 µm slit device operating at 8 mA under different pressures. As pressure increases the plasma contracts and withdraws to a corner of the slit.

Similar to observations of circular cavities, upon increasing current, the plasma expanded and spread throughout the slit. This was also observed in the slit device investigated by Wang & Ouyang.[165]

3.8 Gas Temperature Measurements

The rotational temperature, T_R and vibrational temperature, T_{vib} of the N_2 C $^3\Pi_u$ molecules were determined for operation of a 300 µm device at 8 mA under pressures between 0.5 and 4.0 atm (He with trace N_2) by analysis of the second positive system of nitrogen.

3.8.1 Rotational Temperature

T_R was found not to vary with pressure, instead it remained constant at around 400 K. To evaluate whether T_R is equal to T_g, the rotational to translational (R-T) energy transfer between helium and N_2 C $^3\Pi_u$, shown in Equation 3.1 needs to be examined.

$$N_2 \ (C \ ^3\Pi_u, \ v', \ J') + He \ \xrightarrow{k_{R\text{-}T}} \ N_2 \ (C \ ^3\Pi_u, \ v', \ J'') + He \tag{3.1}$$

Above 0.5 atm the time between these collisions, $\tau_{R\text{-}T}$ ($1/k_{R\text{-}T} \cdot n_{He}$) is far greater than the radiative lifetime of the C state, τ_C. Furthermore, other processes, such as electronic quenching, occur too rarely to affect the distribution of rotational energy levels.[138] Consequently, the N_2 C $^3\Pi_u$ molecules are in rotational equilibrium with the helium atoms and it can be assumed that $T_R = T_g$.
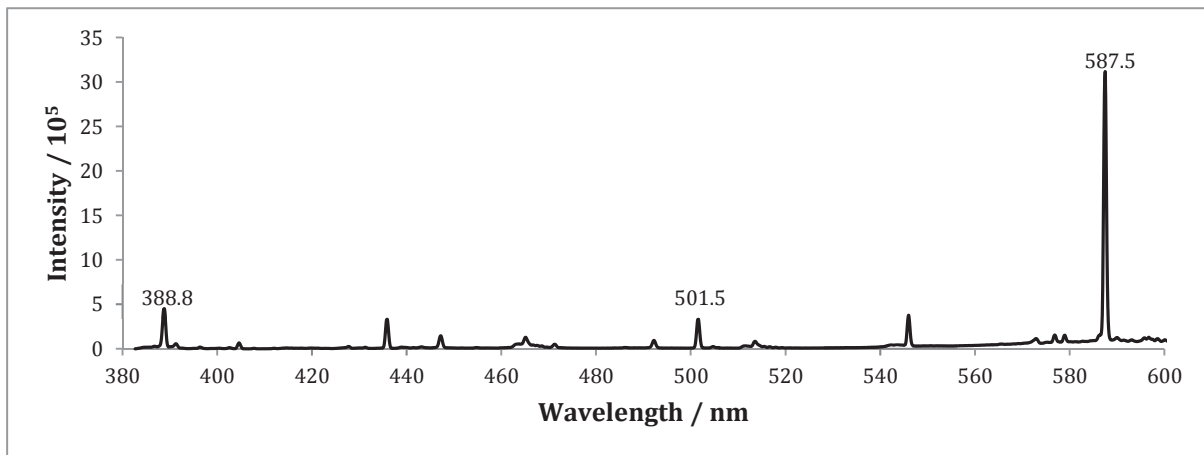
Figure 3.19. The spectrum for a device operating under helium (1 atm) and 4 mA between 380 and 600 nm. Several helium lines are observed, including the line at 501.5 nm, which would not be present if T_e = 400 K.

The low gas temperature indicates that energy is being effectively transferred away from the centre of the plasma, both by the thermally conductive helium and diamond. Indeed, other atmospheric pressure helium microplasmas have also been determined to be around 400 K.[138, 166, 167]

The non-thermal properties of the plasma are further confirmed by the low gas temperature. An electron temperature as low as 400 K would be inadequate to sustain a helium plasma. Furthermore, several of the lines seen in the helium spectra are only observable at electron temperatures greater than 10000 K, such as the line visible at 501.5 nm (Figure 3.19).[168]

The consistency of the gas temperatures with pressure was slightly unexpected. It was initially thought that temperature would increase with pressure as the plasma contracted and density increased. However, the relative errors associated with such low gas temperatures are quite large ($\sim\pm20$ K). Consequently the results may not be accurate enough for a subtle relationship to be discerned. Additionally, only the brightest part of the plasma is measured, this volume is not necessarily representative of the entire plasma.

3.8.2 Vibrational Temperature

The same bands were used to determine the vibrational temperature, T_{vib}. An almost exponential relationship with pressure was observed, shown in Figure 3.20. The vibrational temperature at 0.5 atm is roughly 12500 K, a completely unrealistic value for a gas temperature of 400 K. Consequently it is evident that the N_2 C $^3\Pi_u$ molecules are not in vibrational equilibrium with the gas. This should be expected: helium's monoatomic nature means that vibrational energy transfer from N_2 C $^3\Pi_u$ to He must be much slower than τ_C and the energy levels do not follow a Boltzmann distribution. Instead the distribution represents the vibrational levels the C state is formed in.
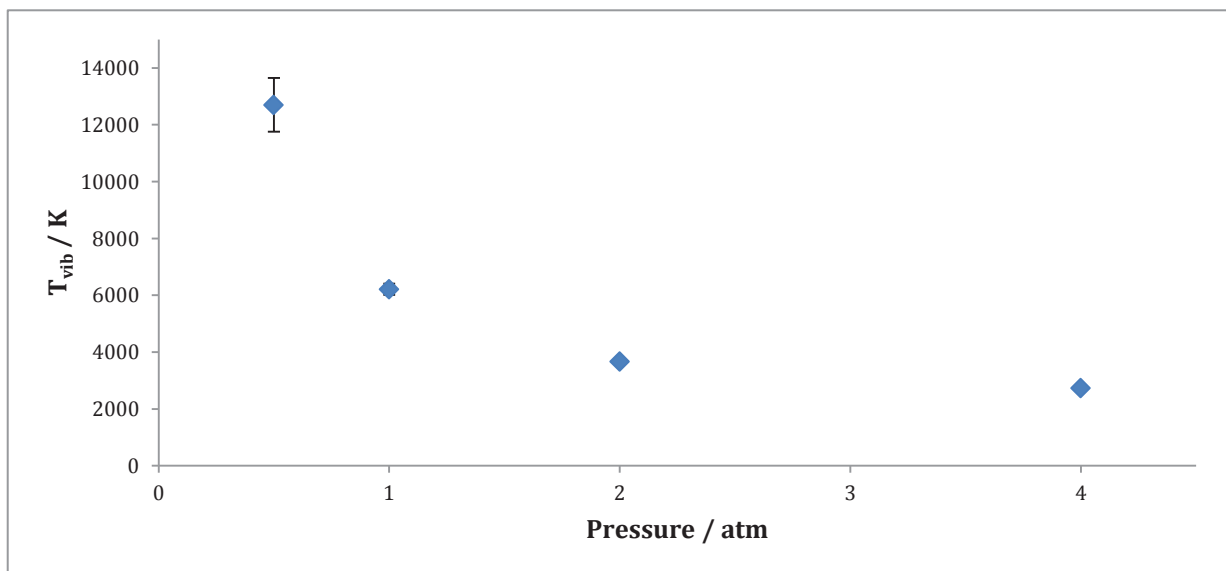
Figure 3.20. Measured vibrational temperature as a function of pressure. The temperatures at low pressures are too high to represent a real vibrational temperature, instead the temperatures represent a non-Boltzmann distribution of the two vibrational energy levels examined.

Within a primarily helium plasma, trace N_2 (C $^3\Pi_u$) molecules are formed by many processes. Predominant processes include electron excitation of ground state N_2 (1), the formation and subsequent quenching of the long lifetime metastable N_2 (A $^3\Sigma^+_u$) via the 'pooling' reaction (2, 3) and collisions with helium metastables, He_m (4):[169, 170]

$$N_2 (X\ ^1\Sigma^+_g) + e^- \rightarrow N_2 (C\ ^3\Pi_u) + e^- \tag{1}$$

$$N + N + He \rightarrow N_2 (A\ ^3\Sigma^+_u) + He \tag{2}$$

$$N_2 (A\ ^3\Sigma^+_u) + N_2 (A\ ^3\Sigma^+_u) \rightarrow N_2 (C\ ^3\Pi_u) + N_2 (X\ ^1\Sigma^+_g) \tag{3}$$

$$N_2 (X\ ^1\Sigma^+_g) + He_m \rightarrow N_2 (C\ ^3\Pi_u) + He \tag{4}$$
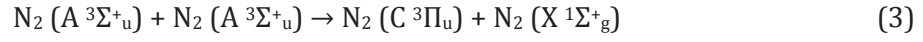
Naturally, different formation processes will preferentially form C state molecules in different vibrational states. Furthermore, in contrast to electron excitation (1), the formation of the C state molecules via the 'pooling' reaction (2, 3) and collisions with metastable helium atoms (4) are both dependent on helium concentrations and thus would be affected by pressure. It is therefore likely that the differences in vibrational temperature shown in Figure 3.20 are due to the rates and contributions of these processes altering with pressure. At 0.5 atm it is possible excitation processes dominate forming more N_2 (C $^3\Pi_u$, v = 3) molecules whereas at 4.0 atm collisional processes dominate forming more N_2 (C $^3\Pi_u$, v = 2) molecules.

3.9 Excitation Temperature Measurements

Boltzmann plots using helium and neon, shown in Figures 3.21 and 3.22, gave excitation temperatures of 3800 and 3400 K respectively, for a plasma operating at 1 atm and 8 mA. Both values are similar, which might suggest they are relatively accurate. Other groups have used both neon and helium to determine T_{exc}.[171-173] Values for helium based atmospheric microplasmas range from 1900 to 4000 K, a range that encompasses the temperatures measured in this project.[174]
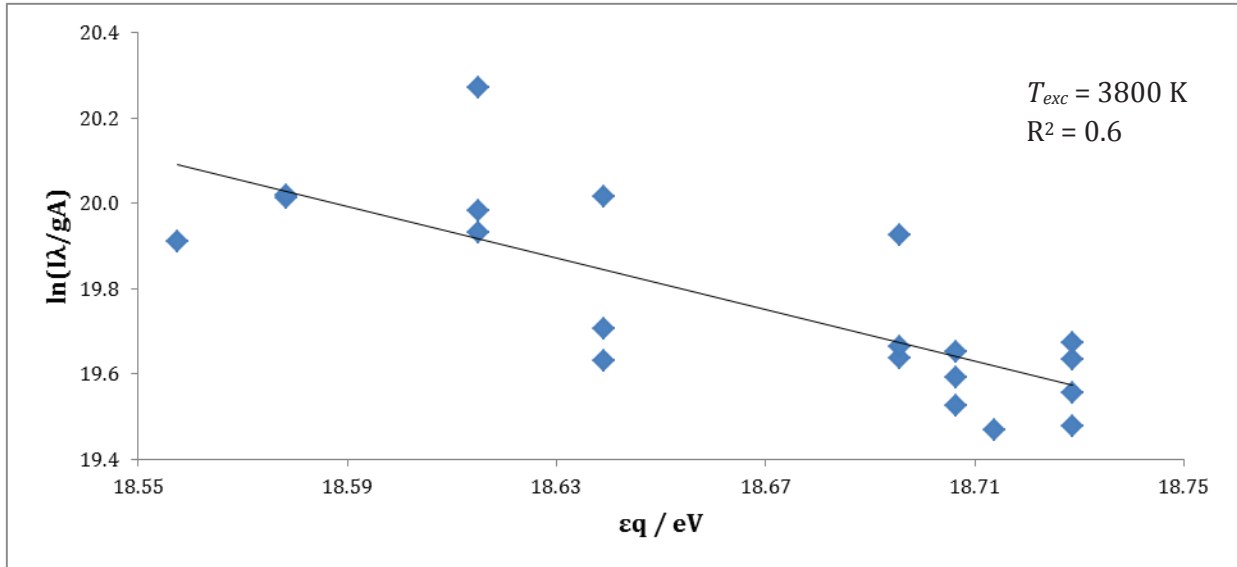
Figure 3.21. The Boltzmann plot for a device operated at 1 atm (50:50 Ne:He) and 8 mA using neon spectral lines. T_{exc} was determined to be 3800 K. A coefficient of determination (R^2) of 0.6 suggests this is not very accurate.

However, the usefulness of excitation temperature as a characterisation tool, particularly for atmospheric helium plasmas, has been disputed. A study by Jonkers & van der Mullen came to the conclusion that T_{exc} is not related to any useful plasma parameter. The high ionisation potential of helium combined with its high diffusivity cause the plasmas to deviate from thermal equilibrium. Furthermore, the relatively few lines observable in the spectrum and the closeness of the upper energy levels associated with these lines ensures that T_{exc} is almost always found to be around 3500 K, as in this study.[175]

Consequently, T_{exc} was not deemed to be a useful plasma parameter and further measurements were not pursued. Despite this, investigations of T_{exc} might be useful when investigating device function under other gases.
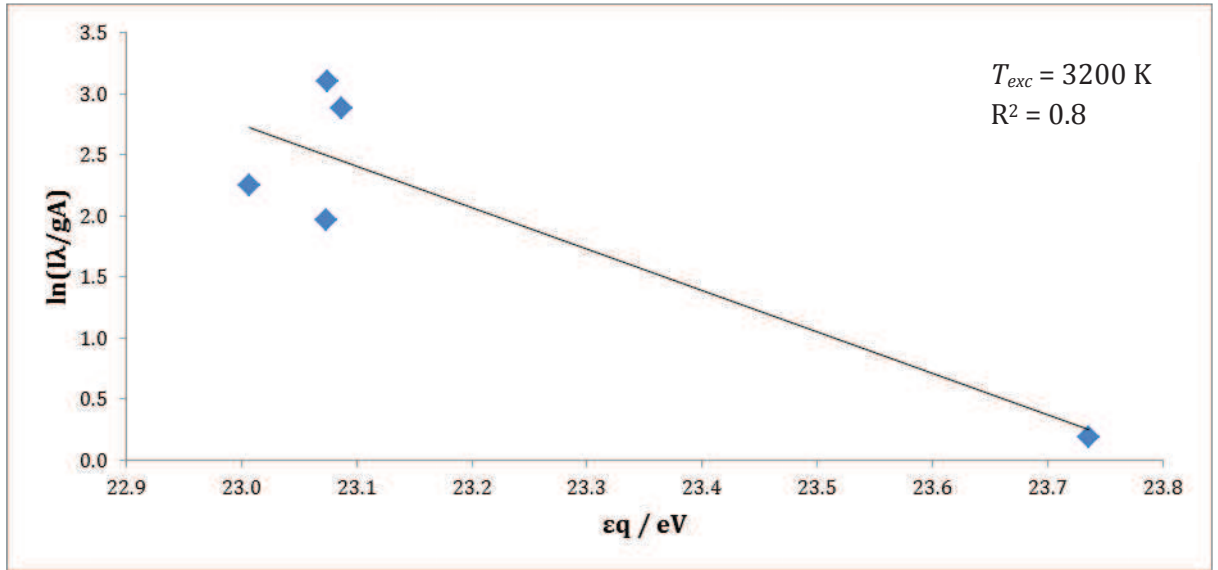
Figure 3.22. The Boltzmann plot for a device operated at 1 atm (pure He) and 8 mA using helium spectral lines. T_{exc} was determined to be 3200 K. The coefficient of determination (R^2) was 0.8.

4 Afterword

4.1 Conclusion

The overarching aims of the project were the fabrication of diamond microplasma devices capable of operating above atmospheric pressure and the characterisation of these high pressure plasmas.

Over a dozen working MHCD devices were fabricated out of diamond. They featured a range of aperture shapes and sizes, and included two arrays. When operated using the specially designed sample holder, good electrical conductivity and consistent operation were achieved.

Devices were capable of operating between 0.5 and 9.5 atmospheres, the limit of the pressure chamber. Smaller single holed devices showed stable operation at 9.5 atm for over 30 minutes.

Microplasmas formed over the full range of pressures were characterised well using both OES and voltage-current measurements. From this characterisation four conclusions were drawn:

1. At all pressures, the devices were operating in the glow discharge mode in a similar manner to low pressure microplasmas. This was evaluated from the low temperature of 400 K observed between 0.5 and 4.0 atm, suggesting highly non-thermal plasmas with T_e $\gg T_g$. A second strong indication was the similarity of the V-I characteristics to conventional glow discharges and low pressure microplasmas; in addition to the predischarge and self-pulsing modes a stable normal mode was observed.

2. There was a subtle change in device operation upon pressure increase. An increase in pressure was accompanied by visible contraction of the plasma coupled with slight but consistent differences in the normal mode V-I characteristics. Possible explanations for these differences were suggested.

3. The devices followed the traditional Townsend breakdown mechanism. This was determined from the three Paschen curves. The curves were very similar in shape to the theoretical helium paschen curve. The shift of the curve to higher breakdown voltages was attributed to the non-planar geometry of the devices.

4. A slight dependency on hole diameter for stable operation at high pressures was observed. This suggests a scaling law akin to the Allis-white similarity law might be active above atmospheric pressure operation.

Considering the harsh conditions associated with high pressure microplasmas, relatively little permanent damage was incurred during operation. The localisation of damage to the cathode suggests it was primarily due to sputtering. This is further indicated by the low gas temperatures. Although graphitisation occurred after roughly an hour of operation, causing shorting, the graphite was easily removed by acid washing. It can be concluded, therefore, that diamond is fairly resistant to damage, an effective material for transporting heat away from the plasma and, through these, an excellent material for microplasma fabrication.

When operated under high frequency pulsed DC, a 2×2 array functioned well and featured good power distribution between all holes at 0.5 to 3 atm. Consequently, high pressure arrayed devices were proven feasible, providing a foundation for the operation of larger arrays.

All six sub-objectives specified in Section 1.12 were achieved, as shown in Table 4.1. As such, the two overarching objectives have also been accomplished:

- Diamond microplasma devices have proved to be an effective strategy for accessing high pressure operation.
- Stable microplasmas were formed and characterised at pressures higher than ever before.

It can therefore be concluded that the project has been a success. Additionally there is vast scope for future work, as suggested in the next section.

Table 4.1. The original sub-objectives and the achievements corresponding to each of them.

Sub-Objective	Achievement
1. Design and fabricate microplasma devices adhering to the following criteria: - A MHCD type geometry - Components exposed to high temperatures (cathode and dielectric) made out of diamond - Good electrical contact between device and circuitry - Capable of consistent breakdown - A range of aperture sizes	Over a dozen working devices adhering to these criteria were fabricated. Apertures ranged from 40 – 600 μm. See Sections 2.1 – 2.2.
2. Develop and fabricate a device of similar design consisting of an array of microplasmas.	Two working arrays (2×2 and 3×3) were fabricated following the criteria of objective 1.
3. Operate the devices at pressures of up to ten atmospheres.	Devices were operated consistently between 0.5 and 9.5 atm, limited only by the pressure chamber capability. See Section 3.3.
4. Characterise the microplasmas using the following techniques: - Voltage and current measurements to obtain Paschen curves and V-I characteristics - OES measurements to determine species' temperatures and densities	Voltage-current measurements were used to obtain Paschen curves and V-I characteristics. See Sections 2.7, 3.1 and 3.3. Although not used to measure densities, OES was used to determine gas temperatures. See Section 3.8.
5. Explain the microplasma characteristics in terms of their fundamental physics and by comparing them to well-characterised microplasmas operated at lower pressures.	Results were compared to similar, lower pressure devices. Possible physical explanations were provided to explain observations. See Section 3.

6. Assess the feasibility of diamond as a material used to fabricate microplasma devices by observing damage after high pressure operation.	Only a relatively small amount of damage was observed after device operation. It was concluded, therefore, that diamond is a feasible material for device fabrication. See Section 3.5.

4.2 Future Work

Two different types of future work have been identified:

1. Development of the investigations presented here to validate findings, and
2. Investigation into properties not yet explored.

There are several suggestions for development of current investigations:

- At low pressures it was unclear how much the copper influenced the microplasma properties. Consequently, it would be beneficial to modify the sample holder to ensure the copper lid was far enough away from the device aperture to prevent interaction.

- Although it is likely that the oscillations observed at roughly 1 mA were due to the self-pulsing mode, this is not for certain. A charged-coupled device (CCD) detector could be used to record high resolution images of the microplasma during oscillations and validate the regime.

- The origin of sputtered material surrounding the cathode after operation is unknown. Techniques such as EDX could be used to identify the composition of these particles.

- Fabrication of uniform, well-drilled, holes with $D < 200$ µm was difficult. Realignment of the laser, or the use of thinner B-doped wafers could solve this issue. These could be used to fabricate and investigate much smaller devices. In addition, larger consistently formed arrays would also be more accessible.

Investigation into unexplored properties is broader and less well defined. However:

- Further plasma properties could be characterised, such as electron density and temperature. One possible method would be to use high resolution spectroscopy and Stark broadening.

- Considering the potential applications of microplasmas, exploring the radiative emission of devices and how this varies with pressure is important. A sensitive photodiode or use of a CCD detector could be used to determine this.

- Only helium, the most favourable gas for high pressures was used. It would be beneficial to investigate how the device functions with different gases, especially those featuring useful radiative frequencies, such as xenon.

- As the majority of damage was from sputtering rather than high gas temperatures, it would be interesting to investigate the operation of a radio frequency AC device. Although this should reduce sputter damage, the device would have to be redesigned to enable AC operation.

4.3   Acknowledgements

5 References

1. J. G. Eden, S. J. Park, J. H. Cho, M. H. Kim, T. J. Houlahan, B. Li, E. S. Kim, S. K. Lee, K. S. Kim, J. K. Yoon, S. H. Sung, P. Sun, C. M. Herring and C. J. Wagner, *IEEE Trans. Plasma Sci.*, 2013, **41**, 661.
2. K. H. Becker, K. H. Schoenbach and J. G. Eden, *J. Phys. D: Appl. Phys.*, 2006, **39**, R55.
3. J. G. Eden, S. J. Park, N. P. Ostrom, S. T. McCain, C. J. Wagner, B. A. Vojak, J. Chen, C. Liu, P. v. Allmen, F. Zenhausern, D. J. Sadler, C. Jensen, D. L. Wilcox and J. J. Ewing, *J. Phys. D: Appl. Phys.*, 2003, **36**, 2869.
4. R. Foest, M. Schmidt and K. Becker, *Int. J. Mass. Spectrom.*, 2006, **248**, 87.
5. R. J. Goldston and P. H. Rutherford, *Introduction to Plasma Physics*, Institute of Physics Publishing, Bristol, 1995.
6. D. A. Gurnett and A. Bhattacharjee, *Introduction to Plasma Physics: with Space and Laboratory Applications*, Cambridge University Press, Cambridge, 2005.
7. P. M. Bellan, *Fundamentals of Plasma Physics*, Cambridge University Press, New York, 2008.
8. B. Chapman, *Glow Discharge Processes*, John Wiley & Sons, Toronto, 1980.
9. M. D. Calzada, M. Moisan, A. Gamero and A. Sola, *J. Appl. Phys.*, 1996, **80**, 46.
10. A. Bogaerts, E. Neyts, R. Gijbels and J. v. d. Mullen, *Spectrochimica Acta Part B*, 2002, **57**, 609.
11. M. I. Boulos, P. Fauchais and E. Pfender, *Thermal Plasmas: Fundamentals and Applications*, Plenum Press, New York, 1994.
12. C. Tendero, C. Tixier, P. Tristant, J. Desmaison and P. Leprince, *Spectrochimica Acta Part B*, 2006, **61**, 2.
13. G. M. W. Kroesen, D. C. Schram and J. C. M. d. Haas, *Plasma Chem. Plasma Proc.*, 1990, **10**, 531.
14. A. Gleizes, J. J. Gonzales and P. Freton, *J. Phys. D: Appl. Phys.*, 2005, **38**, R153.
15. H. R. Griem, *Phys. Rev.*, 1962, **128**, 997.
16. B. Basu and N. J. Grossbard, *Phys. Plasmas*, 2011, **18**, 092106-092101.
17. D. Summers and R. M. Thorne, *Phys. Fluids B*, 1991, **3**, 1835.
18. C. G. Wilson, Y. B. Gianchandani, R. R. Arslanbekov, V. Kolobov and A. E. Wendt, *J. Appl. Phys.*, 2003, **94**, 2845.
19. N. S. J. Braithwaite, *Plasma Sources Sci. Technol.*, 2000, **9**, 517.
20. F. M. Penning, *Electrical Discharges in Gases*, Philips Technical Library, Eidenhoven, 1957.
21. R. A. Treumann, Z. Klos and M. Parrot, *Space Sci. Rev.*, 2008, **137**, 133.
22. R. S. Mason, D. J. Mitchell and P. M. Dickinson, *Phys. Chem. Chem. Phys.*, 2010, **12**, 3698.
23. F. Llewellyn-Jones, *The Glow Discharge and an Introduction to Plasma Physics*, Methuen & Co., London, 1966.
24. F. Llewellyn-Jones and W. D. Owen, *Proc. Phys. Soc.*, 1964, **83**, 283.
25. A. Fridman, *Plasma Chemistry*, Cambridge University Press, New York, 2008.
26. J. J. Lowke, *Plasma Sources Sci. Technol.*, 2013, **22**, 023002.
27. J. J. Lowke, 19th Int. Conf. on Gas Discharges and their Applications, Tsingua University, Beijing, 2012.
28. F. Massines, N. Gerardi, N. Naude and P. Segur, *Plasma Phys. Control. Fusion*, 2005, **47**, B577.
29. V. I. Kolobov and A. Fiala, *Phys. Rev. E*, 1994, **50**, 50.
30. K. Takaki, D. Taguchi and T. Fujiwara, *Appl. Phys. Lett.*, 2001, **78**, 2646.
31. A. A. Yahya and J. E. Harry, *Int. J. Electronics*, 1999, **86**, 755.
32. H. V. Boenig, *Fundamentals of Plasma Chemistry and Technology*, Technomic Publishing Company, Lancaster, 1988.

33. K. S. S. Harsha, *Principles of Vapor Deposition of Thin Films*, Elsevier, Oxford, 2006.
34. V. I. Arkhipenko, A. A. Kirillov, Y. A. Safronau and L. V. Simonchik, *Eur. Phys. J. D*, 2010, **60**, 455.
35. C. Lazzaroni and P. Chabert, *J. Phys. D: Appl. Phys.*, 2011, **44**, 445202.
36. U. Valbusa, C. Boragno and F. B. d. Mongeot, *J. Phys.: Condens. Matter*, 2002, **14**, 8153.
37. S. M. Rossnagel, *Thin Solid Films*, 1995, **263**, 1.
38. J. Hopwood, F. Iza, S. Coy and D. B. Fenner, *J. Phys. D: Appl. Phys.*, 2005, **38**, 1698.
39. D. W. Oxtoby, H. P. Gillis and N. H. Nachtrieb, *Principles of Modern Chemistry*, Thomson Learning, London, 2002.
40. Y. E. S. Eliezer, *The Fourth State of Matter: An Introduction to Plasma Science*, 2nd edn., Institute of Physics Publishing, Bristol, 2001.
41. F. Paschen, *Ann. Phys.*, 1889, **37**, 69.
42. R. Arora and W. Mosch, *High Voltage Insulation Engineering*, New Age International, New Delhi, 1995.
43. A. Fridman and L. A. Kennedy, *Plasma Physics and Engineering*, Taylor & Francis Books, New York, 2004.
44. D. B. Go and D. A. Pohlman, *J. Appl. Phys.*, 2010, **107**, 103303.
45. W. S. Boyle and P. Kisliuk, *Phys. Rev.*, 1955, **97**, 255.
46. R. Gayet, C. Harel, T. Josso and H. Jouin, *J. Phys. D: Appl. Phys.*, 1996, **29**, 3063.
47. R. Tirumala and D. B. Go, *Appl. Phys. Lett.*, 2010, **97**, 151502.
48. F. Iza, G. J. Kim, S. M. Lee, J. K. Lee, J. L. Walsh, Y. T. Zhang and M. G. Kong, *Plasma Process. Polym.*, 2008, **5**, 322.
49. E. Lennon, J. Farr and R. Besser, *Expert Syst. Appl.*, 2013, **40**, 6321.
50. J. Guikema, N. Miller, J. Niehof, M. Klein and M. Walhout, *Phys. Rev. Lett.*, 2000, **85**, 3817.
51. M. Klein, N. Miller and M. Walhout, *Phys. Rev. E*, 2001, **64**, 026402.
52. J. Hopwood and F. Iza, *J. Anal. At. Spectrom.*, 2004, **19**, 1145.
53. G. Stockhausen and M. Kock, *J. Phys. D: Appl. Phys.*, 2001, **34**, 1683.
54. A. E. Dubinov, S. K. Saikov and L. A. Senilov, *Tech. Phys.*, 2012, **57**, 1199.
55. D. Maric, N. Skoro, G. Malovic, Z. L. Petrovic, V. Mihailo and R. Djulgerova, *J. Phys.: Conf. Ser.*, 2009, **162**, 012007.
56. A. D. White, *J. Appl. Phys.*, 1959, **30**, 711.
57. D. J. Sturges and H. J. Oskam, *J. Appl. Phys.*, 1964, **35**, 2887.
58. K. H. Schoenbach, A. El-Habachi, W. Shi and M. Ciocca, *Plasma Sources Sci. Technol.*, 1997, **6**, 468.
59. J. P. Boeuf, L. C. Pitchford and K. H. Schoenbach, *Appl. Phys. Lett.*, 2005, **86**, 071501.
60. K. H. Schoenbach, R. Verhappen, T. Tessnov, F. E. Peterkin and W. W. Byszewski, *Appl. Phys. Lett.*, 1996, **68**, 13.
61. M. Miclea, K. Kunze, U. Heitmann, S. Florek, J. Franzke and K. Niemax, *J. Phys. D: Appl. Phys.*, 2005, **38**, 1709.
62. M. J. Kushner, *J. Phys. D: Appl. Phys.*, 2005, **38**, 1633.
63. J. Greenan, C. M. O. Mahony, D. Mariotti and P. D. Maguire, *Plasma Sci. Technol.*, 2011, **20**, 025011.
64. D. D. Hsu and D. B. Graves, *J. Phys. D: Appl. Phys.*, 2003, **36**, 2898.
65. M. K. Kulsreshath, N. Sadeghi, L. Schwaederle, T. Dufour, L. J. Overzet, P. Lefaucheux and R. Dussart, *J. Appl. Phys.*, 2013, **114**, 243303.
66. X. Aubert, G. Bauville, J. Guillon, B. Lacour, V. Puech and A. Rousseau, *Plasma Sources Sci. Technol.*, 2007, **16**, 23.
67. P. Chabert, C. Lazzaroni and A. Rousseau, *J. Appl. Phys.*, 2010, **108**, 113307.
68. C. Lazzaroni and P. Chabert, *Plasma Sources Sci. Technol.*, 2011, **20**, 055004.
69. B. N. Sismanoglu and J. Amorim, *Eur. Phys. J. Appl. Phys.*, 2008, **41**, 165.
70. B. N. Sismanoglu, C. L. A. Cunha, M. P. Gomes, R. Caetano and K. G. Grigorov, *Braz. J. Phys*, 2010, **40**, 459.
71. M. P. Gomes, B. N. Sismanoglu and J. Amorim, *Braz. J. Phys*, 2009, **39**, 25.

72. M. Moselhy, W. Shi, R. H. Stark and K. H. Schoenbach, *IEEE Trans. Plasma Sci.*, 2002, **30**, 198.
73. S. J. Park, J. Chen, C. Liu and J. G. Eden, *Appl. Phys. Lett.*, 2001, **78**, 419.
74. J. Chen, S. J. Park, Z. Fan, J. G. Eden and C. Liu, *J. Microelectromech. Syst.*, 2002, **11**, 536.
75. E. A. Lennon, A. A. Burke and R. S. Besser, *Curr. Appl. Phys*, 2012, **12**, 1064.
76. J. W. Frame, D. J. Wheeler, T. A. DeTemple and J. G. Eden, *Appl. Phys. Lett.*, 1997, **71**, 1165.
77. P. S. Kothnur and L. L. Raja, *J. Appl. Phys.*, 2005, **97**, 043305.
78. X. Zhang, X. Wang, F. Liu and Y. Lu, *IEEE Trans. Plasma Sci.*, 2009, **37**, 2055.
79. *US Pat.*, US 2005/0183996 A1, 2005.
80. J. P. Boeuf, *J. Phys. D: Appl. Phys.*, 2003, **36**, R53.
81. H. Hirakawa, M. Ishimoto, K. Awamoto and T. Shinoda, *J. Display Technol*, 2010, **6**, 381.
82. P. v. Allmen, D. J. Sadler and C. Jensen, *Appl. Phys. Lett.*, 2003, **82**, 4447.
83. K. H. Schoenbach and W. Zhu, *IEEE J. Quantum Electron.*, 2012, **48**, 768.
84. T. Yamasaki, S. Namba, K. Takiyama and H. Nojima, *Jpn. J. Appl. Phys.*, 2012, **51**, 126101.
85. P. J. Lindner, S. Y. Hwang and R. S. Besser, *Energy Fuels*, 2013, **27**, 4432.
86. P. J. Lindner and R. S. Besser, *Chem. Eng. Technol.*, 2012, **35**, 1249.
87. H. Qiu, K. Martus, W. Y. Lee and K. H. Becker, *Int. J. Mass. Spectrom.*, 2004, **233**, 19.
88. M. H. Kim, J. H. Cho, S. B. Ban, R. Y. Choi, E. J. Kwon, S. J. Park and J. G. Eden, *J. Phys. D: Appl. Phys.*, 2013, **46**, 305201.
89. A. Koutsospyros, S. M. Yin, C. Christodoulatos and K. Becker, *Int. J. Mass. Spectrom.*, 2004, **233**, 305.
90. A. D. Koutsospyros, S. M. Yin, C. Christodoulatos and K. Becker, *IEEE Trans. Plasma Sci.*, 2005, **33**, 42.
91. K. Hensel, *Eur. Phys. J. D*, 2009, **54**, 141.
92. X. T. Deng, J. J. Shi, H. L. Chen and M. G. Kong, *Appl. Phys. Lett.*, 2007, **90**, 013903.
93. A. Smith, M. Dickson, J. Aitkin and J. Bagg, *J. Hosp. Infect.*, 2002, **51**, 233.
94. J. Julak, O. Janouskova, V. Scholtz and K. Holada, *Plasma Process. Polym.*, 2011, **8**, 316.
95. D. Luo and Y. Duan, *Trends Anal. Chem.*, 2012, **39**, 254.
96. M. Miclea, K. Kunze, J. Franzke, F. Leis, K. Niemax, C. Penache, O. Hohn, S. Schossler, T. Jahnke, A. Brauning-Demian and H. Schmidt-Bocking, in *Proc. Hakone VIII*, Puehajaerve, Estonia, 2002, vol. 1, p. 206.
97. R. Guchardi and P. C. Hauser, *J. Anal. At. Spectrom.*, 2003, **18**, 1056.
98. R. Guchardi and P. C. Hauser, *J. Anal. At. Spectrom.*, 2004, **19**, 945.
99. M. K. Kulsreshath, L. Schwaederle, L. J. Overzet, P. Lefaucheux, J. Ladroue, T. Tillocher, O. Aubry, M. Woytasik, G. Schelcher and R. Dussart, *J. Phys. D: Appl. Phys.*, 2012, **45**, 285202.
100. S. J. Park, K. F. Chen, N. P. Ostrom and J. G. Eden, *Appl. Phys. Lett.*, 2005, **86**, 111501.
101. W. Shi, R. H. Stark and K. H. Schoenbach, *IEEE Trans. Plasma Sci.*, 1999, **27**, 16.
102. A. El-Habachi, W. Shi, M. Moselhy, R. H. Stark and K. H. Schoenbach, *J. Appl. Phys.*, 2000, **88**, 3220.
103. R. Dussart, L. J. Overzet, P. Lefaucheux, T. Dufour, M. Kulsreshath, M. A. Mandra, T. Tillocher, O. Aubry, S. Dozias, P. Ranson, J. B. Lee and M. Goeckner, *Eur. Phys. J. D*, 2010, **60**, 601.
104. W. S. Boyle and F. E. Haworth, *Phys. Rev.*, 1956, **101**, 935.
105. A. A. Yaha and J. E. Harry, *Int. J. Electronics*, 1999, **86**, 755.
106. J. C. T. Eijkel, H. Stoeri and A. Manz, *Anal. Chem.*, 1999, **71**, 2600.
107. C. Meyer, R. Heming, E. L. Gurevich, U. Marggraf, M. Okruss, S. Florek and J. Franzke, *J. Anal. At. Spectrom.*, 2011, **26**, 505.
108. H. Chang, C. Ryu, S. J. Yoo, S. B. Kim and S. J. You, *J. Phys. D: Appl. Phys.*, 2012, **45**, 195206.
109. H. Wei, L. Xinghua, X. Richang, C. Suhong, L. Ruijin, F. Yang and X. Hanguang, *Plasma Sci. Technol.*, 2013, **15**, 335.
110. J. Choi, F. Iza, J. K. Lee and C. Ryu, *IEEE Trans. Plasma Sci.*, 2007, **35**, 1274.
111. S. G. Belostotskiy, T. Ouk, V. M. Donnelly, D. J. Economou and N. Sadeghi, *J. Appl. Phys.*, 2010, **107**, 053305.

112.   M. Mobli, R. Mahamud and T. I. Farouk, in *Pulsed Power Conference, 19th IEEE*, San Francisco, 2013, p. 1.

113.   D. Mariotti, J. A. McLaughlin and P. Maguire, *Plasma Sources Sci. Technol.*, 2004, **13**, 207.

114.   J. Cazaux, *Appl. Surf. Sci.*, 2010, **257**, 1002.

115.   V. Karanassios, K. Johnson and A. T. Smith, *Anal. Bioanal. Chem.*, 2007, **388**, 1595.

116.   J. M. Bustillo, R. T. Howe and R. S. Muller, *P. IEEE*, 1998, **86**, 1552.

117.   N. P. Ostrom and J. G. Eden, *Appl. Phys. Lett.*, 2005, **87**, 141101.

118.   L. Schwaederle, M. K. Kulsreshath, L. J. Overzet, P. Lefaucheux, T. Tillocher and R. Dussart, *J. Phys. D: Appl. Phys.*, 2012, **45**, 065201.

119.   *CRC Handbook of Chemistry and Physics*, 94th edn., CRC Press, Boca Raton, 2013.

120.   M. N. R. Ashfold, P. W. May, C. A. Rego and N. M. Everitt, *Chem. Soc. Rev.*, 1994, **23**, 21.

121.   P. W. May, *Phil. Trans. R. Soc. Lond. A*, 2000, **358**, 473.

122.   L. Diedrich, O. M. Kuttel, P. Aebi and L. Schkapbach, *Surf. Sci.*, 1998, **418**, 219.

123.   T. Yokoya, T. Nakamura, T. Matsushita, T. Muro, Y. Takano, M. Nagao, T. Takenouche, H. Kawarada and T. Oguchi, *Nature*, 2005, **438**, 647.

124.   A. Kraft, *Int. J. Electrochem. Sci.*, 2007, **2**, 355.

125.   S. Mitea, M. Zeleznik, M. D. Bowden, P. W. May, N. A. Fox, J. N. Hart, C. Fowler, R. Stevens and N. S. Braithwaite, *Plasma Sources Sci. Technol.*, 2012, **21**, 1.

126.   R. Windholz and P. A. Molian, *J. Mater. Sci.*, 1997, **32**, 4295.

127.   T. Chang, S. Lou, H. Chen, C. Chen, C. Lee, N. Tai and I. Lin, *Nanoscale*, 2013, **5**, 7467.

128.   A. Hatta, H. Nakatsuma, K. Yannai and T. Nishikawa, *Plasma Process. Polym.*, 2007, **4**, S942.

129.   J. Kim and K. Terashima, *Appl. Phys. Lett.*, 2005, **86**, 191504.

130.   D. Staack, B. Farouk, A. F. Gutsol and A. Fridman, *IEEE Trans. Plasma Sci.*, 2007, **35**, 1448.

131.   J. E. Sansonetti and W. C. Martin, *J. Phys. Chem. Ref. Data*, 2005, **34**, 1559.

132.   S. G. Belostotskiy, R. Khandelwal, Q. Wang, V. M. Donnelly, D. J. Economou and N. Sadeghi, *Appl. Phys. Lett.*, 2008, **92**, 221507.

133.   S. G. Belostotskiy, V. M. Donnelly, D. J. Economou and N. Sadeghi, *IEEE Trans. Plasma Sci.*, 2009, **37**, 852.

134.   P. Kurunczi, N. Abramzon, M. Figus and K. Becker, *Acta. Phys. Solvaca*, 2004, **54**, 115.

135.   J. Torres, J. Jonkers, M. J. v. d. Sande, J. J. A. M. v. d. Mullen, A. Gamero and A. Sola, *J. Phys. D: Appl. Phys.*, 2003, **36**, L55.

136.   J. Torres, M. J. v. d. Sande, J. J. A. M. v. d. Mullen, A. Gamero and A. Sola, *Spectrochimica Acta Part B*, 2006, **61**, 56.

137.   B. Du, S. Mohr, D. Luggenholscher and U. Czarnetzki, *J. Phys. D: Appl. Phys.*, 2011, **44**, 125204.

138.   Q. Wang, I. Koleva, V. M. Donnelly and D. J. Economou, *J. Phys. D: Appl. Phys.*, 2005, **38**, 1690.

139.   A. Sola, M. D. Calzada and A. Gamero, *J. Phys. D: Appl. Phys.*, 1995, **28**, 1099.

140.   H. Park and W. Choe, *Curr. Appl. Phys*, 2010, **10**, 1456.

141.   A. Bogaerts, A. Quentmeier, N. Jakubowski and R. Gijbels, *Spectrochimica Acta Part B*, 1995, **50**, 1337.

142.   S. J. Park and J. G. Eden, *Appl. Phys. Lett.*, 2002, **81**, 4127.

143.   I. N. Kosarev, V. I. Khorunzhenko, E. I. Mintoussov, P. N. Sagulenko, N. A. Popov and S. M. Starikovskaia, *Plasma Sources Sci. Technol.*, 2012, **21**, 045012.

144.   G. Chryssolouris, *Laser Machining: Theory and Practice*, Springer-Verlag, New York, 1991.

145.   E. Hecht, *Optics*, 4th edn., Pearson Education Inc., San Francisco, 2002.

146.   P. W. Butler-Smith, D. A. Axinte, M. Pacella and M. W. Fay, *J. Mater. Process. Tech.*, 2013, **213**, 194.

147.   A. V. Zvyagin and N. B. Manson, in *Ultrananocrystalline Diamond: Synthesis, Properties and Applications*, eds. O. A. Shenderova and D. M. Gruen, Elsevier, Oxford, 2nd edn., 2012, p. 344.

148.   J. Roth and C. Garcia-Rosales, *Nucl. Fusion*, 1996, **36**, 1647.

149.   A. Savitzky and M. J. E. Golay, *Anal. Chem.*, 1964, **36**, 1627.
150.   W. L. Wiese and J. R. Fuhr, *J. Phys. Chem. Ref. Data*, 2009, **38**, 565.
151.   W. L. Wiese, M. W. Smith and B. M. Glennon, *Atomic Transition Probabilities Volume I: Hydrogen through Neon*, U.S. Government Printing Office, Washington, 1966.
152.   C. M. Western, *PGOPHER, a Program for Simulating Rotational StructureUniversity of Bristol*, University of Bristol, http://pgopher.chm.bris.ac.uk.
153.   J. F. Kenney and E. F. Keeping, *Mathematics of Statistics*, Van Nostrand, Princeton, 1951.
154.   D. Maric, N. Skoro, P. D. Maguire, C. M. O. Mahony, G. Malovic and Z. L. Petrovic, *Plasma Sources Sci. Technol.*, 2012, **21**, 035016.
155.   S. Wu, X. Lu and Y. Pan, *Curr. Appl. Phys*, 2013, **13**, S1.
156.   K. T. Burm, *Contrib. Plasma Phys.*, 2007, **47**, 177.
157.   L. A. Mendes, M. Mafra and J. C. Rodrigues, *Rev. Sci. Instrum.*, 2012, **83**, 015112.
158.   D. Staack, B. Farouk, A. Gutsol and A. Fridman, *Plasma Sources Sci. Technol.*, 2005, **14**, 700.
159.   C. Lazzaroni, P. Chabert, A. Rousseau and N. Sadeghi, *Eur. Phys. J. D*, 2010, **60**, 555.
160.   H. E. Feng, H. E. Shoujie, Z. Xiaofei, G. Bingang and O. Jiting, *Plasma Sci. Technol.*, 2012, **14**, 1079.
161.   S. Pekarek, *Eur. Phys. J. D*, 2010, **56**, 91.
162.   P. J. Goodhew, J. Humphreys and R. Beanland, *Electron Microscopy and Analysis*, 3rd edn., Taylor & Francis, London, 2001.
163.   I. Petrov, P. B. Barna, L. Hultman and J. E. Greene, *J. Vac. Sci. Technol. A*, 2003, **21**, S117.
164.   I. M. Watt, *The Principles and Practice of Electron Microscopy*, 2nd edn., Cambridge University Press, Cambridge, 1997.
165.   Y. D. Wang and J. T. Ouyang, *IEEE Trans. Plasma Sci.*, 2008, **36**, 1264.
166.   D. Ishihara, Y. Noma, S. Stauss, M. Sai, T. Tomai and K. Terashima, *Plasma Sources Sci. Technol.*, 2008, **17**, 035008.
167.   Q. Wang, D. J. Economou and V. M. Donnelly, *J. Appl. Phys.*, 2006, **100**, 023301.
168.   D. Emerson, *Interpreting Astronomical Spectra*, John Wiley & Sons, Chichester, 1996.
169.   M. A. Naveed, N. U. Rehman, S. Zeb, S. Hussain and M. Zakaullah, *Eur. Phys. J. D*, 2008, **47**, 395.
170.   N. K. Bibinov, A. A. Fateev and K. Wiesemann, *J. Phys. D: Appl. Phys.*, 2001, **34**, 1819.
171.   N. U. Rehman, F. U. Khan, M. A. Naveed and M. Zakaullah, *Plasma Sources Sci. Technol.*, 2008, **17**, 025005.
172.   S. Mahmood, N. M. Shaikh, M. A. Kalyar, M. Rafiq, N. K. Piracha and M. A. Baig, *J. Quant. Spectrosc. Radiat. Transfer*, 2009, **110**, 1840.
173.   S. K. Monfared, A. R. Hoskinson and J. Hopwood, *J. Phys. D: Appl. Phys.*, 2013, **46**, 425201.
174.   A. R. Hoskinson, J. Hopwood, N. W. Bostrom, J. A. Crank and C. Harrison, *J. Anal. At. Spectrom.*, 2011, **26**, 1258.
175.   J. Jonkers and J. A. M. v. d. Mullen, *J. Quant. Spectrosc. Radiat. Transfer*, 1999, **61**, 703.

Appendix I

1   Further Types of Microplasma Devices

In addition to MHCDs explored in the introduction, several other devices are also common. These are explored below.

1.1 Cathode Boundary Layer Discharge

Cathode Boundary Layer Discharges (CBLDs) operate using DC and follow the geometry shown in figure 3.5.[1]   They are closely related to high pressure MHCDs[2] and generally consist of a ring-shaped anode and planar cathode separated by a dielectric film.[3]
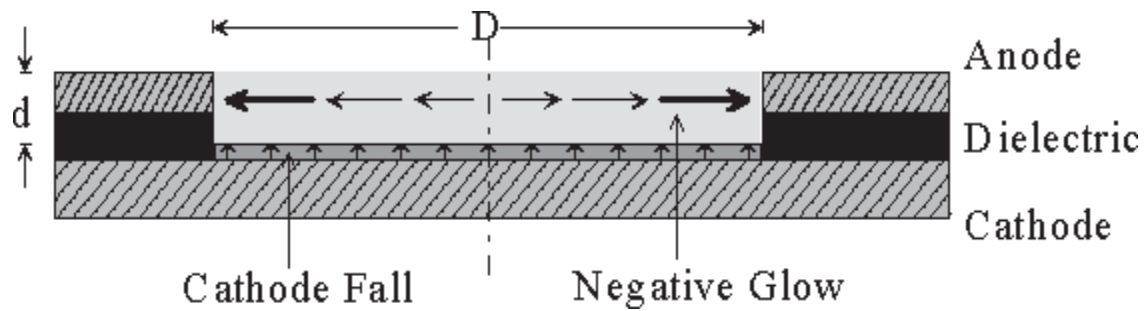
Figure 18. The conventional geometry of a CBLD.[1]

The discharge consists of only the negative glow and cathode-fall regions. The negative glow region acts as a virtual anode, allowing the current to flow radially towards the anode.[4]
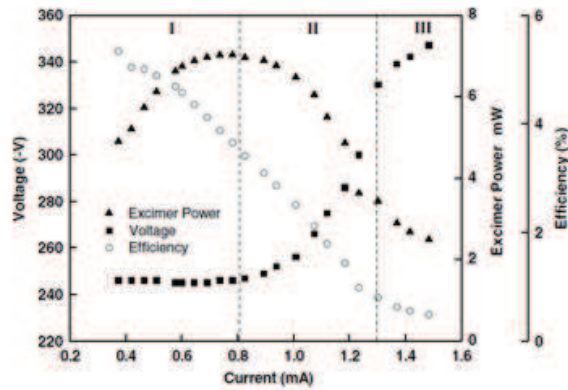
Figure 19. The V-I characteristic for a CBLD operating in neon (250 Torr). Three regions are observed: normal glow (I), self-organisation (II) and abnormal glow (III). Excimer power and efficiency are also plotted against current.[2]
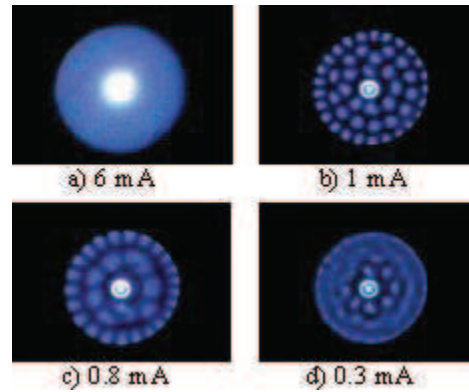
Figure 3. End-on images of a CBLD operating in xenon (128 Torr) at different currents.[4]

V-I characteristics for CBLDs differ from those of MHCDs; as shown in Figure 2 the curve is slightly sigmoidal in shape with no region of negative differential resistance.[2] Initially the discharge is in the normal glow mode with a flat gradient. Once the discharge has covered the surface of the cathode it enters the self-organisation mode, in which patterns appear, examples are shown in figure 3.[4] Although initial investigations stipulated that special mechanisms were

required to explain these patterns, more recently developed models have shown that basic mechanisms such as electron and ion diffusion and secondary electron emission are sufficient.[5] At a certain current, the voltage begins to level off and the discharge has entered the abnormal glow mode. No patterns are observed in this mode.

1.2 Dielectric Barrier Discharges

Dielectric Barrier Discharges (DBDs) are discharges formed between two electrodes, where at least one of the electrodes is coated in a dielectric layer, illustrated in figure 4.[6, 7] The dielectric layer prevents the glow-to-arc transition by limiting charged particles' access to the electrodes[8]. The layer also prevents DC operation; alternating current in the kHz range is used instead.

At low pressures, diffuse glow discharges similar to those described in Section 2.3 are easily obtained.[6] At higher pressures, filamentation of the discharge tends to occur; the filament pattern can either be well-defined or randomly distributed.[9, 10] Under certain conditions a uniform diffuse glow mode has been observed at atmospheric pressure, however, it is unclear whether this is truly a glow mode or just a high number of filaments closely coupled.[11, 12]

A variety of different geometries have been investigated. One of these, the Capillary Plasma Electrode Discharge (CPED), has a novel design in which dielectric capillaries cover the electrodes as opposed to films. The CPED exhibits a unique mode not observed in conventional DBDs: the capillary jet mode.

Figure 4. Common DBD geometries. [6, 7]

Intense plasma jets emerge from the capillaries in this mode.[13] The CPED can be operated under both DC and AC conditions, and gives a V-I characteristic representative of an abnormal glow discharge over the entire operating range.[3]

1.3 RF Capacitively Coupled Plasmas

Conventional radio frequency (RF) Capacitively Coupled Plasmas (CCP) are widely used in industry, particularly in the etching of semiconductor surfaces.[7, 14] RF CCPs consist of two planar electrodes separated by a small distance. The simplest geometry takes the form of two parallel conductive plates acting as the electrodes, however other designs, including the use of perforated and comb shaped electrodes have been studied.[15, 16]

Upon miniaturisation and subjection to higher pressures, RF CCPs become vulnerable to glow-to-arc transitions. Coating of the electrodes with insulating materials can be used to reduce instabilities while maintaining plasma function due to the high radio frequencies used; in these cases they can also be classed as RF DBDs.[17] Despite this, high pressure RF CCPs do not function as well as other microplasmas; as a consequence of the electric field lying perpendicular to the electrodes, sputtering is common and the ion density limited.[7]

1.4 RF Inductively Coupled Plasmas

Miniaturised Inductively Coupled Plasmas (mICPs) have no electrodes; instead the electric field is induced through a coil wrapped around a dielectric barrier, as shown in figure 5.[8]

Figure 5. A common mICP configuration.[8]

mICPs operate well at low pressures. At atmosphere pressure however, the power and current required is extremely high and consequently the devices are inefficient.[18]

2 Stark Broadening

Some spectral lines in a plasma optical emission spectrum appear broader than they would otherwise. The most common spectral lines analysed are the H_β and H_γ lines in either the Balmer or Lyman series. These lines are either present in plasma spectra due to water impurities or small additions of H_2.[19]

In a high pressure microplasma the relevant sources of broadening come from four processes: Stark, instrumental, van der Waals (pressure) and Doppler broadening. Stark broadening is the important process with regards to T_e and n_e. It is a consequence of the Stark effect: the interaction of free electron and ion electric fields with radiating atoms. Instrumental and Doppler broadening generate Gaussian profiles, whereas Stark and van der Waals broadening exhibit Lorentzian profiles. A combination of these profiles gives a Voigt profile, expressed in Equation 1:

$$\Delta\lambda_{\text{Voigt}} \approx \left[\left(\frac{\Delta\lambda_{\text{Lorentz}}}{2} \right)^2 + (\Delta\lambda_{\text{Gauss}})^2 \right]^{\frac{1}{2}} + \left(\frac{\Delta\lambda_{\text{Lorentz}}}{2} \right) \tag{1}$$

where $\Delta\lambda$ corresponds to the full-width half-maximum (FWHM) of either the Lorentz or Gaussian contribution. From this expression the broadening due solely to the Lorentz profiles can be isolated, provided Doppler broadening and instrumental broadening are known.[20] Subtraction of van der Waals broadening, which can be calculated using T_g, from $\Delta\lambda_{Lorentz}$ yields $\Delta\lambda_{Stark}$.[21]

The FWHM dependence on Stark broadening is related to the electron density according to Equation 2:

$$\Delta\lambda_{\text{Stark}} = 2.50 \times 10^{-10} \cdot \alpha(n_e, T_e) \cdot n_e^{\frac{2}{3}} \tag{2}$$

where $\Delta\lambda_{Stark}$ is in nm and n_e in cm^{-3}. The parameter α, in Å per cgs field strength unit, is the reduced wavelength separation, it is specific to the transition and has a small dependence on both n_e and T_e.[22] Values of α for a variety of different densities and temperatures have been tabulated.[23] In many investigations a specific value of α is taken, dependent on an estimated n_e and T_e, this can provide a good approximation of electron density.[21, 24-26] In other investigations both T_e and n_e are found simultaneously by calculating how n_e varies with T_e for two or more different spectral lines.[19, 20, 27] Stark broadening of spectral lines from Ar have also been used to find n_e and T_e.[27, 28]

3 References

1. M. Moselhy and K. H. Schoenbach, *J. Appl. Phys.*, 2004, **95**, 1642.
2. W. Zhu, N. Takano, K. H. Schoenbach, D. Guru, J. Mclaren, J. Heberlein, R. May and J. R. Cooper, *J. Phys. D: Appl. Phys.*, 2007, **40**, 3896.
3. K. H. Becker, K. H. Schoenbach and J. G. Eden, *J. Phys. D: Appl. Phys.*, 2006, **39**, R55.
4. K. H. Schoenbach, M. Moselhy and W. Shi, *Plasma Sources Sci. Technol.*, 2004, **13**, 177.
5. M. S. Benilov, *Plasma Sources Sci. Technol.*, 2007, **16**, 422.
6. U. Kogelschatz, *Plasma Chem. Plasma Proc.*, 2003, **23**, 1.
7. F. Iza, G. J. Kim, S. M. Lee, J. K. Lee, J. L. Walsh, Y. T. Zhang and M. G. Kong, *Plasma Process. Polym.*, 2008, **5**, 322.
8. A. P. Papadakis, S. Rossides and A. C. Metaxas, *Open Appl. Phys. J.*, 2011, **4**, 45.
9. J. Guikema, N. Miller, J. Niehof, M. Klein and M. Walhout, *Phys. Rev. Lett.*, 2000, **85**, 3817.
10. M. Klein, N. Miller and M. Walhout, *Phys. Rev. E*, 2001, **64**, 026402.
11. F. Massines, A. Rabehi, P. Decomps, R. B. Gadri, P. Segur and C. Mayoux, *J. Appl. Phys.*, 1998, **83**, 2950.
12. G. Nersisyan and W. G. Graham, *Plama Sources Sci. Technol.*, 2004, **13**, 582.
13. E. E. Kunhardt, *IEEE Trans. Plasma Sci.*, 2000, **28**, 189.
14. R. L. Layberry, Z. Wronski, C. G. Pearce and J. L. Sullivan, *J. Phys. D: Appl. Phys.*, 1999, **32**, 1857.
15. M. Moravej and R. F. Hicks, *Chem. Vap. Deposition*, 2005, **11**, 469.
16. K. Taniguchi, T. Fukasawa, H. Yoshiki and Y. Horiike, *Jpn. J. Appl. Phys.*, 2003, **42**, 6584.
17. J. J. Shi, D. W. Liu and M. G. Kong, *Appl. Phys. Lett.*, 2006, **89**, 081502.
18. J. Hopwood and F. Iza, *J. Anal. At. Spectrom.*, 2004, **19**, 1145.
19. J. Torres, J. Jonkers, M. J. v. d. Sande, J. J. A. M. v. d. Mullen, A. Gamero and A. Sola, *J. Phys. D: Appl. Phys.*, 2003, **36**, L55.
20. J. Torres, M. J. v. d. Sande, J. J. A. M. v. d. Mullen, A. Gamero and A. Sola, *Spectrochimica Acta Part B*, 2006, **61**, 56.
21. S. G. Belostotskiy, R. Khandelwal, Q. Wang, V. M. Donnelly, D. J. Economou and N. Sadeghi, *Appl. Phys. Lett.*, 2008, **92**, 221507.
22. J. M. Luque, M. D. Calzada and M. Saez, *J. Phys. B: At. Mol. Opt. Phys.*, 2003, **36**, 1573.
23. P. Kepple and H. R. Griem, *Phys. Rev.*, 1968, **173**, 317.
24. M. D. Calzada, M. Moisan, A. Gamero and A. Sola, *J. Appl. Phys.*, 1996, **80**, 46.
25. B. Du, S. Mohr, D. Luggenholscher and U. Czarnetzki, *J. Phys. D: Appl. Phys.*, 2011, **44**, 125204.
26. Q. Wang, I. Koleva, V. M. Donnelly and D. J. Economou, *J. Phys. D: Appl. Phys.*, 2005, **38**, 1690.
27. B. N. Sismanoglu, C. L. A. Cunha, M. P. Gomes, R. Caetano and K. G. Grigorov, *Braz. J. Phys*, 2010, **40**, 459.
28. M. Miclea, K. Kunze, U. Heitmann, S. Florek, J. Franzke and K. Niemax, *J. Phys. D: Appl. Phys.*, 2005, **38**, 1709.
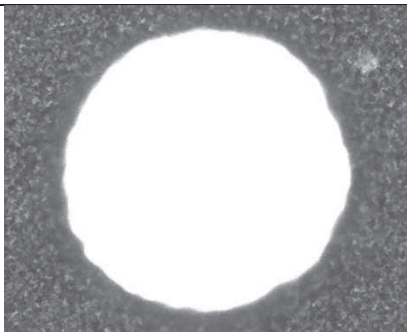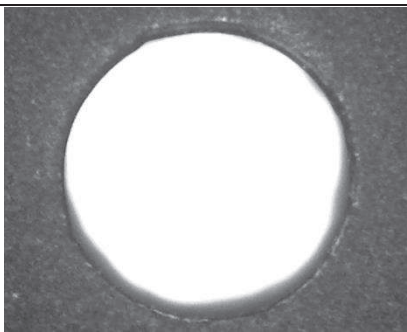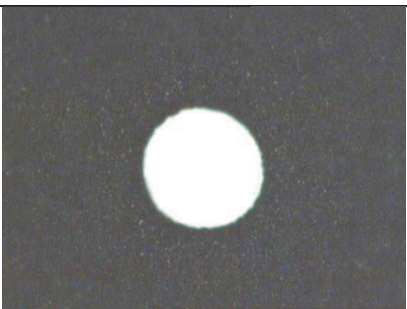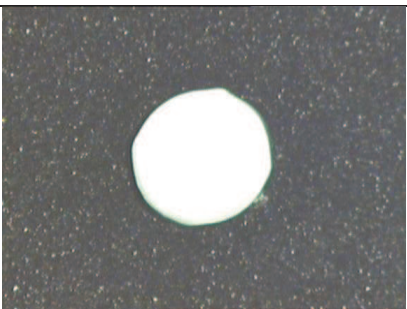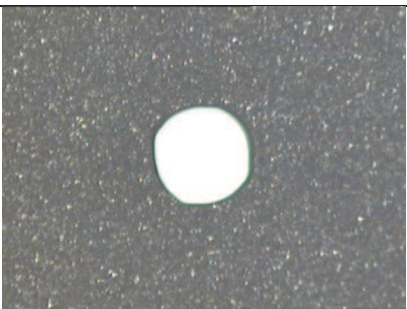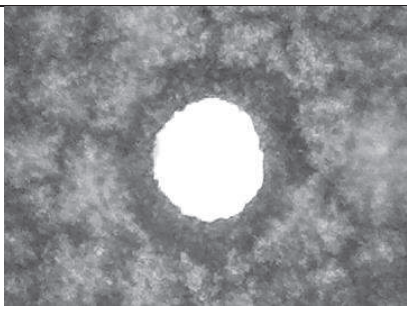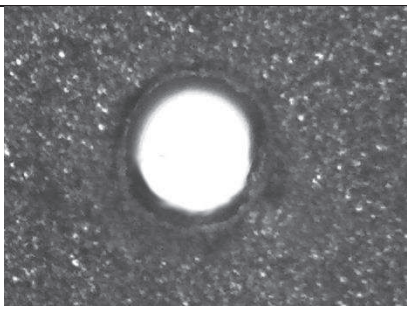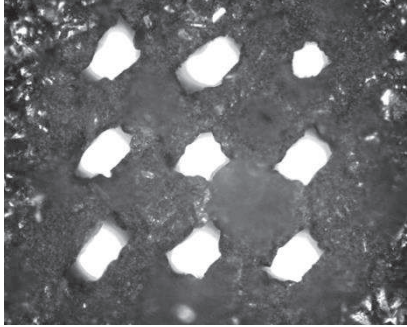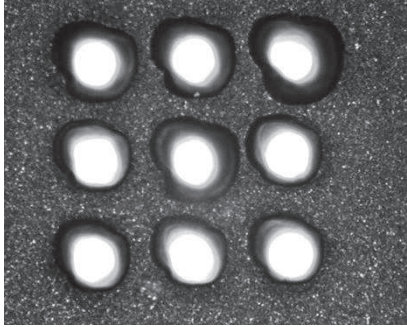
Appendix II
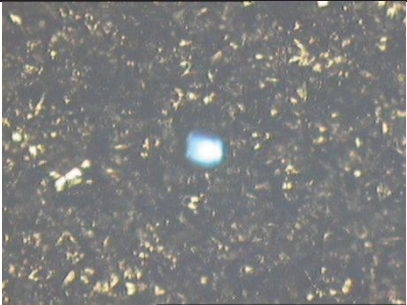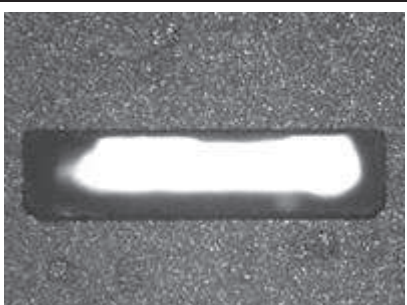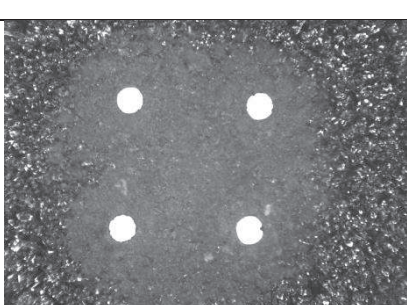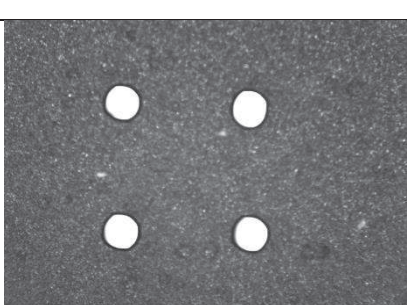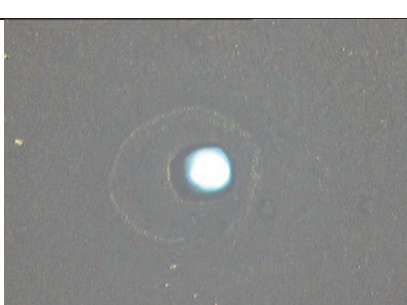
1   Working Samples
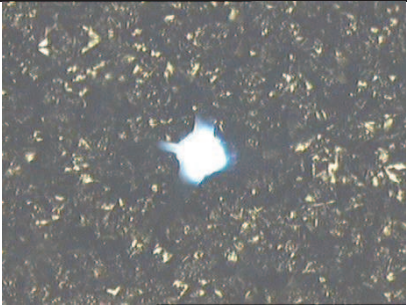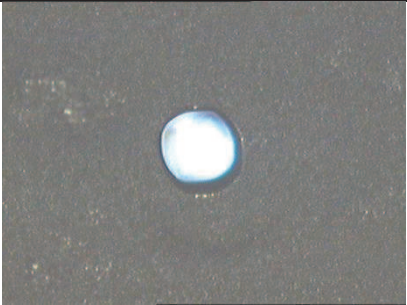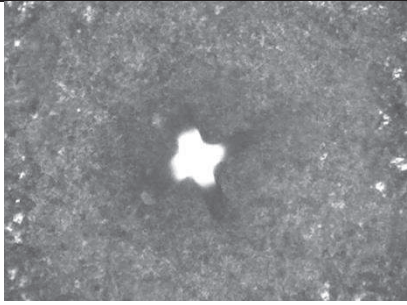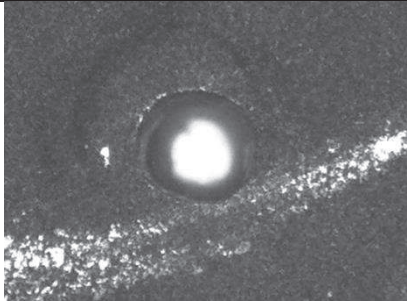
The thirteen working samples are shown in table 1.

Table 1. Working samples and their dimensions.   Sample reference codes are also shown.

Reference	Cathode Side	Insulator Side	Dimension / μm
A3			600
C1			300
C2			200
C4			250

D3			50
D4			40
E1			1000 × 200
E2			200 (×4)
E4			100

F1			150
F4			150
G1			~150 × 9
G2			1000 × 200

Appendix III

1   V-I Characteristics

The following section contains the V-I characteristics for several devices over a range of pressures. For clarity the V-I characteristics for each device have been separated into two graphs.
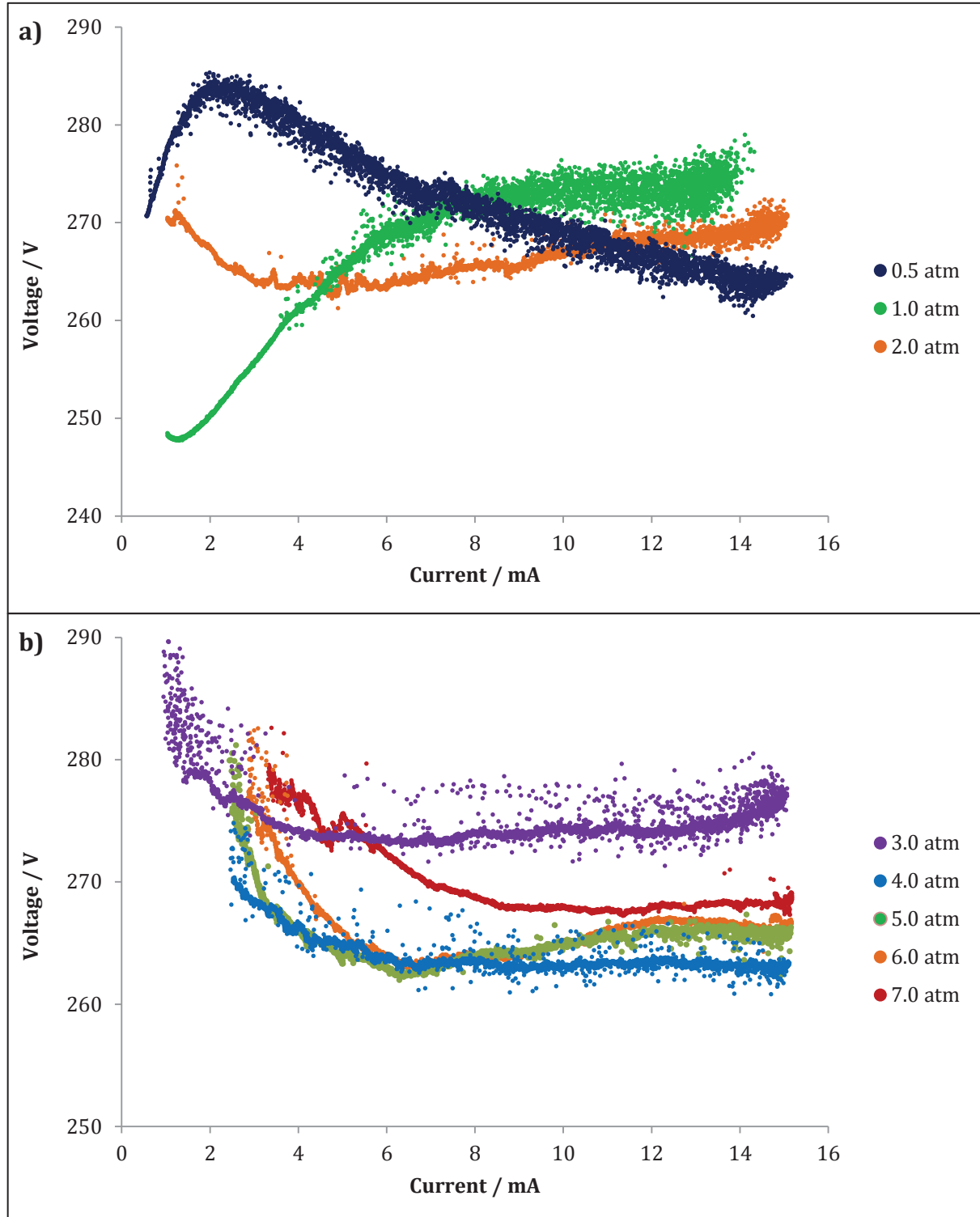
Figure 6. V-I characteristics for a 300 μm device between 0.5 – 2.0 atm (a) and 3.0 – 7.0 atm (b).
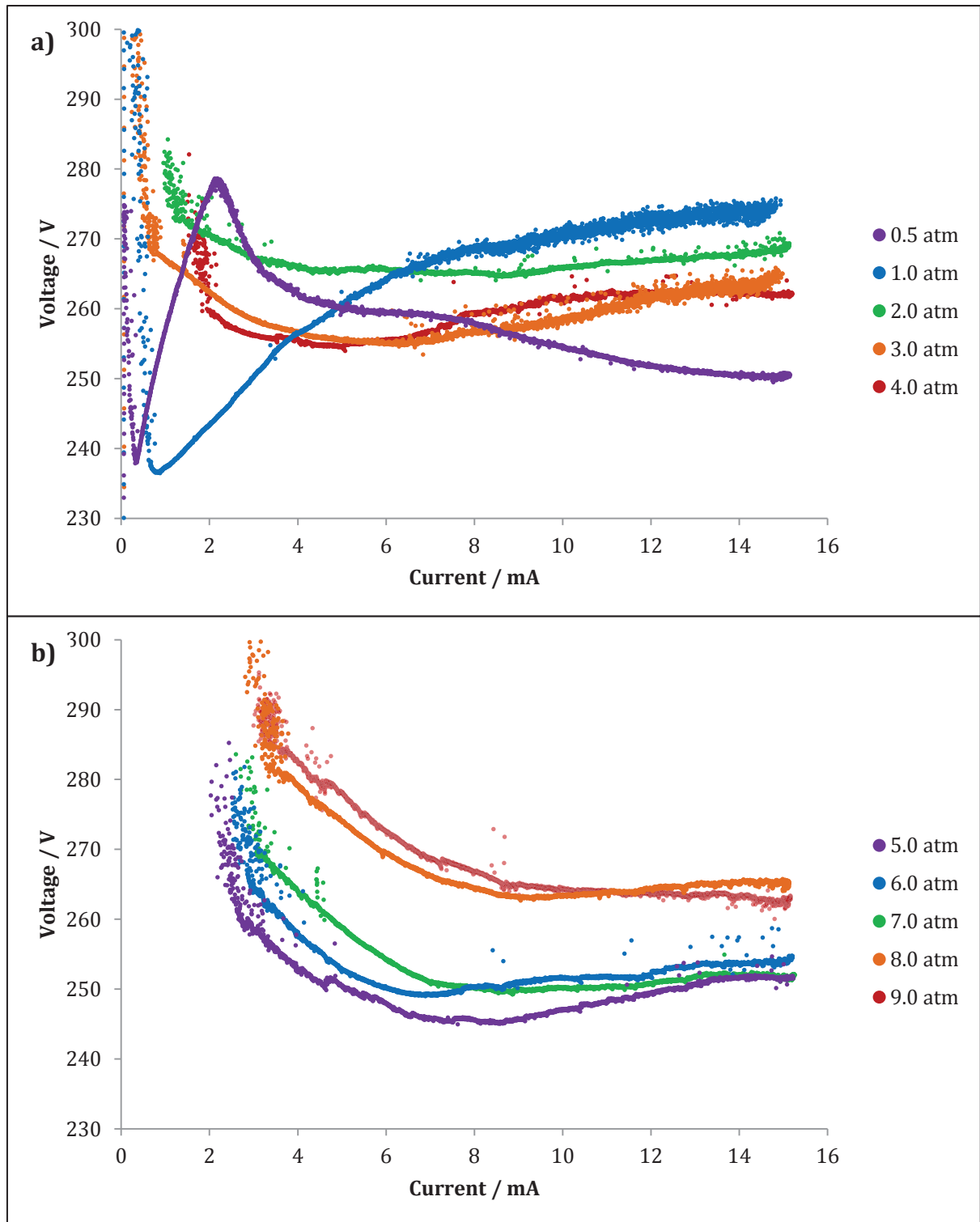
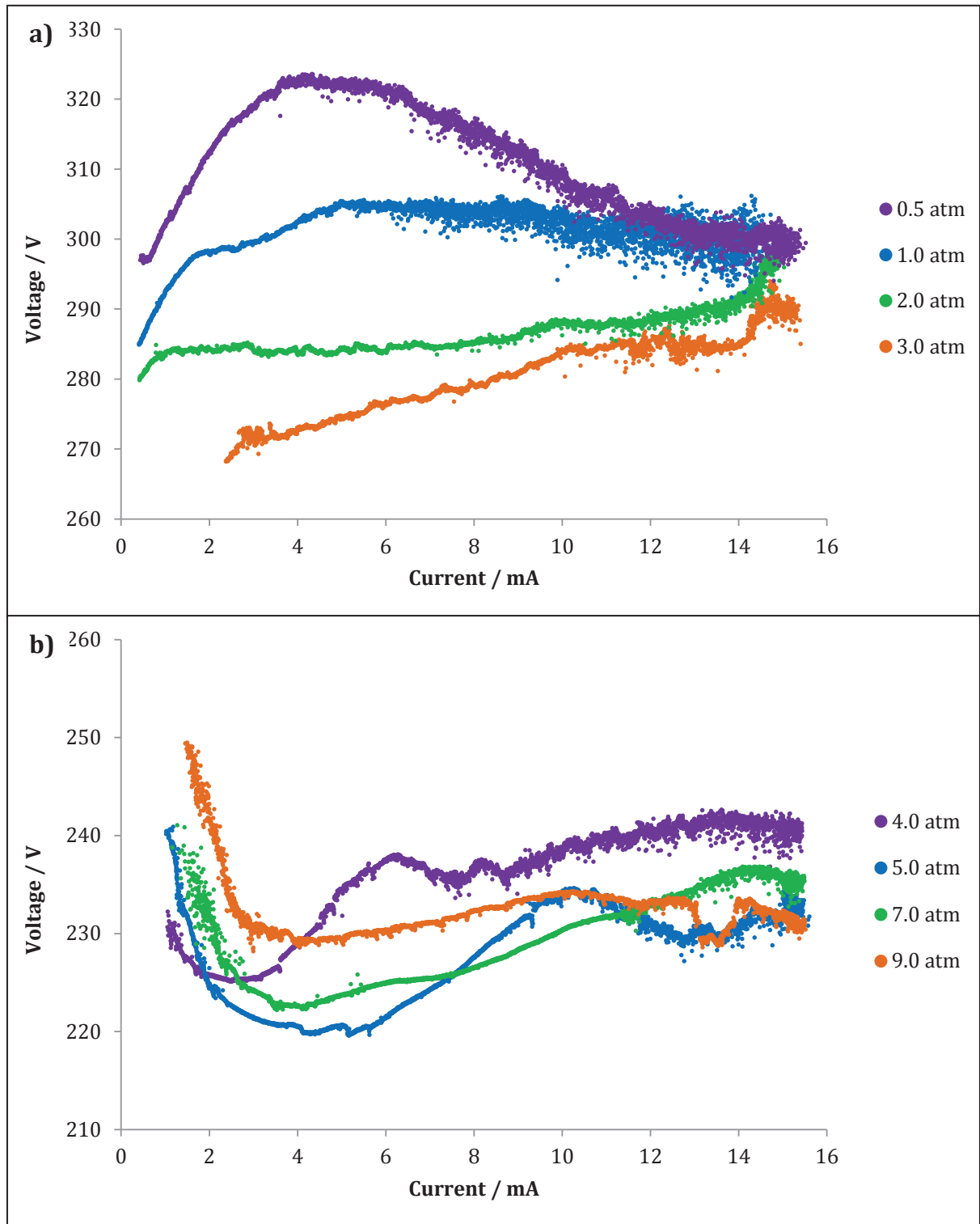**Figure 7.** V-I characteristics for a 200 μm device between 0.5 – 4.0 atm (a) and 5.0 – 9.0 atm (b).
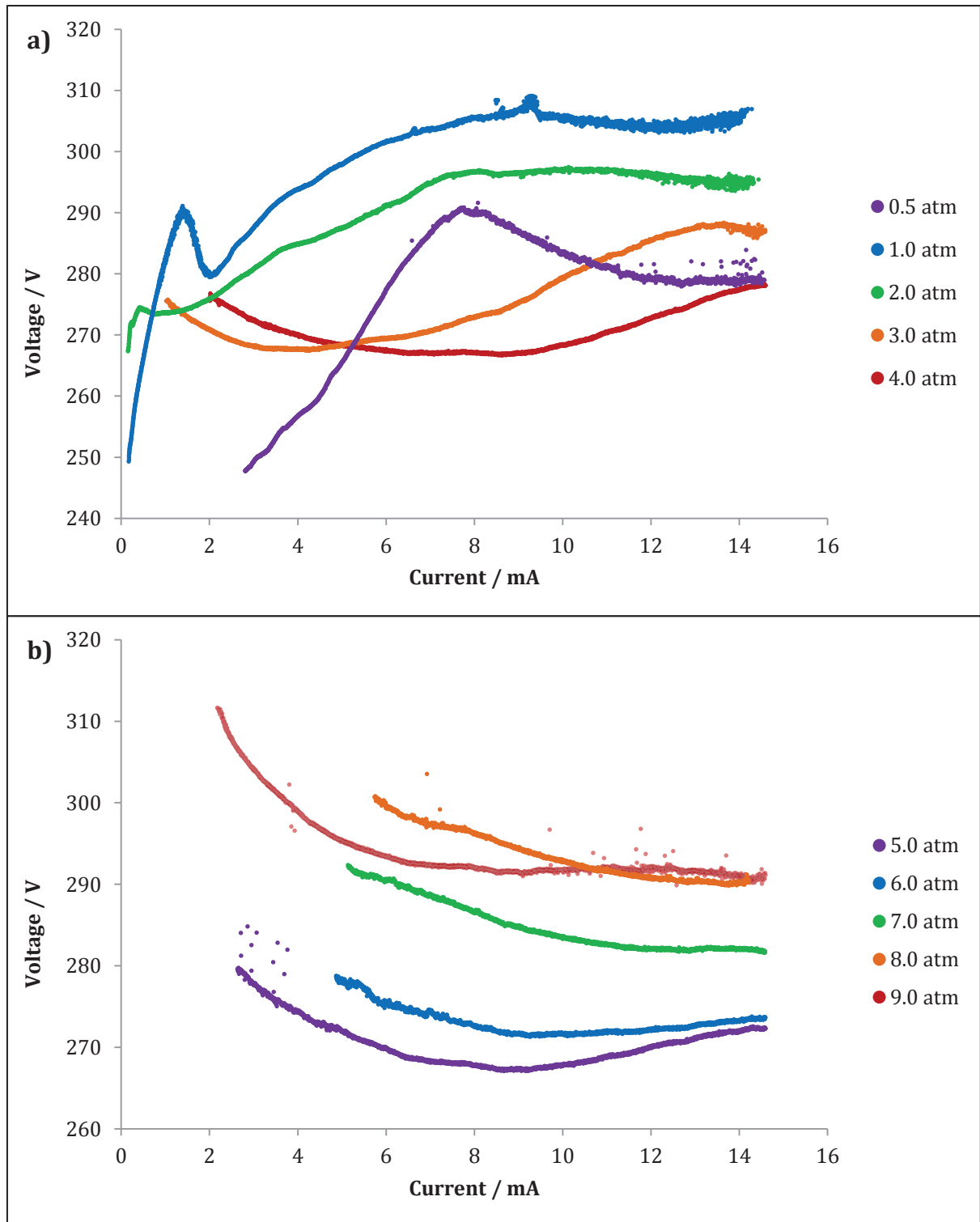
Figure 8. V-I characteristics for a 100 μm device between 0.5 – 4.0 atm (a) and 5.0 – 9.0 atm (b).

x
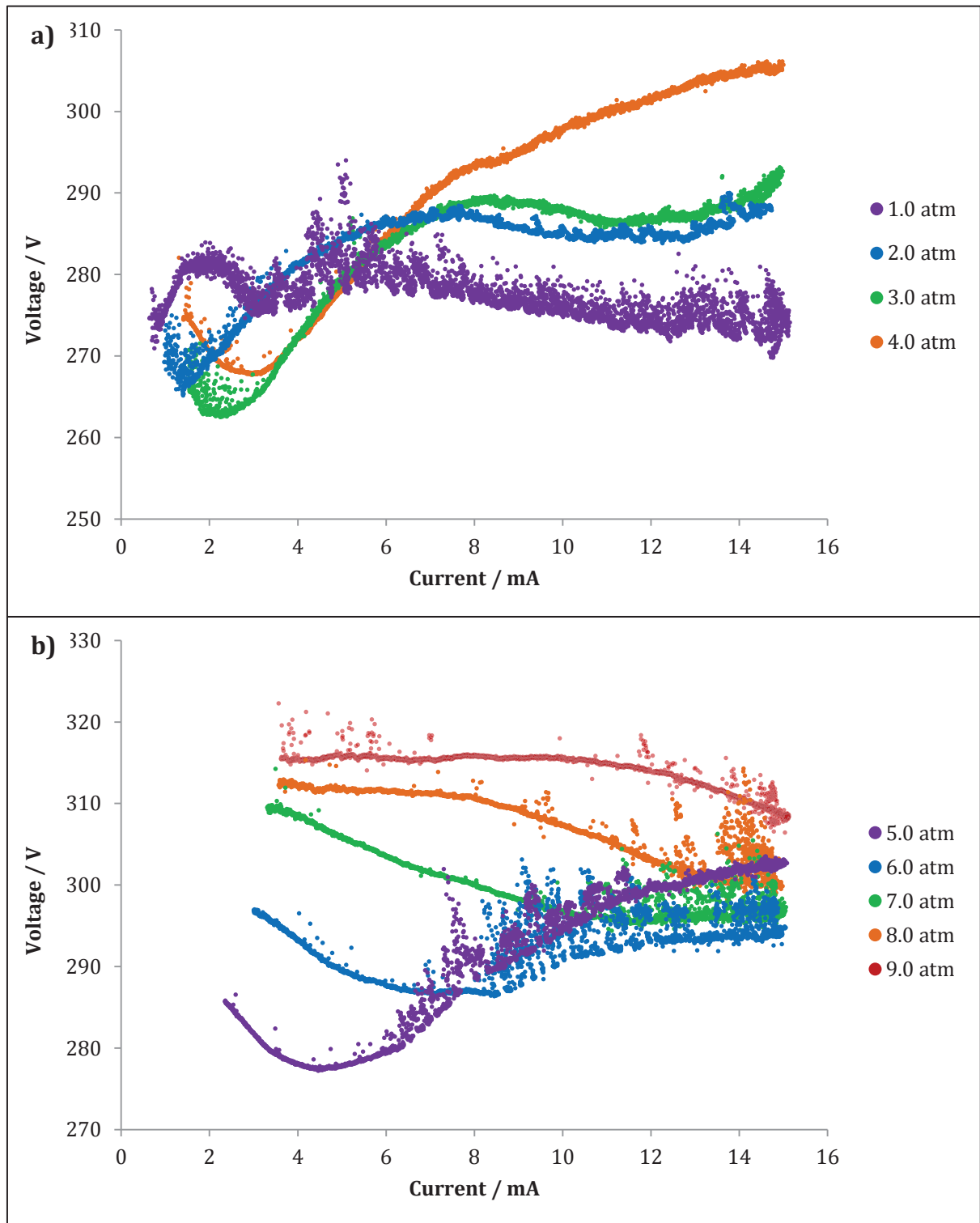
**Figure 9.** V-I characteristics for a 50 μm device between 1.0 – 4.0 atm (a) and 5.0 – 9.0 atm (b).

Figure 10. V-I characteristics for a 1000 × 200 μm slit device between 0.5 – 3.0 atm (a) and 4.0 – 9.0 atm (b).

2   OES Temperature Measurements

A summary of the floated variables used to simulate the experimental spectra is shown in table 2. Additionally, both the recorded spectra over all wavelengths and the simulated region is shown for each pressure.

Table 2. The floated variables used to match the simulated spectra to the experimental spectra.

| Pressure / atm	Simulated T_R / K	Simulated T_V / K	Simulated Lorentzian
0.5	390.8 (85)	12890 (450)	0.0112 (0.0021)
1.0	422.8 (84)	6280 (110)	0.0172 (0.0020)
2.0	377.7 (85)	3717 (51)	0.0085 (0.0021)
4.0	467 (11)	2767 (39)	0.0189 (0.0026)
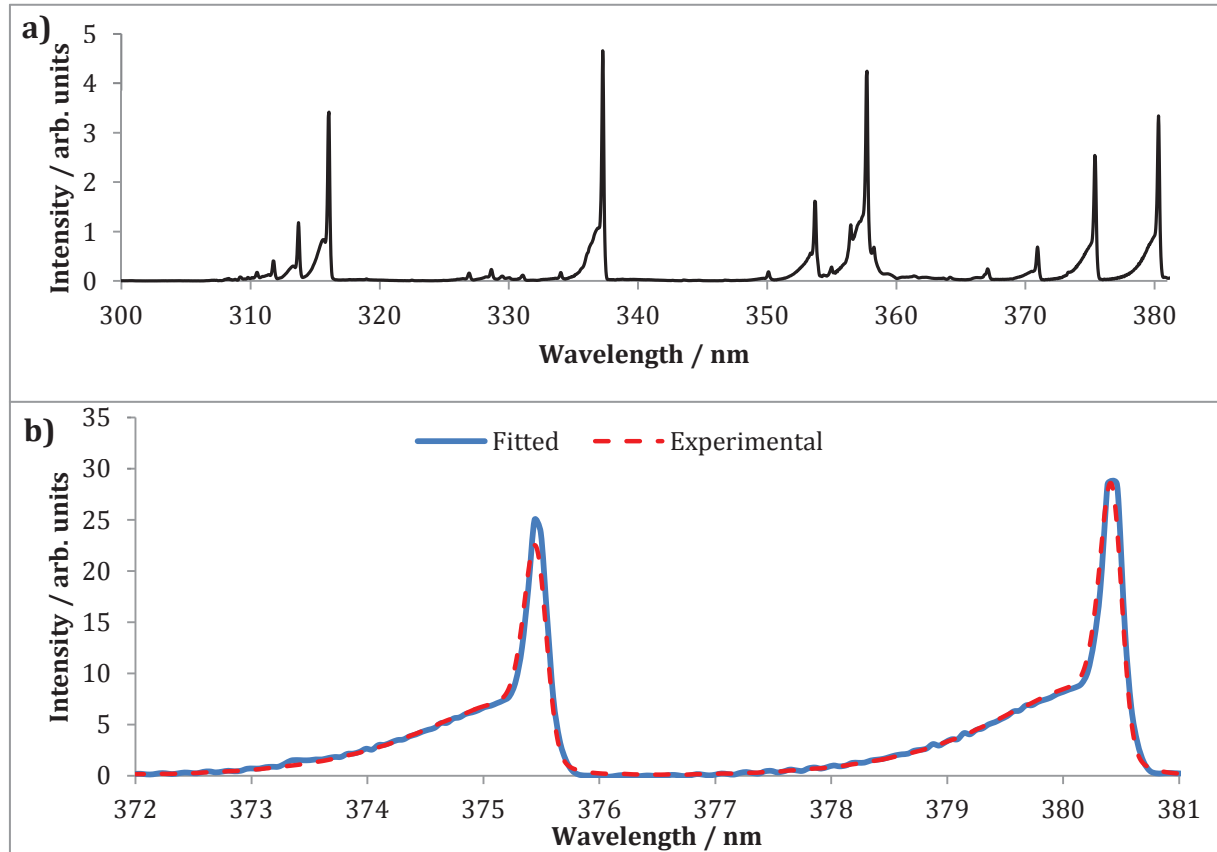
Figure 11. The observed spectra between 300 and 382 nm (a) and both the simulated and experimental C $^3\Pi_g$ (v=0,1) → B $^3\Pi_g$ (v=2,3) bands (b) for a 300 μm device at 0.5 atm (He, trace N_2).
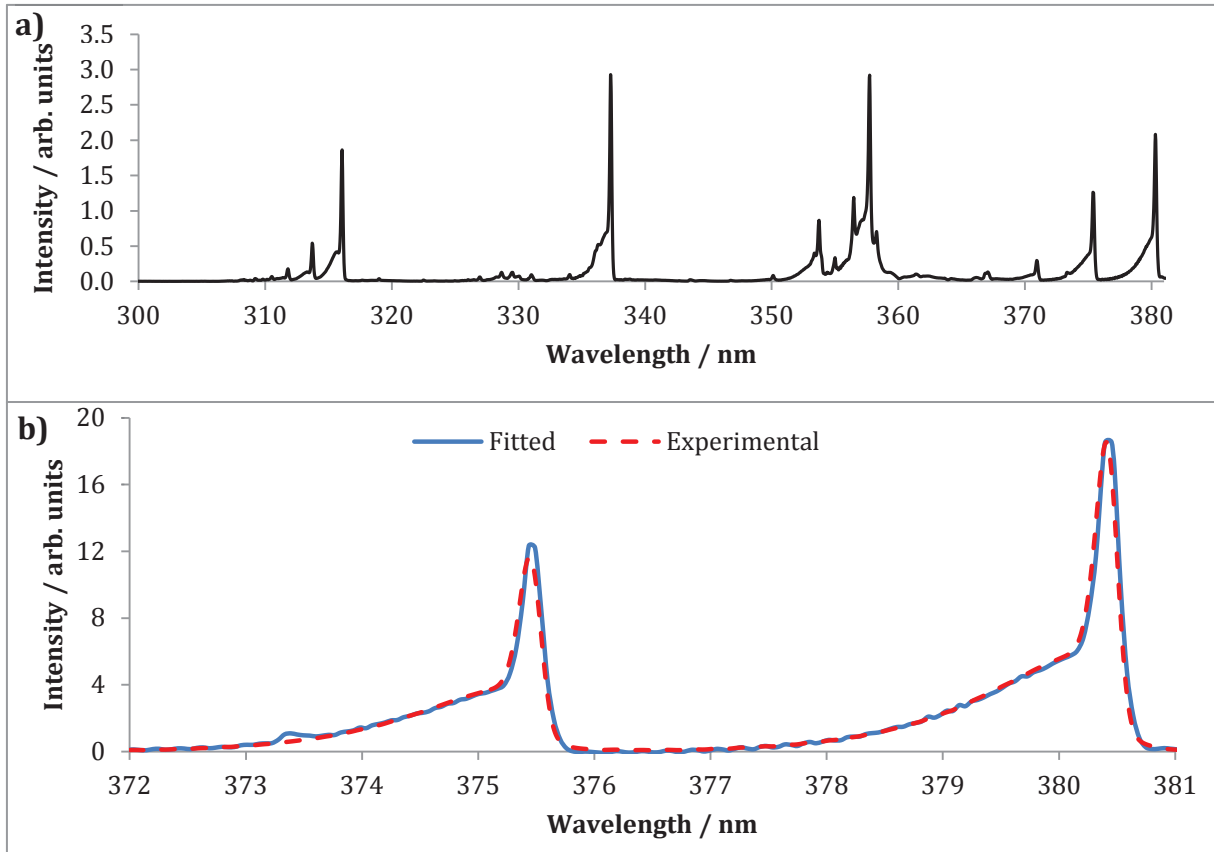
Figure 12. The observed spectra between 300 and 382 nm (a) and both the simulated and experimental C $^3\Pi_g$ (v=0,1) → B $^3\Pi_g$ (v=2,3) bands (b) for a 300 μm device at 1.0 atm (He, trace N_2).
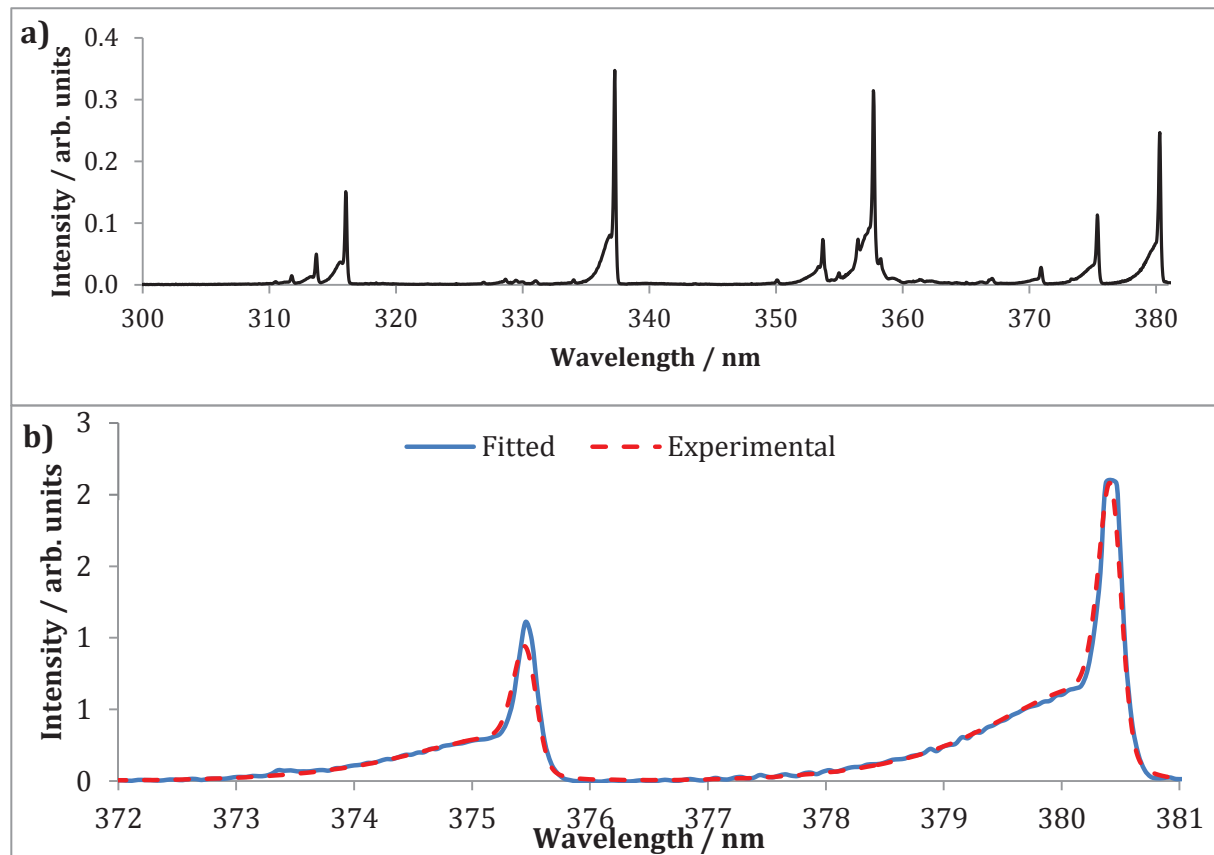
Figure 13. The observed spectra between 300 and 382 nm (a) and both the simulated and experimental C $^3\Pi_g$ (v=0,1) → B $^3\Pi_g$ (v=2,3) bands (b) for a 300 μm device at 2.0 atm (He, trace N_2).
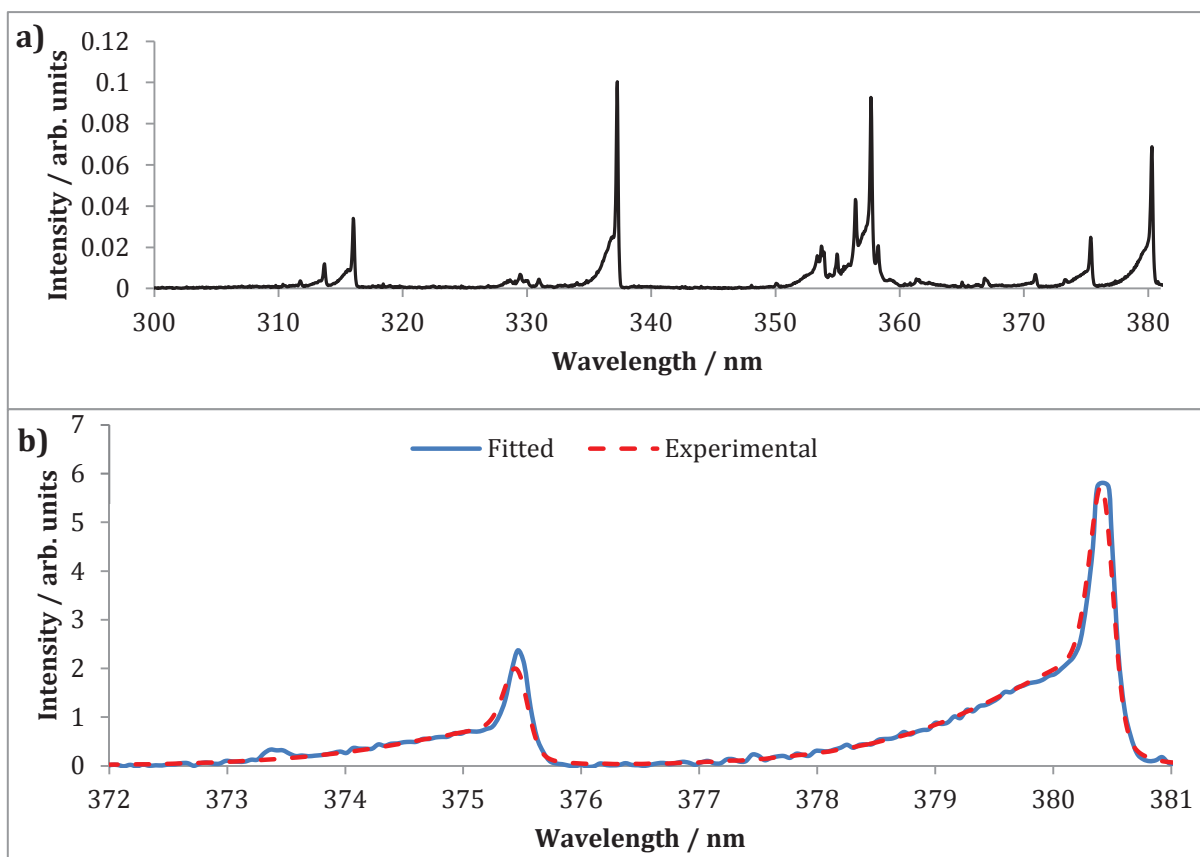
Figure 14. The observed spectra between 300 and 382 nm (a) and both the simulated and experimental C $^3\Pi_g$ (v=0,1) → B $^3\Pi_g$ (v=2,3) bands (b) for a 300 μm device at 4.0 atm (He, trace N_2).